Alma Mater Studiorum · University of Bologna

School of Science
Department of Physics and Astronomy
Master Degree in Physics

Characterization of innovative kerfless cutting of monocrystalline silicon wafers for photovoltaic applications

Supervisor:
Prof. Daniela Cavalcoli

Co-supervisor:
Prof. Marisa Di Sabatino Lundberg

Submitted by:
Lia Giulia D'Amico

Academic Year 2021/2022

"Deep in the human unconscious is a pervasive need
for a logical universe that makes sense.
But the real universe is always one step beyond logic."
- The Sayings of Muad'Dib
Frank Herbert, Dune

A Giulio, amico e brillante fisico

Acknowledgements

Questo progetto è stato reso possibile dalla mia relatrice, Prof.ssa Daniela Cavalcoli, che mi ha seguito con dedizione durante tutta questa esperienza e mi ha dato l'opportunità di realizzare il mio progetto all'estero.

Ringrazio anche la Prof.ssa Marisa Di Sabatino Lundberg, che mi ha accolto a Trondheim ed è stata la mia co-relatrice alla Norwegian University of Science e Tecnologia, e la Prof. Irina Sorokina e il Dr. Maksim Demesh, che mi hanno permesso di collaborare con loro.

Un ringraziamento particolare va al Dott. Cristiano Albonetti dell' "Istituto per lo Studio dei Materiali Nanostrutturati" (ISMN) del "Consiglio Nazionale delle Ricerche" (CNR), per aver fornito un eccellente introduzione al mondo della microscopia e per aver mostrato una disponibilità e un interesse inestimabili per il mio progetto.

Per ultimi ma non meno importanti, voglio ringraziare coloro che mi hanno sempre sostenuto con amore, pazienza e comprensione: Valentina, Sofia, Ilaria, Federico, Monica e Gianmaria. Siete la mia casa.
Ringrazio di cuore Giovanni, Davide e Costanza per la loro amicizia, e Arianna, Rocco, Francesco e Alberto per i bei momenti condivisi a Trondheim.
Infine, voglio citare gli amici del DIFA, in particolare Camilla: un affiatato gruppo di giovani ricercatori con la loro unicità e con un valore inestimabile che merita un riconoscimento speciale. Ma soprattutto li ringrazio per aver reso questo viaggio speciale e per essermi stati vicini come se fossimo stati amici da una vita. Voglio anche ricordare Giulio, che non è più con noi, ma il cui sorriso non dimenticheremo.

Abstract

Nowadays renewable energies are a hot research topic, and the goal is to improve cell efficiency and reduce production costs, aiming to make the use of photovoltaics increasingly widespread and convenient. Monocrystalline silicon solar cells are leaders in the photovoltaic market. However, market-established cutting techniques produce a consistent amount of material waste when cutting ingots into wafers. The"Stress-induced LIft-Off Method" (SLIM) is emerging in recent years as an alternative, more sustainable separation technique, which reduces material loss and can lead to obtaining increasingly thinner wafers, further reducing the required amount of silicon.

This thesis presents the micro-characterization of the separated wafers with the SLIM technique. The wafers were obtained with a two-step procedure. First, a layer of defects was induced in the silicon using ultra-short medium-infrared laser pulses. Then, the material was deposited on one of the sides and induced stress in the silicon, such as to further weaken it. In this way, only rapid cooling is required for detachment to occur. Measurements of the minority carriers' lifetime and Raman spectra, along with SEM images, were used to understand how the separation changed the properties of the monocrystalline silicon surface layers in SLIM-cut wafers. The same techniques have also been employed to perform a morphological study of laser-induced defects, buried in unseparated bulk silicon samples. The atomic force microscope (AFM) made it possible to complete the morphological analysis of the separated wafers by providing information on the topography and electrical behaviour of the modified and unmodified regions.
The obtained results indicate that the SLIM-cut technique halves the minority carriers' lifetime. There is no amorphization, crystal disorder or high-pressure phases. However, changes in the Raman spectra suggest that tensile stress may have been produced on these surface layers by the separation process. The AFM topography highlights surface irregularities, which may be removed with a polishing step. The surface also shows laser-modified regions, which are evident in SEM images, but not in AFM topographies, suggesting a charging effect due to electron bombardment. Lastly, the electrical characterization by conductive AFM lacks any changes in the conductive behaviour of the material where the laser-modified areas should be located.

In conclusion, these preliminary results are promising to continue the study of this innovative SLIM technique. The prospect could be to optimize the three cutting steps to produce a more significant number of separate wafers with the standard dimensions required by the photovoltaic industry. In this way, a systematic characterization of this technique could be carried out.

Abstract

Questa tesi presenta la microcaratterizzazione dei wafer separati con la tecnica "Stress-induced LIft-Off Method" (SLIM), che sta emergendo negli ultimi anni come una tecnica di separazione alternativa, più sostenibile, in grado di ridurre la perdita di materiale e che può portare all'ottenimento di wafer sempre più sottili, riducendo ulteriormente la quantità necessaria di silicio. In primo luogo, è stato indotto nel silicio uno strato di difetti utilizzando impulsi laser infrarossi ultra-brevi. Quindi, è stato depositato su uno dei lati un materiale che inducesse uno stress nel silicio, tale da indebolirlo ulteriormente. In questo modo, è necessario solo un rapido raffreddamento affinché si verifichi il distacco. Le misure del tempo di vita dei portatori di carica minoritari e gli spettri Raman, insieme alle immagini SEM, sono stati utilizzati per capire come la separazione abbia modificato le proprietà degli strati superficiali di silicio monocristallino nei wafer tagliati tramite SLIM. Le stesse tecniche sono state anche impiegate per eseguire uno studio morfologico dei difetti indotti dal laser, che si trovano in profondità di campioni di silicio non separati. Il microscopio a forza atomica (AFM) ha permesso di completare l'analisi morfologica dei wafer separati fornendo informazioni sulla topografia e sul comportamento elettrico delle regioni modificate e non modificate.

I risultati ottenuti indicano che la tecnica SLIM dimezza la vita dei portatori di carica minoritari. Non risultano esserci amorfizzazione, disordine cristallino o fasi ad alta pressione. Tuttavia, i cambiamenti negli spettri Raman suggeriscono che il processo di separazione potrebbe aver prodotto uno stress residuo superficiale. La topografia AFM evidenzia le irregolarità della superficie, che potrebbero essere rimosse con una lappatura. La superficie mostra anche regioni modificate con il laser, che sono evidenti nelle immagini SEM, ma non nelle topografie AFM, suggerendo così che ci sia un effetto di caricamento del materiale durante il bombardamento di elettroni nel SEM. Infine, la caratterizzazione elettrica mediante AFM conduttivo non mostra alcuna modifica nel comportamento conduttivo del materiale dove dovrebbero essere localizzate le aree modificate con il laser.

In conclusione, questi risultati preliminari sono promettenti al fine di continuare lo studio di questa innovativa tecnica SLIM. La prospettiva potrebbe essere quella di ottimizzare le tre fasi di taglio per produrre un numero più significativo di wafer separati con le dimensioni standard richieste dal settore fotovoltaico. In questo modo si potrebbe effettuare una caratterizzazione sistematica di questa tecnica.

Contents

List of Abbreviations

2PA	–	Two-Photon Absorption
3PA	–	Three-Photon Absorption
4PA	–	Four-Photon Absorption
AFM	–	Atomic Force Microscpy
BSE	–	Back-Scattered Electrons
C-AFM	–	Conductive Atomic Force Microscpy
c-Si	–	monocrystalline silicon
Cz	–	Czochralski
DWS	–	Diamond Wire Sawing
FCA	–	Free Carrier Absorption
FCI	–	Free Carrier Induced
FTIR	–	Fourier-transform infrared spectroscopy
IBA	–	Inverse Bremsstrahlung Absorption
ITRPV	–	International Technology Roadmap for Photovoltaic
LO phonons	–	Longitudinal optical phonons
MCLT	–	Minority Carrier Lifetime
Mid-IR	–	Mid-infrared
MPA	–	Multi-photon Absorption
NA	–	Numerical Aperture
NFOM	–	Non Linear Figure of Merit
NIR	–	Near-infrared
OP	–	oxygen precipitate
PCD	–	Photo-Conductance Decay
PCE	–	Power Conversion Efficiency
PEG	–	polyethylene glycol
PV	–	Photovoltaic
rms	–	root-mean-square
SBS	–	Slurry Based Sawing
SE	–	Secondary Electrons
SLIM	–	Stress induced LIft-off Method
SPM	–	Self-phase modulation
SPM	–	Scanning Probe Microscopy
sscm	–	standard cubic centimeter per minute
SSD	–	Subsurface Saw Damage
SSPC	–	steady-state photo-conductance
TD	–	thermal donor
TM-AFM	–	Tapping Mode AFM
TO	–	Transverse Optical phonons
TTV	–	Total Thickness Variation

Introduction

Nowadays, monocrystalline silicon (c-Si) dominates the PV module market with a share of about 95% [1]. Silicon is an abundant material and the production technologies for silicon wafers are already well-established, leading to performances suitable for extended and widespread use. Indeed, silicon solar cells achieve good power conversion efficiencies (PCE) among all the PV technologies [2], with a record of efficiency of 26.7% and an average PCE of 20% for single junction cells [1, 3]. The lifetime of the modules should reach 30 years in 2022 [1] and the energy payback time of currently installed systems in European countries is $\approx 1 - 1.2$ years [3, 4]. From the environmental point of view, in the last 5-7 years, the life-cycle energy consumption and carbon and acidic emissions for c-Si PV were reduced by approximately 49% [4].[1] Moreover, advanced recycling schemes are expected to be designed to reuse silicon after the module failure. Finally, it has to be mentioned that c-Si is also employed to fabricate promising tandem solar cells with perovskites (PCE $\sim$ 30% [2]) and III-V materials (PCE $\sim$ 33% [1]).

Silicon PV technology has the major advantage of a separable manufacturing chain (see Figure 1), in which each step can be optimized independently starting from the solar-grade silicon and ingot growth to the wafering, cell processing and module assembly [3].

[1] At the moment c-Si solar cells reach $\sim$ 1000 $kgCO_2eq/kWp$, which quantifies how much CO_2 gas contributes to global warming per peak kilowatt of a module [4].

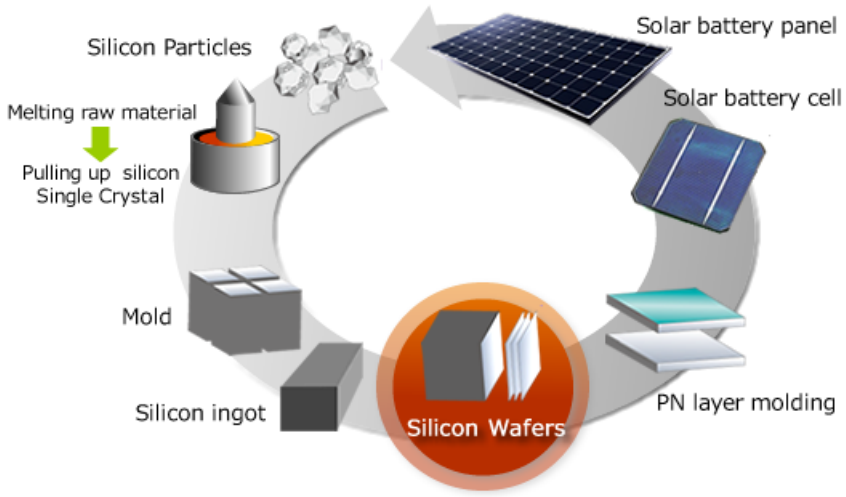

Figure 1: Manufacturing process of silicon solar cells. Adapted from [5].

The most common method to cut the ingot is the slurry-based technique: a thin steel wire is wound multiple times around guiding cylinders. The wires press SiC particles, which are suspended in a carrier liquid, onto the ingot surface and remove the material by sawing the wafers. Another common method is the fixed abrasive technique, where diamond particles are embedded into the thin wire and remove the material scratching over the surface. Nevertheless, these techniques lead to significant kerf losses from 50 μm to 200 μm [3]. For instance, the fixed-abrasive technique introduces a loss of material of up to 50% and a loss of 70% for thin layers with thickness ≤ 100 μm [6].
Alternative techniques have been implemented to solve this problem, such as epitaxial lift-off, stress-induced spalling, and Stress-induced LIft-off Method (SLIM)-cut [6]. In particular, SLIM-cut techniques are based on the simple principle of creating a layer of defects below the surface of the wafer. Then, the deposition of a stress-inducing layer on the silicon wafer surface and a cooling step is sufficient to activate the self-detachment of the thin foils of silicon [7]. Wafer separation has been achieved using Silver-Aluminium screen-printed paste, a single layer of evaporated aluminium or epoxy as the stress-inducing layer. This method paves the way for reducing the kerf losses of the wafering manufacturing step and the required amount of Si material by one order of magnitude [8].

The present work focuses on one innovative and promising SLIM-cutting, based on employing a laser of a suitable wavelength that can penetrate for a few hundred micrometres inside the bulk of the material and induce modifications at the focal spot. Several studies report that the laser-writing process was successfully achieved with Mid-infrared (Mid-IR) lasers, with the wavelength from 1.5 to 2.1

μm. The pulses were picoseconds or nanoseconds long with an energy of a few μJ [9]. Nevertheless, silicon presents several difficulties in its laser functionalization, due to its strong non-linear response to IR radiation. As a consequence, the successful realization of the buried modifications still depends on an optimization of the combination of the laser parameters.
Once the parameters are optimized, the layer with a high density of modifications is produced inside the silicon bulk and the process continues with the detachment. Within the framework of this project, the layer with a high density of defects was obtained with Mid-IR picoseconds laser pulses. The wafer obtained by the Laser Physics Group of the Norwegian University of Science and Technology (NTNU) was compared to the wafers obtained by Professor Joao Serra's research group at the Universidade de Lisboa. The latter group employed a technique slightly different from the approach chosen by the Laser Physics Group at NTNU.

This project aims to characterize the effects of the aforementioned SLIM-cutting. Thus, the study includes the analysis of the laser-induced buried modifications in thick monocrystalline silicon samples and the surface of the separated wafers. The characterization of SLIM-cut wafers should shed light on the quality of the surface, the type of modifications and their electrical behaviour. In particular, it must be assessed if the SLIM-cutting process introduces a significant amount of crystal defects, impurity contamination or loss of crystallinity in order not to compromise the PV conversion efficiency [7].
The thesis is divided as follows. In the theoretical description of Chapter 1, Section 1.1 describes the properties of monocrystalline silicon and the wafer manufacturing process, with particular attention to the wafer cutting techniques. Then, Section 1.2 contains a theoretical description of the principles of the laser-writing technique in silicon, from the propagation of the radiation to the mechanisms that lead to the modification of the material. In the last part of this section, the state-of-the-art of laser-processing with Mid-IR lasers in silicon is reported. Subsequently, the experimental results in Chapter 3 are divided as follows: Section 3.1 presents the morphological characterization of the buried laser-induced modification in bulk monocrystalline silicon wafers; Section 3.2 reports the micro-characterization of the surface of the separated wafers. Chapters 4, 5 and 6 contain the discussion of the results and the final remarks and further developments, respectively. Lastly, Appendix 6 reports the study of Focused Ion Beam as a possible choice for cross-section preparation.

Chapter 1

Theoretical Background

1.1 Monocrystalline silicon wafers: properties and production

1.1.1 Crystal structure of c-Si

Silicon is a purely covalent bonded material and crystallizes in the diamond cubic (DC) structure where atoms are coordinated tetrahedrally [10]. The conventional diamond unit cell of silicon (see Figure 1.1) can be imagined as being composed of two interpenetrating face centered cubic (fcc) lattices with a basis of two identical atoms in positions:

$$A = (0, 0, 0) \qquad B = \left(\frac{1}{4}, \frac{1}{4}, \frac{1}{4}\right). \tag{1.1}$$

The primitive cell is defined by the three vectors:

$$\mathbf{a_1} = \frac{a}{2}(0, 1, 1), \qquad \mathbf{a_2} = \frac{a}{2}(1, 0, 1), \qquad \mathbf{a_3} = \frac{a}{2}(1, 1, 0), \tag{1.2}$$

where the lattice constant is $a = 5.43$Åat room temperature [10, 11]. These vectors and the lattice parameter are highlighted in Figure 1.1. Considering Eq.(1.1-1.2), the eight atoms in the diamond unit cell are in the following positions: (0,0,0), (0,1/2,1/2), (1/2,0,1/2), (1/2,1/2,0) and (1/4,1/4,1/4), (1/4,3/4,3/4), (3/4,1/4,3/4), (3/4,3/4,1/4). Therefore all atoms in the diamond unit cell are included in the family of planes $\{100\}$ and the distance between these planes is a. However the actual distance between the atomic planes along any of the cubic axes is $a/4$, since the $\{100\}$ are equivalent to the $\{400\}$ planes. Moreover, the lines that join the four first nearest neighbors in the diamond unit cells are along the $\langle 111|111\rangle$ directions. It is important to note that five large interatomic voids in which interstitial atoms are easily accommodated are located along the body diagonals.

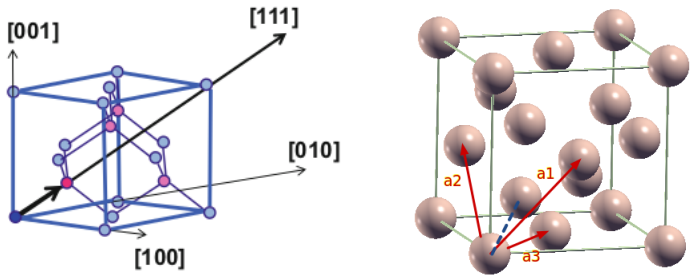

Figure 1.1: Diamond unit cell of silicon. On the left the two interpenetrating FCC unit cells are respectively shown in blue and red (reproduced from [10]). On the right the primitive vectors $\mathbf{a_1}, \mathbf{a_2}, \mathbf{a_3}$ (solid arrows) and the lattice parameter (dashed line) are highlighted.

In Cz process, the monocrystalline silicon is typically grown in the [100] or [111] directions. In Figure 1.2 the crystal orientations for the two growth directions are

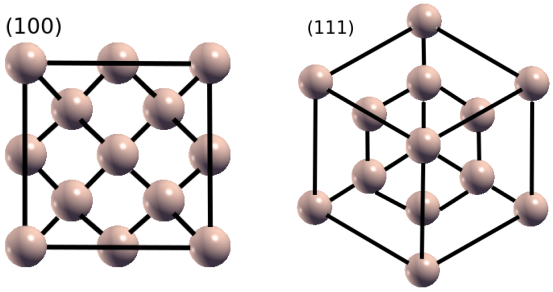

Figure 1.2: Miller planes (100) and (111) in silicon crystal structure for [100] and [111] silicon ingot growth, respectively.

shown: the (100) plane is perpendicular to the [100] growth and the (111) plane to the [111] growth.
Ingots pulled along [100] have a 4-fold symmetry. The top view of this kind of ingots appears with a squared shape with four ribs extending radially from the seed, 90° apart from each other (see Figure 1.3). The four ribs occur where the {110} planes intersect the surface of the crystal [11], which means that ribs develop in the $\langle 110|110 \rangle$ directions from the seed. The side facets consist of (111) planes which are 54.5° from the melt surface [12].
On the other hand ingots pulled along [111] have a 6-fold symmetry. The top view shows a circular shape with six ribs, which occur where the three {110} planes intersect the top of the crystal [11]. The ribs develop in the $\langle 121|121 \rangle$ directions from the seed (see Figure 1.3).

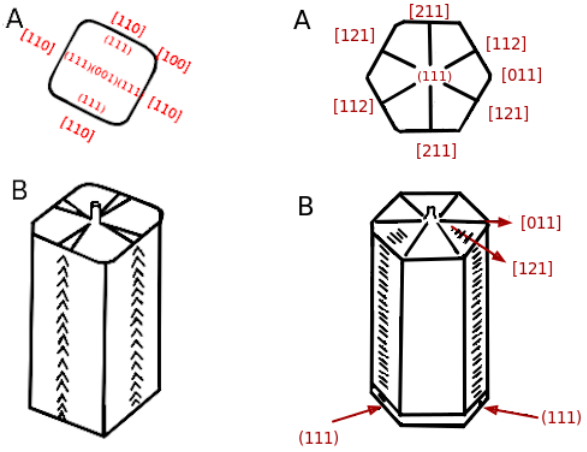

Figure 1.3: Cz [100] growth *(left)* and [111] growth *(right)*: **(a)** sketch of a top view with stereographic projection of key atomic planes and **(b)** sketch of a prospect view. Adapted from [12].

1.1.2 Electrical properties of c-Si wafers

Resistivity

In order to describe the electrical behaviour of the material, resistivity is mainly used instead of doping concentration because it is easier to measure and is given by the manufacturers. The resistivity is determined by the concentration of mobile charge carriers n (m^{-3}) and their mobility μ ($\mathrm{m}^2\mathrm{V}^{-1}\mathrm{s}^{-1}$) with the following relation:

$$\rho\ (\Omega\mathrm{m}) = \frac{1}{qn\mu}, \tag{1.3}$$

where $q = 1.602 \times 10^{-19}\mathrm{C}$ is the elementary unit charge.
For semiconductor thin films, it is better to use the sheet resistance, given by the ratio between the resistivity and the layer thickness.

Lifetime

The minority carrier lifetime measures how long the electron-hole pairs travel separately before recombination. The electron-hole pair is generated by the excitation of the semiconductor by suitable radiation, which is at an energy higher than the bandgap of the material. The diffusion length of the minority charge carrier depends on the lifetime through the following relation:

$$L_{eff}\ (\mathrm{m}) = \sqrt{\tau_{eff} D}, \tag{1.4}$$

where D (m^2s^{-1}) is the diffusion coefficient and τ_{eff} (s) is the effective lifetime. Indeed both the bulk and the surface contribute to the total lifetime: the first contains contributions of radiative recombination, Auger processes and trap-associated carrier lifetimes, while the second depends on the surface recombination velocities of the front S_f and rear sides S_r, on the wafer thickness W and the diffusion coefficient for electrons or holes $D_{n,p}$. Therefore the effective minority carrier lifetime in semiconducting wafers is expressed as [3, 13]:

$$\frac{1}{\tau_{eff}} = \frac{1}{\tau_{bulk}} + \frac{1}{\tau_{surf} + \tau_{diff}} = \sum_i \frac{1}{\tau_{bulk,i}} + \left[\frac{W}{S_f} + \frac{W}{S_r} + \frac{W^2}{\pi^2 D_{n,p}}\right]^{-1}, \tag{1.5}$$

where the sum is over all the mentioned bulk recombination processes. The surface contribution is typically approximated as $\tau_{surf} = W/2S$, neglecting the difference between the two surface recombination velocities. The surface recombination velocity is short for polished bare wafers ($S \approx 5 \times 10^4$ cms^{-1}) and long for passivated wafers ($S < 10$ cms^{-1}) [13]. For a typical p-type 300 μm thick wafer, with $D_n = 27$ cm^2s^{-1} [14] and $S \approx 5 \times 10^4$ cms^{-1} [13], the lifetime that can be expected for a non-passivated surface is $\tau_{eff} = 2.8$ μs [14]. This value would lead to $\tau_{bulk} \approx 12$ μs, using Equation 1.5.
Regarding c-Si, the limiting bulk recombination mechanism is not the radiative recombination, but the Auger one [15, 16]. The effective lifetime can be written as [15]:

$$\frac{1}{\tau_{eff}} = \frac{1}{\tau_{rad}} + \frac{1}{\tau_{Auger}} + \frac{1}{\tau_{SRH}} + \frac{1}{\tau_{surf}}, \tag{1.6}$$

where τ_{rad} is the lifetime due to radiative recombination processes, τ_{Auger} due to Auger recombination and τ_{SRH} due to Shockley-Read-Hall recombination (trap-assisted). The first two contributions are intrinsic to the material, while the second two contributions are extrinsic.

Recombination mechanisms

Briefly, Auger recombination is a three-particle interaction, where an electron-hole pair recombines and the excess energy is transferred to a third free particle (electron or hole). Several parametrizations for the Auger recombination process have been proposed. The most accepted is that of *Kerr et al.(2002)* [16], improved by *Richter et al.(2012)* [15] and *Veith-Wolf et al.(2018)* [17], which leads to having the solar cell theoretical efficiency limit of around 29.5% [3, 17]. This value is lower than the expected 32% of a semiconductor with a bandgap of 1.1 eV [18].
The Auger recombination lifetime can be written as [8]:

$$\tau_{Auger} = \frac{1}{\gamma N^2}, \tag{1.7}$$

where $\gamma = 3.8 \times 10^{-31}\text{cm}^6\text{s}^{-1}$ is the Auger recombination coefficient [19] and N is the carrier density.
The Shockley-Read-Hall model predicts that the lifetime is a function of the excess carrier density, the dopant density N_A, the density of recombination centres, the defect energy level, and the electron and hole time constants (τ_{n0}, τ_{p0}) [14]. Making the approximation that the recombination centre is near the middle of the energy gap, i.e. omitting the defect energy level, the SRH lifetime is given by:

$$\tau_{SRH} = \tau_{n0} + \tau_{p0}\frac{\Delta n}{\Delta n + N_A}. \tag{1.8}$$

Regarding the contribution of all these effects, the typical curve of lifetime as a function of the excess carrier density shows a slow increase of the lifetime, with strong contribution from SRH effect up to $\Delta n \sim 10^{16}$ cm^{-3}; for higher densities the Auger and band-to-band recombination dominate and the lifetime decreases [14].

Dependence of solar cell performances on lifetime and resistivity

As mentioned in the Introduction, this work would like to stress the importance of optimizing the silicon manufacturing process for PV applications. In this direction, both the resistivity ρ and the lifetime τ of Si wafers play a crucial role in the outcome of the cells' performance.
A simple descriptive model for the solar cells is that of a diode, with the characteristic I-V curve given by:

$$I = I_S \exp\{(\beta(V - IR_S))\} - I_L \tag{1.9}$$

where I_S is the reverse saturation current, R_S is the serial resistance due to ohmic loss and I_L is the current due to the generation of excess carriers by the absorption of the sunlight. It is relevant to notice that this expression neglects the shunt parallel resistance due to leakage current because it is much smaller than R_S.
Starting from Equation 1.9 the most useful parameters to characterize the behaviour of the solar cells can be defined:

- *short-circuit current* I_{SC} is the current when the voltage across the solar cell is zero and is due to the generation and collection of light-generated carriers; thus when $V = 0$, $I_{SC} = I_L$;
- *open-circuit voltage* V_{OC} is the maximum voltage available from a solar cell, and this occurs at zero current;
- *filling factor* (FF) is a parameter which, in conjunction with V_{OC} and I_{SC}, determines the maximum power extracted from a solar cell.

The FF is defined as the ratio of the maximum power ($P_m = I_m V_m$) from the solar cell to the product of V_{OC} and I_{SC}: $FF(\%) = P_m/(V_{OC} I_{SC})$. The FF is a useful parameter because it quantifies how much power can be concretely converted. In Figure (1.4) two examples of FF are shown: the low FF is due to a smaller maximum power relative to the power given by $V_{OC} \times I_{SC}$, while the highest FF is obtained when the two powers are the same.

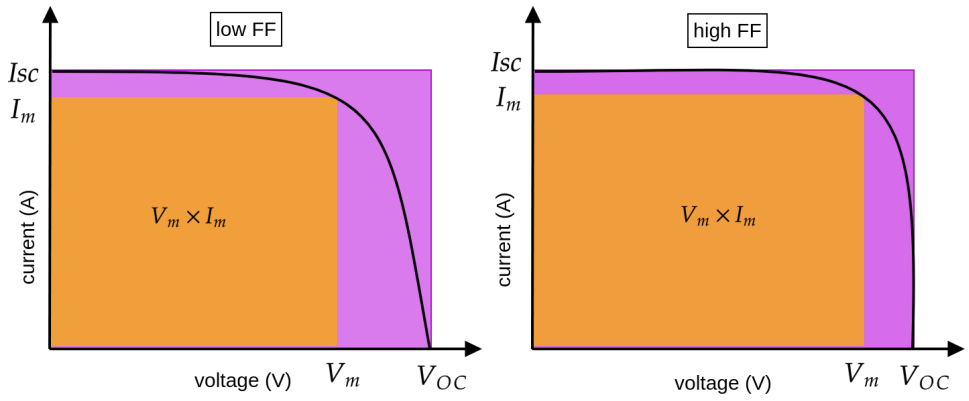

Figure 1.4: Graph of cell output current as a function of voltage. The open-circuit voltage V_{OC} and the cell short-circuit current I_{SC} points are also shown. The purple rectangle is given by $V_{OC} \times I_{SC}$ and the orange rectangle by $V_m \times I_m$. On the right side an example of high FF is shown, while on the left side of low FF.

Aiming to quantify the performances of a solar cell, the power conversion efficiency (PCE) can be used as one of the main parameters. The PCE is the ratio between the maximum power that the cell generates and the input power:

$$PCE(\%) = \frac{P_{max}}{P_{in}} = \frac{I_{SC} V_{OC} FF}{P_{in}}. \tag{1.10}$$

As the name suggests, a higher PCE corresponds to better performance.
V_{OC}, and therefore FF, strongly depends on the effective lifetime of the material. Indeed V_{OC} has the following behaviour [20]:

$$V_{OC} \approx \frac{k_B T}{q} \ln\left(\frac{\Delta p(\Delta p + n_0)}{n_i^2}\right), \tag{1.11}$$

where the equation considers n-type c-Si with generated excess carrier density Δp, doping level n_0 and intrinsic carrier density n_i. In Section 2.2.1, Eqs.(2.3-2.4) will show that Δp is governed by the lifetime: upon reducing τ, the carrier injection decreases and therefore V_{OC} drops [14]. It was seen that the drop is

more pronounced for higher ρ since the lower n_0, in that case, does not help counterbalance the harmful effect of lowered Δp [20].
The FF is also affected: for high ρ (low n_0) and a low τ (low resulting carrier injection) the effect is extremely detrimental since the resistive losses associated with the majority electron transport through the bulk are not prevented and lead to a FF drop. Considering Eq.(1.10), the efficiency will also drop. The FF drop is mitigated for lower ρ due to the higher majority electron concentrations n_0, promoting efficient electrical conduction [20].
The last effect of a low lifetime is the reduction of I_{SC}, due to the reduction of the diffusion length and hence a reduction in the collection efficiency.

1.1.3 Czochralski growth

Czochralski (Cz) silicon detains the major share of the current market for the fabrication of high-efficiency solar cells in the PV industry [3]. The World Market Share of p-type and n-type mono-Si is supposed to increase from 87% in 2021 to 100% in 2032 [21]. Indeed Cz growth process allows obtaining silicon wafers with low defect density and a well-textured surface with low reflectance, which are two requirements for PV device technology. In particular, the Cz process allows the growth of single crystals from high-purity polycrystalline silicon ($> 99.9999\%$ [22]). Moreover, the crucible can be recharged while still hot and three to five ingots can be pulled without cooling and breaking the controlled atmosphere [3]. However, the Cz process is less productive than multicrystalline silicon, having a growth rate of $\sim$ 1mm/min [23].

The Cz process takes place in the crystal puller, which consists of an air-tight, water-cooled growth chamber and a crystal harvesting chamber. In the growth chamber, usually made of stainless steel, there are the heater and the graphite cup. The latter supports a quartz crucible that contains polysilicon charges. The graphite cup is on a graphite pedestal which rotates in the opposite direction of the seed holder, which holds the seed used for the single crystal growth.
During crystal growth, the puller chamber is purged with an inert gas like argon or nitrogen with a reduced pressure ($\sim$ 20 mbar [23]).

Figure 1.5 depicts the pulling procedure. The polycrystalline silicon melts in the quartz crucible, and after the melt is thermally stable, the seed is dipped. When the seed starts to melt, it is gradually withdrawn from the melt. In order to obtain dislocation-free ingots the Dash necking technique is used [22]: the diameter is strongly reduced up to 3-6 mm [23] and the so-called "neck" is grown up to a few centimeters in length when the crystal becomes dislocation-free. Afterwards, the pulling rate is decreased and the diameter starts to grow up to the desired dimension; this part of the ingot with variable diameter is called "shoulder/crown". The length of the main body is typically 15-20 cm [23]. After the crystal cylinder

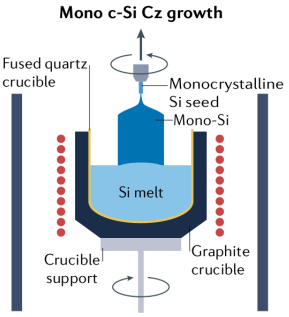

Figure 1.5: Schematic representation of Cz growth furnace and process. Adapted from [3].

is finished, the crystal diameter has to be reduced gradually to a small size and an end-cone is formed. For this purpose, the pulling rate is raised and the crystal diameter decreases.

1.1.4 Wafering techniques

The next step after the growth of the silicon ingot is cutting the thin wafers. The need of extremely thin wafers and reduction of the kerf losses is mainly due to the high cost of silicon material, which represents the 44% of the final module cost [21]. In fact, this requirement is now stronger than the previous years because the contribution of polycrystalline silicon cost, employed in Cz-growth, was 17% at the end of 2020 [24], while it increased to 44% during 2021 due to capacity shortages. In 2021 the required thickness for small and medium size[1] p-type and n-type wafers was 165 μm and 160 μm, respectively. It is expected to be reduced to 140 μm and $\sim$ 127 μm in 2032 [21].

The Total Thickness Variation (TTV), the wafer cleanness and the Subsurface Saw Damage (SSD) are the most common parameters that quantify the quality of a cutting technique. Indeed a uniform thickness, a low TTV ($<$ 25 μm) and roughness, a low SSD, and a high surface cleanness are the requirements for PV applications [25].
The previous parameters are defined as follows [25]:

- TTV is the change of the wafer thickness, which is ideally zero;
- SSD consists of microcracks below the surface, up to 20 μm in length, or of

[1]The required thickness depends on the size of the wafers. Here, medium-sized wafers here are wafers with an area equal to 166 mm $\times$ 166 mm and this format dominates the PV technology. Larger wafers ($>$ 210 mm $\times$ 210 mm) are between 5 μm and 7.5 μm thicker [21].

thin layers of silicon material that transforms into an amorphous or micro-crystalline structure;

- the wafer cleanness depends on the contamination with impurities and organic residues from the sawing and cleaning process; this parameter can influence the etching and texturing steps compromising the quality of the finished wafer.

The following sections describe the two main cutting methods: Slurry-based sawing (SBS) and Fixed Abrasive Sawing or also called Diamond Wire Sawing (DWS). Then the state-of-the-art for kerfless cutting techniques is presented. Indeed, these latter methods may offer an alternative, aiming to obtain thinner wafers (~ 50 μm [26]) without kerf losses. However, it must be kept in mind that kerf losses are not only due to the loss of material produced during the cutting step, but it is also due to the etching and texturization steps, which are required to remove the surface damage caused by sawing and contamination. Therefore, it may result that also the so-called "kerfless" techniques have some amount of material loss.

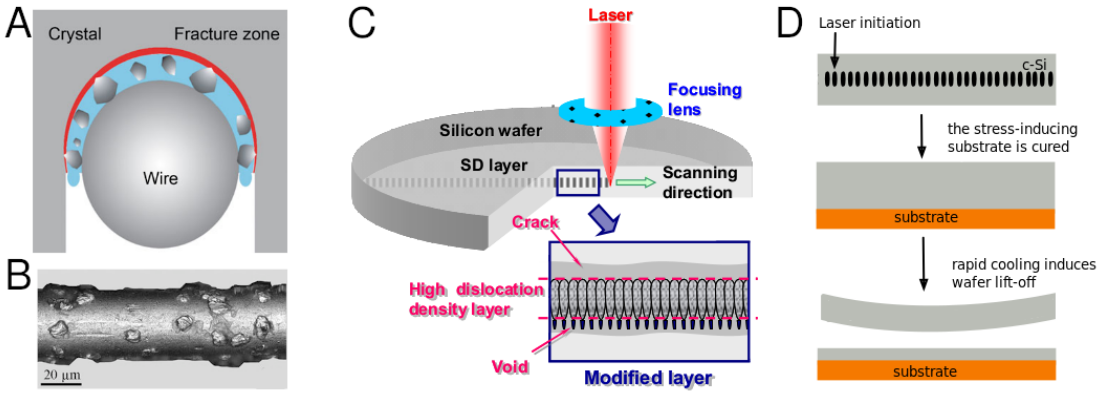

Figure 1.6: **(a)** Schematic view of the slurry-based cutting method [25]. **(b)** Diamond-coated wires for fixed-abrasive cutting method with electroplating bonding [26]. **(c)** Stealth Dicing laser processing [27]. **(d)** Basic spalling process for SLIM-cutting.

Slurry-based sawing

Before the introduction and optimization of the DWS in 2018 [21], the SBS dominated the silicon wafering industry. Figure 1.6a shows the basic setup for SBS. The physical model is based on the "rolling-indenting grain" [26]: free-floating abrasive particles are suspended in a carrier fluid and a steel wire pushes these particles onto the silicon surface. Then the rolling and indenting of the abrasive

particles cause the removal of the material (see Figure 1.7a). Only the larger particles are in direct contact with the silicon surface and induce the formation of lateral cracks and the chipping of material.

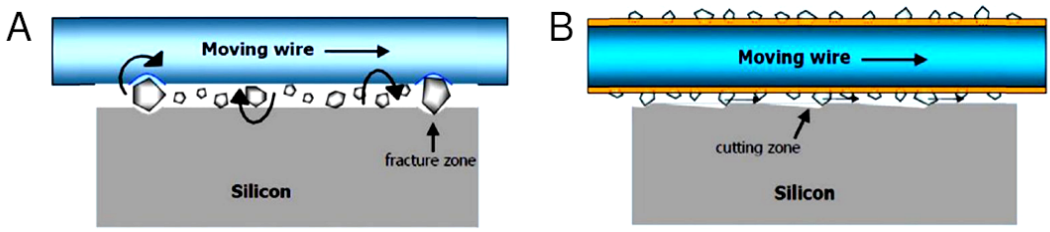

Figure 1.7: Schematic representations of the sawing mechanisms: **(a)** SBS and **(b)** DWS. Adapted from [28].

The most commonly used abrasive particle is SiC, with grain size between 2 and 15 μm [26]. These particles are faceted and their sharp edges exert very high local pressures. Due to the fact that only the largest particles are responsible for the removal of material, it is possible that a SiC powder is within the specification but does not work properly because the size distribution of the larger particles differs [25].

The carrier fluid, also called slurry, must have good transportation capability for the abrasive powder and it must be able to carry the silicon and metal debris out of the sawing channel. This translates into requirements for the viscosity, which is kept in the range 0.05-0.2 Pa·s [26]. Therefore, the commercial slurries are now based on polyethylene glycol (PEG)-based fluids, which have a viscosity of $0.07 - 0.09$ Pa·s [25] depending on the composition. The viscosity requirement is also satisfied by oils ($\eta = 0.06 - 0.2$ Pa·s), which were the most used in the past. Oils are more difficult to recycle and make the wafer cleaning more challenging [26].

From the environmental and economic point of view, water would be a better liquid because it does not require any recycling chain and is the cheapest liquid available. Nevertheless, its low viscosity (0.001 Pa·s [25]) is not suitable for SBS and this would require additives to improve the SiC transport. Moreover, water vaporizes quickly inside the sawing machine, causing the SiC particles to clog the apparatus (filters, tubes, etc). Even more significant is the hydrogen production due to the water-silicon interaction, which increases the risk of explosions during the cutting process [26].

SBS has many drawbacks. The steel wires become 8-10% thinner after one cut and are not recyclable because they must be discarded as metal scrap [26]. Considering also that the use of PEG slurry increases hazardous waste emissions and makes it more expensive to recover silicon debris from the slurry, SBS is not

as sustainable as DWS [28]. The kerf loss is around 120-140 μm per wafer, which is almost the same as the final wafer thickness. Lastly, the optimization of the process implies taking into account the effect of several parameters. Thus the nominal viscosity of the slurry and the nominal size of the SiC is not sufficient to determine the successful wafer cutting. For instance, the viscosity depends on the temperature, the SiC and debris concentration and also on the particle shape [26]. Moreover, the wire dimension, speed and tension, the cutting speed and the diameter of the sawing channel are important parameters.

Sawing with structured wires is one of the possible solutions. They contain periodic kinks which ensure a more stable sawing process. Indeed the kinks allow a better transport of the slurry along the sawing channel, preventing the appearance of saw marks on the wafers. With structured wires, the sawing capacity of a wire saw is doubled, due to a faster table speed and the energy consumption is reduced by 2/3 relative to straight wires for SBS [29]. This technology is also beneficial because it reduces the TTV and the replacement costs of wires and slurry. Indeed sawing with structured wire has a 74% lower total cost/wafer than SBS [26].

Fixed Abrasive sawing

The introduction of diamond wire sawing (DWS), completed in 2018 [21], has enabled significant reductions in the kerf width. In this case, the steel wire is directly coated with highly abrasive particles, i.e. diamond, as shown in Figure 1.6b. Two methods are typically used to fix the particles: resin bonding and electroplating bonding. The former is cheaper but leads to a weaker bond. The latter gives a stronger bond because the particles are embedded in a nickel-coating layer, but the technique is more expensive [26, 28].
For DWS the removal of the material is different from SBS because it is the scratching of diamond particles over the crystal surface (see Figure 1.7b). Similarly to SBS, not all the particles are in contact with the ingot and the indentation depth varies depending on the particle size. Thus the scratches have different depths too.

The sawing process must take place in a sawing fluid, which is necessary to cool both the wire and the ingot and carry the silicon kerf out of the channel. Contrary to what happens for the SBS, water-based liquids are suitable for DWS because of the absence of SiC particles. Additives are still needed to ensure the removal of the kerf and the protection of the wire against corrosion [26].

Despite the expensive cost of the diamond, DWS technology has several major advantages. Firstly, the wire can be used more than once, due to the specific "pilgrim" sawing mode, where the wire is running back and forth and in each cycle a few meters of new wire are added. This sawing mode also leads to a yield production 2 or 3 times higher than SBS [28].
Secondly, considering the results of the International Technology Roadmap for

Photovoltaic (ITRPV) 2022 [21], the kerf loss of DWS is 60 μm, but is expected to be reduced to 8% already in 2022 and should be further reduced to 30% in 2032. This reduction allows saving more material. The TTV is typically 10 μm in DWS [21].
In addition, DWS is more sustainable than SBS because water-based cutting fluids are suitable. Thus the costs of waste post-treatment and silicon recovering from the cutting fluid are reduced [28]. Lastly, the silicon wafers obtained by DWS have higher strength and longer service life [28].
DWS has 74% and 33% lower total cost/wafer than SBS if diamond particles are bonded with nickel or resin, respectively [26].
The significant disadvantage of DWS over SBS is that diamond-coated wires are more prone to breaking, getting stuck in the channel and winding up in the spools. Both techniques have the major drawback of metal contamination of the silicon surface. In particular, the contaminants come from the damaged steel wires and their coating with iron, nickel, copper, boron, phosphorous, etc. Oxygen is also a typical contaminant because the small silicon particles, which form the kerf, can accumulate large amounts of oxygen and easily oxidize. Directional solidification is a partial solution to the metal contamination because the metal impurities are transported to the top of the ingot, which is removed. However carbon, oxygen, aluminum, boron and phosphorous are difficult to remove since their segregation coefficients are closer to one [22].

Kerfless SLIM-cut

Aiming to reduce the cost of wafer production, a solution to the problem of kerf loss must be found. Figure 1.6a is a clear example of the reason why wire sawing induces kerf losses of at least the wire diameter. Kerfless techniques are based on the simple principle of producing the detachment of thin layers without significant loss of the material by exploiting different methods.
Among the most advanced separation techniques is the cleaving process after ion implantation[30], where protons are implanted in a thin layer at a controlled depth under the surface of silicon. Roughness and TTV are typically less than 1 μm and 1-2%, respectively [26]. Differently, direct epitaxial growth of high-quality silicon is possible if the silicon is grown on a substrate layer and a porous separation layer. Then the thin film is separated from the substrate breaking the small supporting pillar in the separation layer and subsequently, the thin film is transferred to another substrate. However, these methods are difficult to be transferred to the industry, since processes and costs related to weakening the silicon samples stay relevant [31].

Another interesting method relies on the induction of a layer defects employing laser radiation at lower energy than the silicon band gap, where the material is

transparent (wavelength higher than 1.12μm). This technique is often referred to as Stress-induced LIft-off Methods (SLIM) and is extremely different from the normal use of lasers for cutting. Indeed the SLIM-cutting requires to form a modified layer inside the material reducing the surface damage as much as possible. The physical mechanisms behind the modification of the silicon bulk are presented in Section 1.2, but now the focus will be on the detachment part that follows the laser modification step.

The SLIM-cut technique has two main applications, one is the previous mentioned wafer cutting and the other is the silicon chip formation. This particular kind of SLIM-cut method is called "stealth dicing" and was developed as an innovative dicing method by Hamamatsu Photonics K.K. [27].
Figure 1.6c depicts the laser processing step, where a layer of defects is induced at a controlled depth. As is presented in Section 1.2.2, the defects are elongated in the laser direction. Regarding wafer cutting, the technique consists of three steps [31]:

1. displaying a stress-inducing layer on the silicon wafer surface and curing at high temperature;

2. a cooling step to activate the stress and detach a thin foil of silicon;

3. a chemical cleaning to obtain a flat thin silicon foil.

During the cooling step, the difference between the thermal expansion coefficients of silicon and the stress-inducing layer creates a local high stress increase at the defect layer, which induces crack propagation [30]. It has been demonstrated that cooling at room temperature work for foils with thicknesses from 80 to 150 μm, while liquid nitrogen is necessary for foils with thicknesses between approximately 50 and 100 μm [32].
The choice of the stress-inducing layer is non-trivial. Indeed the substrate-silicon interface must have an interfacial strength high enough for the crack to propagate in the Si lattice [33]. Moreover, the process must be compatible with PV cell processing, which translates into compatible deposition methods and control over the introduction of defects and impurities. Examples of efficient stress-inducing layers are double screen-printed Silver/Aluminum layer [32], dispensed epoxy paste [7, 30, 31], and electrodeposited Nickel [33, 34].

Bellanger et al. [30] reported the first solar cells fabricated on SLIM-cut silicon foils: they manually dispensed a Stycast epoxy layer as the stress-inducing layer and obtained a silicon foil with a thickness of 130 μm and maximum roughness height of 37.4 μm. However, they also demonstrated in a later work that the thickness can be varied between 40 and 140 μm by changing the epoxy thickness [32].

The process is not only limited to the production of one wafer because one can induce several defect layers at different depths. Then the foil extraction is induced from the defect layer that is closer to the upper surface [31] and subsequent steps of epoxy deposition and separation allow cutting more wafers from the same bulk silicon. *Serra et al.* [31] observed that the foil preserves the initial shape of the starting substrate, but successive foils are thinner. This is attributed to the fact that the parent substrate is becoming thinner while the stress-inducing layer thickness is unchanged between SLIM-cuts. They suggest adjusting the epoxy thickness for every step. Interestingly, the same research group found that the dislocation density increases from $2 \times 10^5 \mathrm{cm}^{-2}$ to $6 \times 10^5 \mathrm{cm}^{-2}$ as successive foils are extracted from the same parent substrate [7].

SLIM-cut for PV applications has still to be optimized. For instance, *Bellanger et al.* [32] reported conversion efficiencies of 12.5% and 13.8% using 55 μm and 120 μm thick Si foils and epoxy during the separation procedure, while *Yang et al.* [34] obtained an efficiency of 14.23% with 50 μm thick silicon foils detached from a nickel substrate.

Although SLIM-cutting has a good application potential, the high requirements for optical systems limit its application to a certain extent.

1.2 Laser-induced bulk modifications in silicon

This section presents the theoretical description of the laser-beam propagation inside silicon and the modifications that are induced in the material. The basic idea is to exploit non-linear properties of silicon, i.e. non-linear reactions that are triggered by the IR laser focused into a tiny volume ($\sim \mu\text{m}^3$ [35]), to optically induce mechanical stresses within the Si bulk. These mechanisms are self-phase modulation (SPM), self-focusing, multi-photon absorption (MPA) and avalanche ionization, which are going to be described in Section 1.2.1. Furthermore, in Section 1.2.2 a review of the morphology of the induced modifications is presented. Lastly, Section 1.2.3 presents the state-of-the-art of laser induced modifications in bulk silicon.

1.2.1 Beam propagation and radiation-matter interaction

The propagation of a linearly polarized electromagnetic wave is described by the non-linear Schrödinger equation in the slowly varying envelope approximation [6, 36]:

$$\frac{\partial E}{\partial z} = \frac{i}{2k_0}\left(\frac{1}{r}\frac{\partial}{\partial r} + \frac{\partial^2}{\partial^2 r}\right) + \frac{ik_0 n_2}{n_0}|E|^2 E - \frac{1}{2}\sum_K \beta^{(K)}|E|^{2K-2}E - \frac{\sigma}{2}(1+i\omega_0\tau_c)NE. \tag{1.12}$$

The first term is the diffraction term dependent on the wavenumber k_0 at the pulse central frequency ω_0. The second term considers the optical Kerr effect, which is a non-linear effect of self-phase modulation and self-focusing. This term depends on the linear refractive index n_0, the non-linear refractive index n_2 and the complex magnitude of the electric field E. Here $|E|^2 = I$, with I as the intensity of the laser beam. The third term accounts for the $K-$photon absorption (MPA), with the coefficient $\beta^{(K)}$. The last term is for the free carrier absorption (FCA) plasma and defocusing. The FCA term depends on the cross-section for the inverse *bremsstrahlung* absorption (IBA) σ, the free carrier plasma momentum scattering time $\tau_c = 3.5$ fs [36] and the free carrier plasma density N. IBA is the process in which an electron absorbs a photon while colliding with an ion or with another electron and the cross-section can be evaluated as:

$$\sigma = \frac{q^2 k_0 \omega_0 \tau_c}{[n_0^2 \omega_0^2 \epsilon_0 m(1+\omega_0^2\tau_c^2)]}, \qquad \text{with } m = \frac{m_e^* m_h^*}{m_e^* + m_h^*}, \tag{1.13}$$

where q is the the elementary electronic charge, ϵ_0 is the permittivity of free space and $m = 0.15 m_e$ is the reduced optical mass of electron-hole pairs in silicon [19]. Therefore σN describes the absorption of light by free carriers created by interband transition [37].

The propagation of the laser beam implies that the incident radiation interacts and deposits energy in the bulk in a way that can be schematized as in Figure 1.8. The scheme considers the excitation by a single photon with energy higher than the silicon bandgap (E_g). As mentioned above, the absorption of the radiation can occur via interband MPA or FCA (see Eq.1.12). Interband absorption implies that an electron-hole pair is generated and the created free carriers will have excess kinetic energy equal to $\hbar\omega_0 - E_g$. Then it can be assumed that the carriers will thermalize into Fermi-Dirac distribution functions at sufficiently high densities such that carrier-carrier collisions occur on a time scale faster than 100 fs [19]. These distribution functions of electrons and holes share the same tempera-

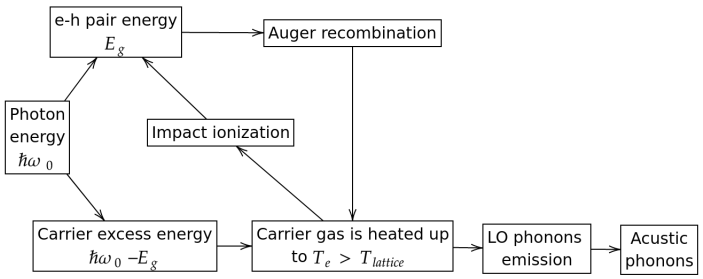

Figure 1.8: Evolution of laser deposited energy in the carrier and lattice system for single-photon excitation. From [19].

ture T_e. At this point, the carriers attempt to reach thermal equilibrium with the lattice (at $T_{lattice}$) through the emission of longitudinal-optical (LO) phonons on a time scale defined by the electron-phonon coupling time. In silicon, this time scale for LO-phonons channels is $\tau_e < 500$ fs [8], which implies that on the time scale of the laser pulse (typically ps and ns), the kinetic energy of the free carriers is instantaneously converted to lattice energy. Indeed ps and fs pulse durations are long enough to consider that the electron–phonon relaxation time is instantaneous [38]. Then the LO-phonons will attempt to thermalize with other lattice modes through phonon-phonon interactions.
In the meantime, recombination takes place to reduce the density of generated carriers. Auger recombination is the dominant process for carrier densities $N > 10^{18}$ cm^{-3}, involved in the laser-induced excitation of silicon [8, 15–17, 19]. The inverse process of Auger recombination is impact ionization when an energetic carrier creates an electron-hole pair losing energy. These two processes are responsible for achieving particle number equilibrium at the same temperature T_e.

Therefore, considering also MPA, the particle balance is given by [19, 37]:

$$\frac{\partial N}{\partial t} = G + R - \nabla \cdot \mathbf{J}, \tag{1.14}$$

where G is the pair generation rate, R the pair recombination rate and $\mathbf{J}$ the carrier pair current given by [37]:

$$\mathbf{J} = -D_0 \left(\nabla N + \frac{N}{2k_B T_e} \nabla E_g + \frac{N}{2T_e} \nabla T_e \right), \tag{1.15}$$

where the electron diffusivity is $D_0 = 1.8 \times 10^{-3}(300/T_l)$ and T_l is the lattice temperature. In general, the pair generation takes into account the K-photon absorption (MPA), thus [36, 37]:

$$G = \sum_K \frac{\beta^{(K)} |E|^{2K}}{K\hbar\omega_0}, \tag{1.16}$$

where $I \equiv |E|^2$ is the beam intensity.
The pair recombination must take into account Auger and impact ionization processes as follows [37]:

$$R = -\gamma_{Au} N^3 + \delta(T_e) N, \tag{1.17}$$

where γ_{Au} is the Auger coefficient of Equation 1.7 and $\delta = 3.6 \times 10^{10} \exp\{-1.5 E_g / k_B T_e\}$ s^{-1} is the impact ionization coefficient [19].
Nevertheless, some approximations can be made when dealing with ultra-short laser pulses propagating in silicon. The assumptions are summarized as follows:

- the MPA absorption process is mainly responsible for beam attenuation. However, the linear absorption coefficient $\alpha \equiv \beta^{(1)}$ is low for the considered laser wavelengths, e.g. $\sim 10^{-8}$ cm^{-1} for 1550 nm [35]. The two-photon absorption (2PA) coefficient is $\beta \equiv \beta^{(2)} \approx 1 \times 10^{-11}$ m/W for 1500 nm and decreases to ~ 0 for above 2000 nm [39]. The three-photon absorption (3PA) coefficient is $\gamma \equiv \beta^{(3)} \approx 3 \times 10^{-26}$ $\mathrm{m}^3/\mathrm{W}^2$ for 2600 nm and decreases to $\approx 0.3 \times 10^{-26}$ $\mathrm{m}^3/\mathrm{W}^2$ below 1500 nm and above 3000 nm [40]. The reported values make 2PA the main ionization mechanism for the considered range of wavelengths [9];

- the impact ionization coefficient is relevant for pulses longer than 10 ps [6, 36] and for the free carrier densities that are considered in this work ($N > 10^{19}$ cm^{-3}) is negligible because its rate is a few orders of magnitude smaller than Auger recombination [8];

- similarly, for the carrier density considered, SRH recombination is negligible relative to Auger recombination [38];

- the FCA for ultra-short pulses ($< ps$) only increases the carrier temperature without triggering avalanche processes [36]. Moreover, avalanche ionization is limited for fs- and ps- pulses independently of the initial doping concentration [9], but its influence compared to MPA increases for longer pulse lengths [41];

- the carrier diffusion is negligible because the diffusion length is much smaller than the smallest diameter of the beam in silicon [8]. For instance, for a pulse with duration $\tau_{pulse} = 3$ ns, the diffusion length would be $L_{diff} = \sqrt{6D\tau_{pulse}} = 1.8$ μm at 300 K, while the beam focus would be 3 μm;
- the recombination processes do not affect the plasma density for ultra-short laser pulses (sub-ps) because the plasma lifetime in silicon is long $\sim 1 - 10$ ns [6, 36].

The aforementioned assumptions lead to approximate Equation 1.14 to:

$$\frac{\partial N}{\partial t} = \sum_K \frac{\beta^{(K)}|E|^{2K}}{K\hbar\omega_0}. \tag{1.18}$$

Therefore, the attenuation of the laser intensity with the depth of the absorption z becomes [6, 19, 35, 37]:

$$\frac{\partial I(t,z)}{\partial z} = -\sum_K \beta^{(K)} I^K - \sigma N I \approx -\beta I^2(t,z) - \gamma_{Au} I^3(t,z) - \sigma N I(t,z). \tag{1.19}$$

Heat generation mechanisms

The considerations of the previous section lead to the definition of three main mechanisms for heat generation after the beam propagation (see also Figure 1.8). The first mechanism is the heat generated by MPA. Since the present case deals with high intensities, the two-photon absorption (2PA) is dominant and the single-photon absorption is negligible in the total heat generation rate. For simplicity, the absorption of a higher number of photons is not considered now because the 2PA is relevant in the wavelength range around 1550 nm, while 3PA becomes dominant above 1960 nm [6]. The heating rate for 2PA is [8]:

$$Q_{2PA} = \beta I^2 \left(1 - \frac{E_g}{2\hbar\omega_0}\right). \tag{1.20}$$

The second mechanism is Auger recombination with:

$$Q_{Auger} = E_g \gamma_{Auger} N^3. \tag{1.21}$$

The third is free carrier absorption (FCA) because conduction electrons can absorb photons through intraband absorption, which leads to heating. The heating rate is:

$$Q_{FCA} = \Delta\alpha_{FCA} I, \tag{1.22}$$

where $\Delta\alpha_{FCA}$ is the absorption coefficient given by the Drude model [42]:

$$\Delta\alpha_{FCA} = \frac{e^3\lambda^2\Delta N}{4\pi^2c^3\epsilon_0 n}\left(\frac{1}{m_{ce}^{*2}\mu_e} + \frac{1}{m_{ch}^{*2}\mu_h}\right), \tag{1.23}$$

where e is the electronic charge, ϵ_0 is the permittivity of free space, n is the refractive index of unperturbed c-Si, m_{ce}^* is the conductivity effective mass of electrons, m_{ch}^* is the conductivity effective mass of holes, μ_e is the electron mobility, and μ_h is the hole mobility. The typical value is given by [8]:

$$\Delta\alpha_{FCA} = \Delta\alpha_h + \Delta\alpha_e = 0.51\times10^{-20}\lambda^2TN + 1.01\times10^{-20}\lambda^2TN, \tag{1.24}$$

which depends on the temperature T.
For the theory presented in Section 1.2.2, it is important to say that the FCA intraband absorption coefficient $\Delta\alpha_{FCA}$ (Eq.1.23) is linked by Kramers-Kroning relations to the free carriers induced (FCI) change of the refractive index Δn_{FCI} [42]. Therefore [8]:

$$\Delta n_{FCI} = \frac{e^2\lambda^2\Delta N}{8\pi^2c^2\epsilon_0 n}\left(\frac{1}{m_{ce}^{*2}} + \frac{1}{m_{ch}^{*2}}\right). \tag{1.25}$$

In conclusion, the total heating rate is $Q_{tot} = Q_{2PA} + Q_{Auger} + Q_{FCA}$. However, for ultra-short laser pulses, Q_{Auger} term could be omitted [6, 36].
In the following section the relevance of the heat generation inside the silicon bulk will be evident, due to the crucial role of melting in the modification process.

1.2.2 Induced modifications of the silicon properties

This Section firstly presents a description of the morphology of the laser-induced modifications, with particular attention to the mechanisms that lead to defects with a peculiar tear-drop shape. In the second part, this Section describes the formation of elongated structures instead of single tear-drop defects, which is an interesting phenomenon to consider in multi-pulse laser-writing processes.

Morphology of the single induced modifications

The formation of the defects at the focus spot is induced by the generation of the electron plasma cloud that exerts mechanical stresses on the silicon lattice [35]. The carrier-phonon interactions lead to the re-distribution of energy among the carriers and lattice, causing the lattice temperature to rise to the melting point [43]. After the melting and fast resolidification of the excited region, a high dislocation density layer forms due to the large compressive stress [27], with tensile stress perpendicular to the modified layer [44]. Therefore, melting and fast resolidification are the main cause of laser-induced damage [45, 46].

Figure 1.9e depicts the morphology of the induced modifications. The formation mechanism is the following:

1. the laser induces the melting of silicon in the region of the focal spot;

2. a void forms since the volume of the molten silicon is less than that of the monocrystalline silicon [38]. Indeed, the molten silicon is 10% denser than diamond cubic silicon [46]. The void forms significantly before the focal spot [6, 38, 44] because of the non-linear absorption in the prefocal region, where the critical intensity for material modification must have already been reached [6];

3. the melting region expands upward in the direction of the laser beam because of the increase in the absorption coefficient with increasing temperature (Figures 1.9a-b) and it propagates as a thermal shock wave [27]; the molten region expansion stops at the end of the pulse duration;

4. the thermal diffusion around the focal spot induces recrystallization by cooling the molten silicon (Figure 1.9c). Thus, the void is separated by the recrystallized area from the remaining molten silicon (Figure 1.9d) because the release of latent heat of crystallization can retard the resolidification process in the central region [47];

5. lastly, the molten silicon resolidifies with the restriction of atom transfer and eventually converts to the disordered region (Figure 1.9e) [38]. Residual stress generates due to the expansion on resolidification of the trapped molten silicon.

The modified area has a tear-drop shape with a void at the sharp end. The disordered region is surrounded by cracks, while the void lacks surrounding crack marks. The crack formation is not due to mechanical stress generation around the void but is rather due to the stress surrounding the disordered region [38]. It has also been observed that in the border regions, the time for recrystallization is too small for the formation of crystallites and the surface solidifies into an amorphous state located in an annular zone around the recrystallized regions [47]. *Verburg et al.* [46] detected high-pressure phases along defect lines that were presumably formed by the overlap of adjacent resolidification fronts and they suggested that the melt solidifies into Si-III/Si-XII phases of a similar density. The presence of polycrystalline and amorphous phases has also been confirmed by several recent studies [9, 37, 43, 48–51]. *Zhang et al.* [37] observed that the amorphization preferentially takes place on the (111) crystallographic surface because this is the crystallographic close-packed plane and has the smallest surface energy since Si has a fcc lattice structure. This means that the growth speed of this plane is the

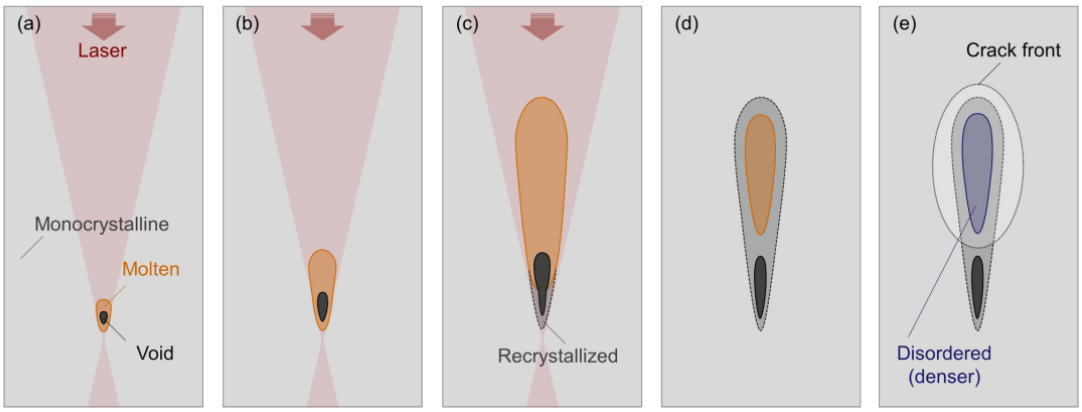

Figure 1.9: Schematic illustrations from *Kiyota et al.* [38] of the phase transition sequence arising in a single pulse. The laser melts the silicon and induces the formation of a void (a), then the molten silicon expands (b) and the outer region of molten silicon starts to recrystallize due to cooling (c) separating the void from the molten region (d). The resulting morphology has a tear-drop shape with a void a the sharp end, an elliptical disordered region of solidified silicon surrounded by recrystallized silicon (e).

smallest and the amorphization may be more energetically favourable than the crystallization with the same solidification rate.

In addition to these general considerations about the morphology of the induced modifications, it must be mentioned that the shape of subsurface modification depends on the laser pulse energy, scanning speed, repetition rate, and input beam shape. For instance, *Wang et al.* [48] observed that the modifications become larger with increasing pulse energy, and the length and width of the modification decrease with the increasing scanning speed, but increasing the repetition rate increases the length and the width. *Kammer et al.* [41] saw that the probability of inducing an in-volume modification in silicon increases with pulse duration. Sometimes, employing femtosecond laser pulses the modifications consist of stress, without the presence of void [52], which can be explained by the non-thermal melting mechanism caused by femtosecond laser. In the non-thermal melting process a strong optical excitation may lead to a destabilization of the bonding lattice structure on an ultrafast (sub-ps) timescale [50] and induces mild heating, smaller thermal gradient, and slower cooling compared with nanosecond laser [37].
In conclusion, *Yu et al.* [53] interestingly observed that the modification morphology does not depend on the wafer doping with initial carrier density in the range of $10^{13} - 10^{16}\text{cm}^{-3}$. However, at a higher density of 10^{18}cm^{-3}, linear absorption of light before the focus reduces the in-target pulse energy and thus the size of the induced modification.

Principles of the formation of elongated structures

Aiming to understand the principles of the formation of elongated structures inside the Si bulk, it is useful to consider that from the optical point of view the induced modifications are described by the change of the local bulk optical properties. Following the theory presented in Section 1.2.1, the two main diffractive effects are the thermally induced and free carrier induced change of the refractive index, Δn_{th} and Δn_{FCI}, respectively. The first is given by $\Delta n = n_2 I$ with n_2 as the non-linear refractive index and I as the pump intensity [9]; the latter is given by Equation 1.25. From the optical point of view, these two effects are described by two characteristic focal lengths, f_{th} and f_{FCI}, respectively.
For a single incident pulse $f_{th} > |f_{FCI}|$, which leads to a negative Δn_{FCI} and a shielding effect that prevents modifications of the bulk material [8]. If $f_{th} < |f_{FCI}|$ the thermal lensing is stronger than the diffraction due to FCI, so the beam self-focuses and collapses due to the non-linear Kerr effect and modifies the material [8]. This is the case when the pulse returns from the back surface of the chip due to Fresnel reflection, and counter-propagates relative to the incident beam (see Figure 1.10). When additional pulses are sent, their focal points iteratively shift along the optical axis as each pulse further modifies the material, changing the optical path of the next pulse. In this way, the Si chip has only internal refractive index modification [8]. The elongation of the created structures inside the Si bulk is a self-limiting process, so the elongation cannot reach the sample surface, which can be demonstrated considering the exposure to n-pulses. The second pulse focal position l_2 is described by:

$$\frac{1}{l_2} = \frac{1}{f_{FCI}} + \frac{1}{f_{th}} + \frac{1}{l_1}, \tag{1.26}$$

where l_1 is the focal position of the first pulse, while the focal position of the n-pulse is:

$$\frac{1}{l_n} = (n-1)\left(\frac{1}{f_{FCI}} + \frac{1}{f_{th}}\right) + \frac{1}{l_1}. \tag{1.27}$$

Therefore, the total length of the modified region is:

$$L_{tot} = l_1 - l_n = \frac{l_1}{1 + \frac{\xi}{n-1}}, \qquad \text{with } \xi = \frac{f_{FCI} f_{th}}{l_1(f_{FCI} + f_{th})}. \tag{1.28}$$

1.2.3 Challenges of direct laser-writing inside silicon

This Section presents a brief overview of the peculiar properties of c-Si to understand why silicon presents several challenges regarding its functionalization by

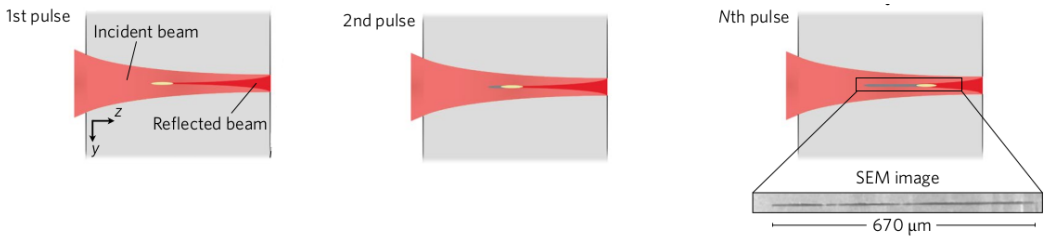

Figure 1.10: Schematic description of the modification of the local Si crystal structure. Consecutive laser pulses focus to shifted positions, axially elongating the structured region. Inset: scanning electron microscopy (SEM) image of a rod-like structure in Si. Adapted from [8].

IR lasers. These challenges are not present for other materials, such as dielectrics, for which laser-writing techniques are already well established and advanced. In this regard, silica (SiO_2) is an optimal candidate [9].
Table 1.1 reports these properties measured at room temperature and for a wavelength that belongs to the near-infrared (NIR) range. Each property has a crucial effect on the applicability of laser-writing techniques, as also reported in the comments of Table 1.1. Firstly, the high refractive index of c-Si implies that [9]:

1. high-precision stages and a vibration-free environment are required during the processing of silicon wafers because any movements along the optical axis of the sample or focusing lens is amplified by a factor of 3.5;

2. strong spherical aberrations need to be compensated;

3. the refracted angle is low ($\theta < 16.6°$ with NA$\sim$ 1), which implies that strong plasma effects, i.e. shielding, absorption, reflection and defocusing are present in the prefocal region.

Moreover, the non-linear response of silicon, which is strong in the near and mid-IR wavelength range, is anisotropic relative to the crystallographic directions, which introduces a further degree of difficulty in the laser-direct process.
Secondly, the laser beam parameters are strongly modified by the Fresnel reflection at the air-silicon interface, which reduces the beam energy reaching the focus, and by the strong dispersive character of silicon, which leads to an elongation of the pulse duration while the beam travels through the material. For instance, a 60 fs pulse is stretched to 100 fs after 1 mm [9].
In addition, the induction of modifications must rely on a balanced delivery of energy at the focal spot because a minimum energy threshold must be overcome, but even at high energy levels, the energy deposition is limited by plasma effects. The efficient delivery of the energy at the focal spot depends also on the strong

non-linear optical effects, e.g. self-focusing, prefocal multi-photon absorption and the fast thermal diffusivity.

The particular properties of c-Si lead to strict requirements regarding the combination of the employed laser parameters. Several studies and simulations have been carried out to assess the probability of inducing the modifications in the Si bulk and the effects on the modifications depending on the main laser parameters: pulse duration τ, wavelength λ, maximum delivered energy E_{max} and repetition rate. Table 1.2 and Table 1.3 present an overview of the state-of-the-art of laser-induced modifications in bulk silicon; the first table shows the attempts made with fs-lasers, while the second table the achievements made with ps- and ns-pulses.

The fs-range of pulse duration is far more unpredictable regarding the probability of inducing modifications in silicon. Indeed a wrong combination of the other laser parameters could lead to no modification, as shown by the negative results of [54, 55, 57–61, 63, 64]. Increasing the pulse duration the number of positive results increases and in the ps- and ns-range the pulse duration is highly effective for producing buried modifications. This evidence may be explained in terms of the response of silicon to longer pulses.
Firstly, the induced electron density increases with the pulse duration and so the delivered energy does. The shortest pulses (sub-100 fs) usually fail in inducing permanent changes inside Si [61] and *Chambonneau et al.* [9] observed that for a pulse duration of < 900 fs the corresponding delivered energy values are below the latent heat of fusion 3.4 kJcm^{-3}, which suggests the impossibility to modify the material.
Secondly, the non-linear propagation effects, as well as plasma screening or scattering effects, in silicon prevent the pulse energy to be efficiently localized and delivered near focus [61, 62] and for pulses of $\leq$ 50ps the plasma formation enhances the 2PA absorption in the prefocal region [45]. These non-linear effects are reduced by increasing the pulse duration [9, 41, 62]. For instance, the Kerr effect is significantly reduced with ns-pulses. Nevertheless, using too long pulses is not beneficial either because for pulses of $\geq$ 100ns the intensity is not high enough for producing sufficient electron density [45]. Lastly, avalanche ionization and bandgap closure are additional possible explanations for the observed modifications in the ps- and ns- range. Indeed the influence of avalanche ionization compared to MPA increases for longer pulse lengths and the longer pulse duration leads to an increase in lattice temperature and so to bandgap closure [41]. For instance, *Kämmer et al.* [41] calculated a reduced bandgap of 0.93 eV for a 10 ps pulse.
The previous considerations are liked to the peculiarity of silicon properties and response. Indeed for dielectrics machining, the energy threshold for modification of a bulk material normally decreases with pulse shortening because of the delivery

of progressively higher peak intensity and so more efficient non-linear absorption [61].

The range of wavelengths currently employed to laser-process silicon goes from 1.03 μm to 2.35 μm. Despite the achievement of modifications within this wide range, for 1.03-1.10 μm wavelengths the linear absorption coefficient is high (≥ 3.5 cm^{-1}) which means that the material transparency is limited [9]. The optimal wavelength for sub-surface modifications is calculated from the Non-linear Figure of Merit (NFOM) [6]:

$$NFOM = \sum_{K} \frac{n_2(\lambda)}{\lambda \beta^{(K)} I^{(K-1)}}, \tag{1.29}$$

which takes into account the K-photon absorption with I as the intensity of the laser beam. Equation 1.29 leads to find that $\lambda_{op} = 2.0 - 2.2$ μm [6].
This range was also experimentally tested by *Richter et al.* [6], who verified with pulses of 1965, 2090 and 2350 nm that the best results are obtained with 2090 nm laser. This could suggest moving to longer wavelengths, where 3PA and 4PA regimes are dominant [40], relative to the mostly employed 1550 nm lasers, which exploit the 2PA regime to induce modifications [9, 39]. Indeed around $\lambda = 2$ μm the non-linear refractive index has a peak and the Kerr effect dominates plasma defocusing. Around 2.8 μm the delivered energy reaches a minimum in the 3PA regime before growing again in the 4PA and 5PA regimes because at longer wavelengths the IBA is more efficient [9]. Again, going towards too long wavelength is not beneficial, since the critical plasma density and the electron density scale as $1/\lambda^2$, which implies that the plasma defocusing has a higher efficiency when λ increases. This has the consequence that the electron density induced in the bulk decreases with increasing wavelength [9].

The laser energy is another crucial parameter and is typically in the range of 0.5-20 μJ. However, silicon strong non-linear response to the incident radiation influences the delivered energy. Indeed, there is an energy dependence of the damage probability due to the competition between the Kerr effect and the plasma defocusing [67]. An interesting experimental result is that the focus position shifts upstream the laser for increased pulse energy [9].
In order to induce any modification, the energy threshold must be overcome and is typically found around 100 nJ [46, 61, 62, 66]. Two thresholds could be defined [62]: a "low damage threshold" (> 0.08 μJ) corresponding to the minimum incoming energy to deliver an energy density exceeding the modification of the material and a "high damage threshold", which is the energy that should not be exceeded to avoid non-linear delocalization inhibiting the pulse capability to inscribe damage in the material. For instance, *Wang et al.* calculated a "high damage threshold" at pulse energy > 0.3 μJ for 6 ps up to pulse energy of 1.95 μJ for 12 ps laser pulse [62]. Already with ps-pulses the reduced beam peak intensities (and so delocalization)

and the potential assistance of energy deposition by band gap closure, when pulse duration exceeds electron-phonon coupling time, gives a way to circumvent the clamping on the delivered energy density [62].

The last relevant parameter is the repetition rate. It is the number of pulses emitted per second and is typically above 0.1 kHz, but otherwise, it has a wide range. This parameter influences the morphology of the modifications because of the different accumulation of energy at the focus spot [52].

In conclusion of this review, it is worth mentioning the type of silicon wafers employed to obtain the results in Tables 1.2 and 1.3. The wafers are monocrystalline Cz wafers, both (100) and (111) oriented with nominal thickness from 60 μm to 2 mm and resistivity from 0.5 Ωcm to 200 Ωcm. The wafers could be p-doped (typically with boron), n-doped (typically with phosphorus) or intrinsic.

Table 1.1: Main properties of c-Si at room temperature. The optical properties are given for a 1.3 μm wavelength. The "low/high" comparison is made relative to amorphous silica. Adapted from [9].

Properties	Value	Comments
Band gap	1.1 eV	· Spectral domain of transparency between Mid-UV and Mid-IR is 1.1 - 7 μm
Linear refractive index n	3.50	· High: the actual energy reaching the focus is significantly reduced
Non-linear refractive index n_2	$\approx 3.1 \times 10^{-14}\text{cm}^2\text{W}^{-1}$	· Strong non-linearity of the beam propagation
Fresnel reflection coefficient for air–material interface	30.9%	· High
Group velocity dispersion	$\approx 1500\ \text{fs}^2\text{mm}^{-1}$	· c-Si is a highly dispersive medium, thus pulses are significantly stretched after few millimeters of propagation
Critical power for self-focusing	24 kW	· Low: the propagation is non-linear even at modest pulse energies (for 100-fs pulses self-focusing takes place at nJ level); impossible to induce modifications with pulse energies of a few nJ.
Critical plasma density n_c	$\approx 10^{20}\text{cm}^{-3}$	· For fs pulses the induced plasma density is subcritical even for a high input energy ($\sim 10\ \mu$J) and this prevents an enhanced energy deposition.
Multi-photon ionization order	2	· Low: a high absorption and depletion of pulse energy in the prefocal region prevents an efficient energy delivery to the focus spot.
Phase transition temperature (melting point)	1687 K	· Low: heat-accumulation is easily induced
Thermal diffusivity	$8.8 \times 10^{-5}\text{m}^2\text{s}^{-1}$	· High: laser-produced heat rapidly diffuses away from the focus; heat-accumulation at the focus is difficult and repetition rates > 10MHz are required for provoking that.

Table 1.2: Overview of the attempts to induce modifications of bulk silicon with different laser parameters: pulse duration τ, wavelength λ, maximum delivered energy E_{max} and repetition rate. The achievement of the bulk modification is reported alongside important observations (typically refractive index change Δn) and the measured energy threshold E_{th}. The pulse duration is the the range of fs.

τ (fs)	λ (nm)	E_{max} (μJ)	Rep. rate (kHz)	Modification	Observations	E_{th} (μJ)	Ref.
60	1300	10	0.1	no			[54, 55]
60	1300	20	0-100	yes	· Negative Δn	< 0.02	[54]
70	2400	1.7	1	near-surface	· Positive Δn		[56]
100	1300-2200	1	1	no		< 50	[57, 58]
100	1300	12	1	no			[59]
110	1240	600	1	no			[60]
110	1240	55	1	yes		> 10	[60]
170	1550	1.95	1	no			[61]
190	1550	1.28	1	yes		> 0.1	[62]
200	1240	5	0.01	no			[63]
250	1200	90	1	no			[64]
350	1550	2	250	yes	· Positive Δn	2	[65]
750	1950	2.55	0.1	yes	· Microbubbles along the optical axis z (size: ~ 4 μm) - positive Δn	1.5	[9]
800	1550	50	100	yes		< 50	[35]
800	1550	6.7	200	yes	· Elongated modifications	6	[41]
800	1550	10	400	yes	· Positive Δn	≈ 0.07	[66]

Table 1.3: Overview of the most remarkable successful induced modifications in bulk silicon with different laser parameters: pulse duration τ, wavelength λ, maximum delivered energy E_{max} and repetition rate. The measured energy threshold E_{th} is also reported. The pulse duration is the the range of ps and ns.

τ	λ (nm)	E_{max} (μJ)	Rep. rate (kHz)	Observations	E_{th} (μJ)	Ref.
1.7 ps	2350	0.020	3.8×10^3	· Small modifications		[6]
2 ps	1970	0.7	100	· Energy dependence of the damage probability	0.25	[67]
2 ps	1965	0.980	7.6×10^3	· Small modifications		[6]
5 ps	2090	760	10	· Conical elongated shape with the sharp corner pointing out the focal point		[6]
$>$ 5.4ps	1550	1.95	1		$\approx$ 0.08	[61]
0.5 ns	1064	2.2-8.8	0.1	· Optical diffraction gratings - polycrystallization/strain and voids		[49]
2 ns	1061	0.91	-		0.14	[46]
3.5 ns	1550	0.5-3.75	20-150	· Shape depends on energy, scanning speed, repetition rate, and input beam shape		[48]
3.5 ns	1550	20	20	· Waveguide - amorphous/polycrystalline features		[68]
3.5 ns	1550	0.5-3.75	20	· No doping dependence for initial carrier density of $10^{13} - 10^{16}$cm^{-3}; when $> 10^{18}$cm^{-3} smaller modified area		[53]
3.5 ns	1549	4	-	· Voids (100–500 n) and presence of Si- III /Si-XII phase	0.4	[46]
3.5 ns	1549	20	0.1	· Voids	0.43	[45]
5 ns	1550	2-8	150	· Spot-like and rod-like structures (3D writing) with negative Δn		[8]
5 ns	1550	5.3	1	· diffraction gratings with positive Δn		[52]
8 ns	1061	4	-	· Spot shape	0.2	[46]
460 ns	1061	4	-	· Formation of cracks	0.2	[46]

Chapter 2

Experimental Methods

2.1 Sample characteristics and preparation

Figure 2.1 shows all the samples analyzed within the present work and Table 2.1 reports the available specifications provided by the manufacturers. Table 2.2 reports the parameters of the laser-writing process. The main parameters are: duration, central wavelength, repetition rate and in-target energy of the laser pulses. The light coming from the laser system was focused with a high Numerical Aperture (NA) objective.

Table 2.1: Specifications of the silicon samples studied in this work provided by the manufacturers: growth method, Cz or Float Zone (FZ); crystal orientation; doping type and atom; resistivity ρ; sample dimensions. The P-doping refers to phosphorus.

Sample	Type	Doping	ρ (Ωcm)	Size
- 081	Cz (111)	N-type with P	7.60 ± 0.13	1.5×3.0
- 062	FZ (111)	-	> 8000	1.5×1.5
- 072 and 073	FZ (111)	-	> 8000	1.0×1.0
- polished wafer with surface lines	Cz (111)	N-type	n.a.	-

The "081" sample was obtained by the Laser Physics Group at NTNU [69]. They induced a layer of micron-sized defects at a depth approximately varying between 40 μm and 500 μm. Then, a thick layer of PMM was solidified on one surface of the sample. Slowly immersing the sample in liquid nitrogen, the detachment took place due to the fast cooling. The difference in the expansion coefficients of PMM and silicon led to the separation of the two thinner wafers. The separated wafer without PMM substrate has a thickness of (550 ± 10) μm. The other side

of the wafer, which remained attached to the substrate ("Si/substrate"), has a thickness of (433 ± 10) μm. Both are reported in Figure 2.1.

Table 2.2: Parameters of the laser-writing process, carried out with a Ho-fiber based amplifier from ATLA Lasers AS. The pulse parameters are the duration τ, the wavelength λ, the repetition rate f and the energy E [69].

Sample	τ	λ (μm)	f (kHz)	E
- 081, 062, 072, 073	ps	2.09	10	few μJ
- polished wafer with surface lines	ps	2.09	10	few μJ
- sample with buried modifications	ps	2.09	10	few μJ

The other samples are "062", "072" and "073" in Figure 2.1. They have been produced at the Faculdade de Ciências da Universidade de Lisboa, mainly by Professor João Manuel De Almeida Serra. The separation procedure is the same as previously reported by *Serra et al.* [7, 31, 33]. One side of the wafer is encapsulated with the "dam and fill epoxy" technique. Then, the sample is cured at 150°C for 30 minutes and then placed on an aluminium block at 10°C to cool down. Thus, the self-detachment takes place rapidly cooling the sample to room temperature. For clarity, the identifying names have been assigned to the pairs formed by the separated wafer and the substrate. In the rest of the discussion the term "Si/substrate" refers to the thin silicon foil that is attached to the stress-inducing layer, e.g. epoxy or polymer PMM. The term "separated wafer" indicates the wafer obtained after the whole separation procedure.

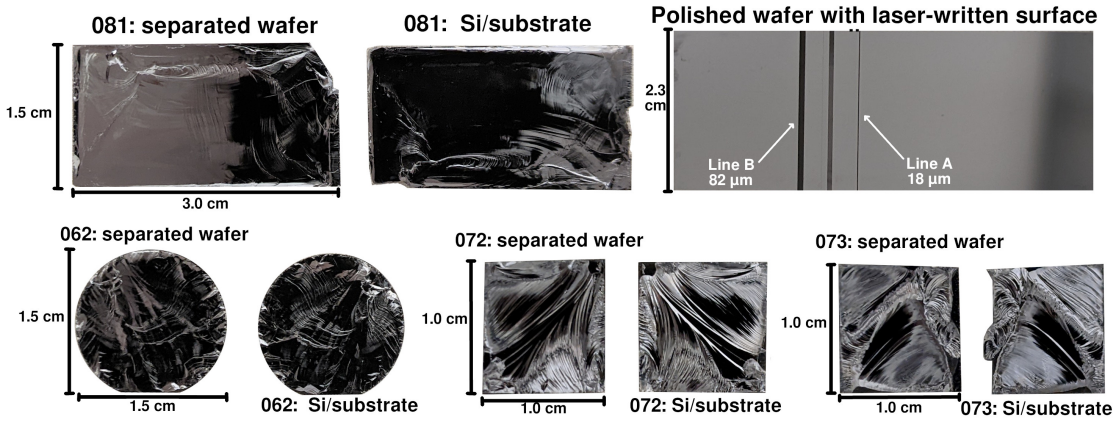

Figure 2.1: Samples under study with their identification name: 062, 072 and 073 are wafers produced by J. M. Serra at the Faculdade de Ciências da Universidade de Lisboa; 081 was obtained by the Laser Physics Group at NTNU. The c-Si polished wafer has laser-written lines of different widths (reported in the figure): only Lines A and B were considered in the experiments.

To study the properties of laser-induced modification in pristine wafers, two silicon wafers were only laser-processed. The purpose of these samples is to analyze the properties of the induced defects and they were not fabricated for SLIM-cutting.
The first one, not depicted in Figure 2.1, contains buried modifications. These defects should be buried 200-300 μm under the surface and only etching, cleaving or FIB milling expose the defects. The laser inscribing system had the parameters reported in Table 2.2. Keeping the energy fixed, a group of three laser-written lines of defects was inscribed at a specific depth. Then, two other groups were written increasing the energy by 33% and 66%, respectively, but keeping the same focusing depth. This procedure was repeated several times obtaining different sets of three groups. The focusing depth changed between sets to determine the optimal laser parameters for that specific depth. The scheme in Figure 2.2 depicts this procedure. These defects are not visible from the cross-section without polishing and etching the surface.
Due to the difficulty in seeing the buried defects, another sample was obtained from a thin polished commercial-grade silicon wafer (≈ 165 μm thickness). Figure 2.1 shows that four thick lines are visible on the surface. These visible structures are composed of a dense sequence of thin lines of defects (width ~ 1 μm) with a nominal distance of 1 μm between each other. The defects have been produced by a laser system with the parameters in Table 2.2. Only the lines labelled as "A" and "B" were considered for the experimental measurements.

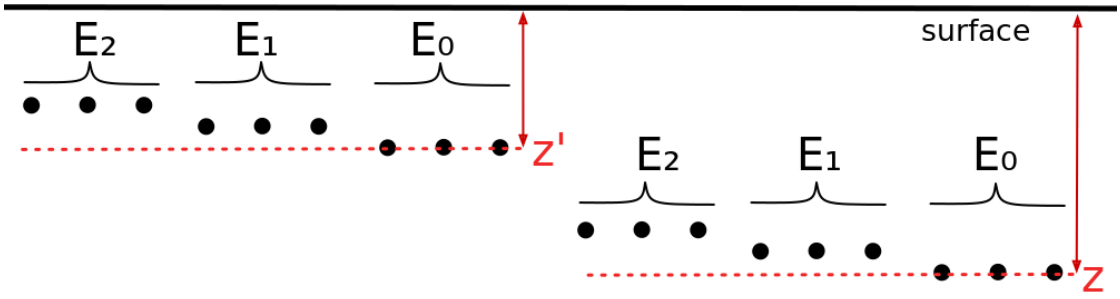

Figure 2.2: Laser inscribing procedure for the optimization of the laser parameters for a specific depth. The first set is inscribed at a depth z and the second set at the depth z'. Changing the energy from E_0 to $E_1 = 1.33E_0$ and $E_2 = 1.66E_0$ the effective depth of the defects changes.

2.2 Characterization methods

2.2.1 Lifetime measurements with microwave-PCD

Two main approaches are generally employed to measure the lifetime: steady-state and transient methods. They both depend on the way the excess carriers are generated in the silicon wafer. In the first case, i.e. steady-state photo-conductance (SSPC), the lifetime is given by the ratio between the measured excess carrier density and the carrier generation rate [14]. In the second case, i.e. photo-conductance decay (PCD), the lifetime is extracted by measuring the rate at which carriers recombine, terminating the generation abruptly. Therefore, the lifetime is extracted considering that the change of the carrier density with time depends on the generated excess carrier density Δn (m^{-3}) and the lifetime τ (s) [14]:

$$\frac{dn}{dt} = -\frac{\Delta n}{\tau}. \tag{2.1}$$

Both methods, SSPC and PCD, require to determine the excess carrier density and the best way to measure Δn is through the photo-conductance. Indeed, the change of the photo-generated excess carrier density Δn depends on the photo-conductance change $\Delta\sigma$ (S) and the sample thickness W (m) as follows [14, 70, 71]:

$$\Delta n(t) = \frac{\Delta\sigma(t)}{q(\mu_e + \mu_h)W}, \tag{2.2}$$

where q is the elementary charge and μ_e and μ_h are the mobility of electrons and holes, respectively. Typical mobility values in silicon are $\mu_e = 1100$ $\mathrm{cm^2V^{-1}s^{-1}}$ and $\mu_h = 400$ $\mathrm{cm^2V^{-1}s^{-1}}$ [14].

Once the excess carrier density is determined, SSPC and PCD determine the lifetime, respectively as [14]:

$$\tau_{SSPC} = \frac{\Delta n}{G}, \tag{2.3}$$

$$\tau_{PCD} = -\frac{\Delta n}{\frac{dn}{dt}}, \tag{2.4}$$

where G is the carries generation rate.

Microwave PCD (μ-PCD) is a non-destructive, pure transient technique [70, 71]. The measurements are parameter-free, non-contact, very fast and suitable for wafer mapping [72]. The method is based on the analysis of the conductivity after the injection of electron-hole pairs by a short laser pulse [73].

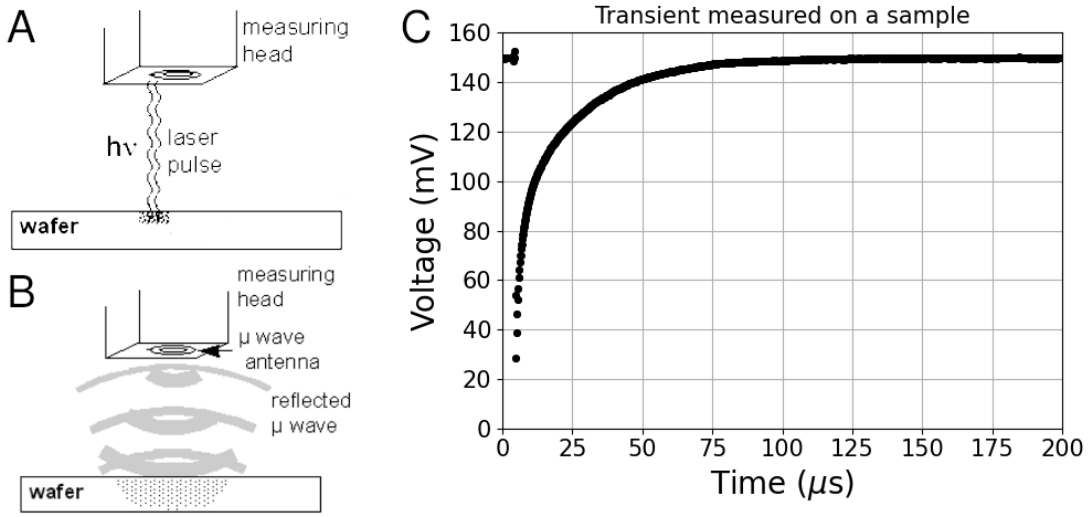

Figure 2.3: Microwave PCD working principle: **(a)** laser excitation and **(b)** detection of the microwave reflected power; adapted from [13]. **(c)** Example of an acquired transient: as the carriers return to equilibrium exponentially, the signal changes accordingly.

The IR laser pulse impinges on the sample perpendicular to its flat surfaces and the reflected microwaves are monitored by a microwave detector (see Figures 2.3a,b). Moving the sample underneath the open end of the waveguide, the sample properties may be mapped across the wafer.
For transient minority carrier lifetime measurements, the microwave detector records the change of the reflected power as a function of time [74]. Indeed, the laser pulse induces the generation of excess carriers in the sample and the carrier density, and thus also the conductivity (see Eq.2.2), both decay due to carrier recombination within the bulk and at the surfaces of the sample. The resulting transient of the

reflected microwave power is interpreted as the effective minority-carrier lifetime, by fitting the μ-PCD signal with an exponential function [72, 74]:

$$\Delta V \sim \exp(-t/\tau), \tag{2.5}$$

where τ is the carrier lifetime. Figure 2.3c shows an example of the transient measured on a sample.

Regarding the advantages of μ-PCD, the determination of the lifetime is quite robust, since it only relies on the measurement of the relative change of the carrier density with time [14]. Therefore, the generation rate does not need to be determined accurately as in SSPC, which implies the knowledge of the photon flux, the fraction of absorbed photons and the thickness of the wafer [14]. Moreover, under low-level injection, the differential lifetime directly coincides with the actual lifetime [71].
Nevertheless, both wafer-related factors (injection-dependent bulk and surface recombination, trapping of excess carriers, depletion region modulation) and measurements conditions related factors (non-linear microwave reflection, too small or non-uniform illumination spot compared to the microwave detection area, effects of lateral carrier spreading) can lead to deal with non-exponential, but rather linear, decay [72]. The strong impact of surface recombination requires the use of passivation techniques for obtaining meaningful data about the bulk recombination lifetime [73]. The injection level, i.e. the carrier concentration induced by illumination, is unknown and cannot be distinguished from the carrier concentration due to doping. In addition, the trapping effect leads to high apparent lifetimes even at low excess carrier concentrations. Since the trapped minority carriers lead to an extra charge in the majority carrier band, they will be misinterpreted as minority carriers [70]. The shape of the PCD signal acquired as a function of time will show a tail due to the slow de-trapping of minority carriers. To avoid the trapping effect in the PCD signal, the traps have to be saturated with carriers injected by a steady-state bias light of low intensity [71].

2.2.2 Raman spectroscopy

Raman spectroscopy is suitable for nondestructive, microscopic, chemical analysis, and imaging characterizations, observing vibrational, rotational, and other low-frequency modes.
Indeed, its basic principle lies in the inelastic scattering of the radiation that is re-emitted from the sample after its exposure to monochromatic electromagnetic radiation in the UV-Vis-IR range with high intensity. The portion of the inelastically scattered radiation is only 10^{-7} of the total scattered light, which is mainly elastically scattered. The need for a high-intensity source is due to the low intensity of Raman scattered photons. Absorption and reflection also take place.

Inelastic scattering processes are two-photon events that involve the simultaneous annihilation of an incident photon and the creation of a scattered photon [75]. The inelastically scattered radiation, which has a frequency lower than the incident radiation, is called Stokes lines and the one that has a higher frequency is called Anti-Stokes. Indeed, the wavenumber of Raman spectra is given by:

$$\omega_R(\mathrm{cm}^{-1}) = \omega_0 \pm \omega_S, \tag{2.6}$$

where ω_0 is the wavenumber of the incident radiation and ω_S is the wavenumber of the scattered radiation. The plus sign is for Anti-Stokes lines, which means that the incident photon gains energy, while the molecule loses energy.

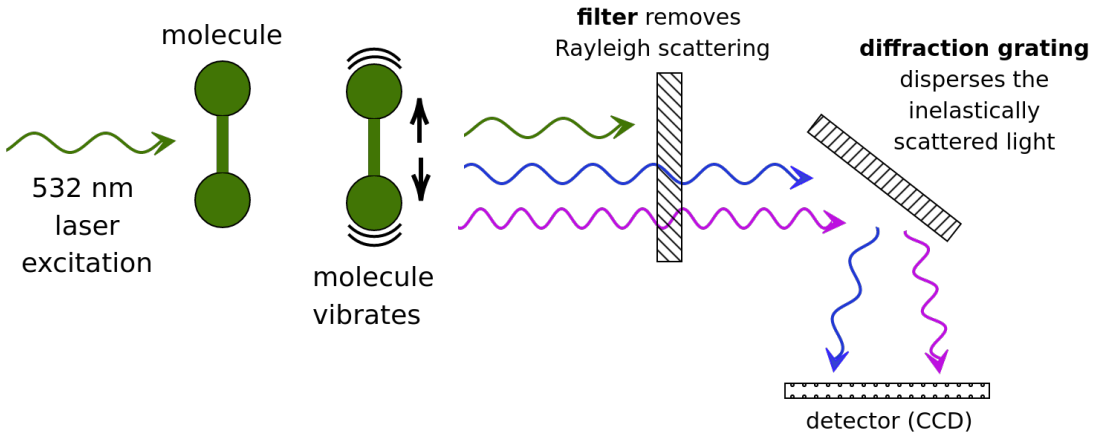

Figure 2.4: Scheme of the working principle of Raman spectroscopy.

The reason is that an excitation from the first vibrational state to the second virtual state takes place. Then, there is a deexcitation from this level to the ground vibrational state. Thus, the energy of the emitted photon is higher than the first transition. On the other hand, the minus sign is for Stokes lines, which correspond to a reduction of the incident photon energy, while the excited molecules absorb energy. In this case, after the excitation from the ground state to the first virtual state, the deexcitation takes place from this level to the first vibrational state. Thus, the energy of the emitted photon is lower.
The energy difference depends on the mass of the nuclei and the strength of the bond between the atoms involved in the vibrational motion [76]. Indeed, the Raman spectra are generated from the vibrational motions that resulted from the change in a source-induced molecular dipole moment [77]. The effect may be understood as that from an induced polarization P (the dipole moment per unit volume) that oscillates at the frequency ω_S [75].

The micro-Raman spectrometer consists of a laser source that is focused into the sample with a micrometre spatial resolution. The scattered radiation typically goes through a dispersion device and a suitable grating which separates the scattered beam into its components. Figure 2.4 shows this working principle. The instrument provides very detailed energetic and spatially localized information, while recording the energy change as a spectrum of the scattered intensity *vs* Raman shift $\omega_{\mathrm{R}}(\mathrm{cm}^{-1})$.

Some applications of Raman spectroscopy are the determination of crystalline orientations, the measurement of temperature and stress, the characterization of doping levels, and the study of alloy semiconductors [78]. Indeed, the study of the intensity of the Raman scattering as the sample or the light polarization is rotated determines the crystalline orientations. The application of stress alters the phonon structure because the strain associated with the applied stress changes the equilibrium position of the atoms in the crystal. Similarly, the presence of an amorphous phase is detected because the Raman spectrum from an amorphous material generally consists of a few broad bands, with maxima at roughly the frequencies corresponding to peaks in the broadened phonon DOS for the crystalline phase [75]. Moreover, the presence of impurities produces new Raman peaks in the spectrum, due to the vibrational modes associated with motions of the impurity atoms, and changes the spectrum of the host material through the change in mass and bond length (atomic effects) and, in the case of donors and acceptors, through the interaction of the carriers with the lattice (electronic effects) [78].

2.2.3 Atomic Force Microscopy

The Atomic Force Microscopy (AFM) technique is a form of Scanning Probe Microscopy (SPM) which provides a 3D profile on a nanoscale, by measuring forces between a sharp probe (radius less than 10 nm) and surface at a very short distance (0.2-10 nm probe-sample separation), as shown in Figure 2.5a. The tip is mounted at the end of a flexible cantilever, which deflects linearly with the force applied. The typical force-distance curves are reported in Figure 2.5b.
The AFM setup (Figure 2.5c) includes an optical system consisting of a laser beam focused on the top surface of the cantilever. The reflection hits a photodiode and the variation of the signal position on the photodiode is associated with the tip/sample force interaction. The sample is mounted on a stage that can move in three directions ($x-y$ to scan the sample surface and z to obtain 3D images) through piezoelectric actuators, which deform by applying an electric field. The effect enables scanning with picometre precision. The AFM also requires a mechanical anti-vibration system that isolates it from external perturbations.

AFM has three main operation modes: contact, "tapping" (TM-AFM) and non-contact modes. In contact AFM the probe-surface separation is less than 0.5

nm and repulsive forces are dominant. The forces between the probe and the sample remain constant by maintaining a constant tip-sample distance, thus also the cantilever deflection is constant. In this case, the feedback loop is activated. Plotting the z-direction position (height), adjusted by the piezoelectric element, provides the sample topography. The vertical resolution is higher but, the lateral frictions with the surface of the sample are much larger, leading to undesired tip and/or sample wearing [79].
In non-contact AFM the probe-surface separation ranges from 0.1 to 10 nm and attractive forces dominate (electrostatic, magnetic, and Van der Waals) [79, 80].
In TM-AFM the cantilever makes intermittent contact with the surface working at its resonant frequency. Thus, the interactions between the tip and the sample are detected through the changes in amplitude, frequency and energy compensation of this oscillator. In amplitude modulation mode, the feedback loop adjusts the piezoelectric element in the $z-$direction to make the cantilever oscillate at the resonant frequency and constant amplitude (Figure 2.5d). Because the contact time is a small fraction of its oscillation period, the lateral forces are reduced dramatically [80], which translates into a lower risk of tip/sample wearing.

Conductive Atomic Force Microscopy (C-AFM) is a type of contact AFM that is used to characterize simultaneously the surface topography and conductivity. A voltage source is needed to apply a potential difference between the tip and the sample holder, and a preamplifier is used to convert the (analogical) current signal into (digital) voltages that can be read by the computer [79]. The nanoprobe has to be conductive. The C-AFM setup is shown in Figure 2.5e.
Typical current values are in the range of sub-nA to μA [82]. The smallest currents detected by a C-AFM are defined by its electrical noise, which is (in the best cases) hundreds of femtoamperes [79].

Tip/semiconductor interaction The C-AFM tips are typically made of silicon covered in a metal layer (e.g. Pt or Ir). When the metallic tip is placed on a semiconductor sample, a depletion barrier forms in the semiconductor if the work function of the metal is larger than the electron affinity [82]. This is the case for Si/Pt-Ir tips on a silicon sample. This depletion barrier behaves similarly to a diode. When a forward voltage is applied, an ohmic contact is formed, and the current increases exponentially with the voltage. The expression for this regime is:

$$I = I_0 \exp\left[\left(\frac{qV_f}{\eta k_B T}\right) - 1\right], \tag{2.7}$$

where I_0 is the saturation current, q is the electron charge, V_f the forward bias, T is the temperature, η the ideality factor (near unity for $T \geq 300$ K, $N \leq 10^{17}$

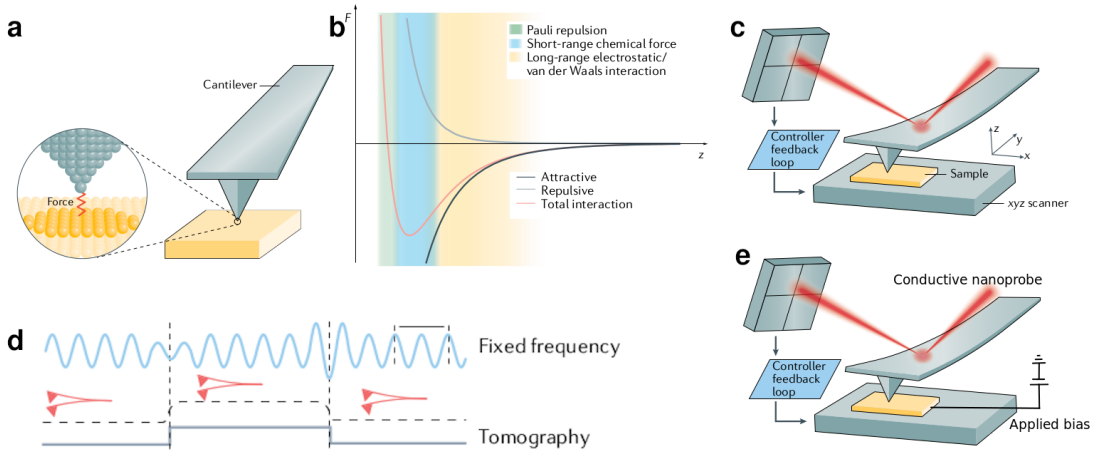

Figure 2.5: Working principle of Atomic Force Microscopy. **(a)** AFM detects local forces and corresponding mechanical parameters through a spring-like cantilever. **(b)** Schematic showing typical force–distance curves. Both short-range (green region, Pauli repulsion; blue region, short-range chemical force) and long-range (orange region, long-range electrostatic or van der Waals interaction) components are indicated. Black and grey curves represent the attractive force and repulsive force versus tip distance, respectively. **(c)** Schematic AFM setup: the laser beam detects cantilever deflection caused by interaction forces between the tip and the sample. Tiny changes in cantilever deflections are compensated by feedback loops controlling the piezoelectric scanner. **(d)** Working principles of amplitude modulation AFM. **(e)** Schematic conductive AFM (C-AFM) setup: a constant bias is applied to the sample holder. Adapted from [81].

cm^{-3}). The saturation current is given by:

$$I_0 = AA^*T^2 \exp\left[-\frac{q}{\eta k_B T}\left(\phi_B - \sqrt{\frac{qE_m}{4\pi\epsilon_s}}\right)\right] \tag{2.8}$$

$$E_m = \sqrt{\frac{2qN}{\epsilon_s}\left(V_r + Vbi - \frac{k_B T}{q}\right)}, \tag{2.9}$$

where A and A^* are the effective emission area and the effective Richardson constant, respectively; ϕ_B is the barrier height, E_m the electrical field maximum, V_r the reverse bias, V_{bi} the built-in voltage and ϵ_s the permittivity of the semiconductor.
On the contrary, with reverse bias, the current is dominated by Schottky emission (Eq.2.8) and remains comparatively small. The Schottky emission follows the formula of the thermionic emission, because the depletion layer in reverse direction performs as an insulator.

2.2.4 Experimental set-up and sample preparation

Microwave-PCD

The samples were firstly cleaned with acetone and rinsed with 70% ethanol. The lifetime was measured employing Semilab's WT-2000, equipped with an InGaAs laser diode emitting at 904 nm wavelength, 200 ns pulse width and 12 TW power. The frequency of the microwave antenna was 10.296 GHz. The lifetime values were calculated by averaging 16 transients for each spatial position. The signal was acquired by Semilab's WINTAU32 v.9.51.341 software. The penetration depth in silicon amounts to ≈ 30 μm [11, 13]. All the measurements were carried out with a spatial resolution of 250 μm. The samples were measured only without passivation. Therefore, the effective lifetime is expected to be underestimated because of the strong contribution of surface recombination.

SEM

In this project, two SEM instruments were employed. Images of buried modification exposed on the cross-section were taken with FEI Apreo at Nanolab NTNU. These SEM images were taken at a working distance of $\sim$ 2 mm, a tilt of 0°, a beam current of 0.40 nA and an acceleration voltage of 10 kV. Images of surface laser-written lines were taken with the SEM of the FEI Helios NanoLab DualBeam FIB at Nanolab NTNU. These SEM images were taken at a working distance of $\sim$ 4 mm, a tilt of 52°, a beam current of 0.17 nA and an acceleration voltage of 10 kV.
The cross-section of the sample was firstly polished and then etched to expose the defects.
Before inserting the samples in the SEM chamber, they were cleaned with Diener Electronics' Femto Plasma Cleaner for three minutes at the maximum generator frequency of 40kHz and with oxygen at 200 sscm flow rate.

Micro-Raman spectroscopy

Micro-Raman spectroscopy was carried out employing Renishaw's inVia Reflex Raman microscope at Nanolab NTNU and the signal was acquired with Renishaw's WiRE 4.0 software. This instrument acquires Raman shifts from 5 cm^{-1} to 30000 cm^{-1} with a spectral resolution of 0.3 cm^{-1} (FWHM), while the lateral and axial resolutions are 0.25 μm and < 1 μm, respectively [83]. The 532 nm laser was mounted in the spectrometer. Its maximum power is 100 mW and it is paired with a 2400 l/mm grating. The power (% of the maximum power), the exposure time and the accumulation were optimized for each measurement. The employed magnification lenses were Leica's N PLAN EPI 100x/0.85 and N PLAN EPI 50x/0.75.

The laser beam has a nominal divergence ($1/e^2$) of < 1.2 mrad and a diameter at the aperture of 700 μm. The beam diameter in the focal plane is 2 μm and 4 μm for the 100x and 50x lenses, respectively.
Before performing the measurements, the samples were cleaned with acetone and rinsed with 70% ethanol and then, with Diener Electronics' Femto Plasma Cleaner for two minutes at the maximum generator frequency of 40 kHz and with oxygen at 180 sscm flow rate.
After the acquisition of the signal, the intensity was normalized to the maximum value of each set of data because the relative intensity of the signals to each other is not considered relevant. This holds for every Raman spectrum presented in this thesis.

AFM and C-AFM

The NT-MDT SMENA SOLVER AFM, placed on an active vibration isolation table, was employed. All the experiments were carried out in air. The resolution was 512×512 pixels per image. Several series of scans decreasing in size from 70×70 μm^2 to 5×5 μm^2 were taken on each sample. Data elaboration was carried out by using the software Gwyddion. The detection limit in height was determined by the vertical sensitivity of the piezoelectric tube, which is 0.1 nm. The specifications of the employed tips are summarized in Table 2.3 and the label is used to identify them in Section 3.2.3. For C-AFM, the sample was fixed onto a glass slide with bi-adhesive tape and the electrical contact was made with silver paste. Different voltages were employed. The I-V curves were acquired for applied voltages from -2V to +2V with a grid of 10×10 points. For each spot, the tip took 10 s to perform the sweep.

Table 2.3: Specifications of the tips employed for AFM with spring constant k and tip curvature radius r.

Tip	coating	k (N/m)	r (nm)	use	label
NT-MDT NSG10	Au	12	10	TM	I
NANOSENSORS PPP-CONTPt	PtIr	0.20	25	C	II
NANOSENSORS CDT-CONTR	diamond	0.5	10	C	III
NT-MDT CSG11	PtIr	0.11	10	C	IV
MikroMasch XNC12	Si_3N_4	0.08-0.32	30	contact	V

Chapter 3

Results

3.1 Characterization of bulk modifications

3.1.1 SEM surface characterization

The SEM imaging technique was employed to determine the position and the morphology of the defects in the unseparated sample, where the modifications are buried under the surface.

The first sample that was analyzed presented a series of inscribed lines, which appear as elongated defects if the cross section is etched, as shown in Figures 3.1-3.2a-3.3. These modifications constitute groups of three defects each, which are (9.83 ± 0.12) μm apart from each other. Note that the pulse energy increased by 33% for each group within the same set and the same set was inscribed with a constant focusing depth, as Figure 2.2 describes.

The defect morphology is not uniform: some defects have a straight elongated structure, while others slightly bend, appear bigger on the shallower end, or even have a circular shape, as Figure 3.1 shows. It is a challenge to determine whether the laser process or the etching process is responsible for this inhomogeneity because the defects are not visible without etching the surface.

When the shape is almost a regular elliptical shape, as in Figure 3.2c, the calculated average dimension in the laser direction is (2.00 ± 0.09) μm, while the dimension perpendicular to the laser beam is (486 ± 4) nm. Both values were calculated as the average of the dimensions of group 2 in Figure 3.2b,c.

The modifications' size does not change significantly with the increasing laser pulse energy, i.e. between different groups. The elongated structures should significantly increase their sizes when the pulse energy is increased by 50%, in the range of the μJ [48, 53].

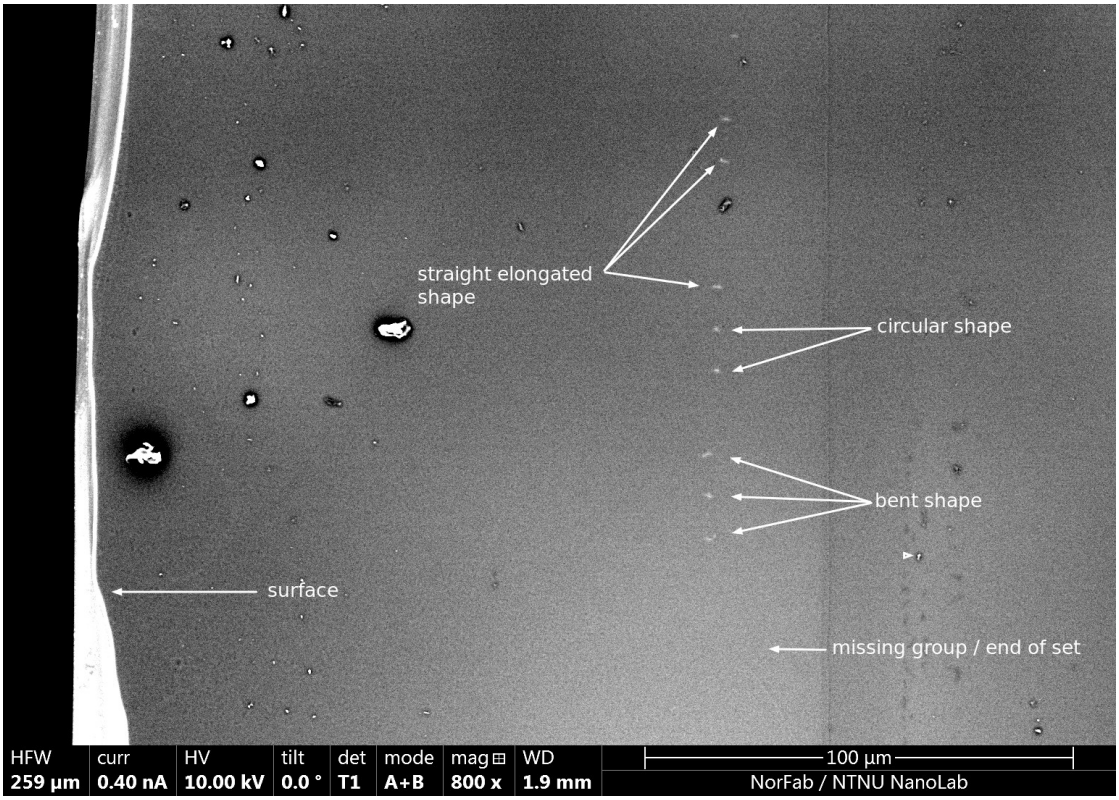

Figure 3.1: BSE signal of buried modifications taken with FEI Apreo SEM. The first visible group (top) has a depth of 148.7 μm, calculated from the surface to the right end of the modification. The different modifications' morphology with a bent, straight or circular shape is evident. The last visible group could be the end of the set or an intermediate set that is followed by a missing group.

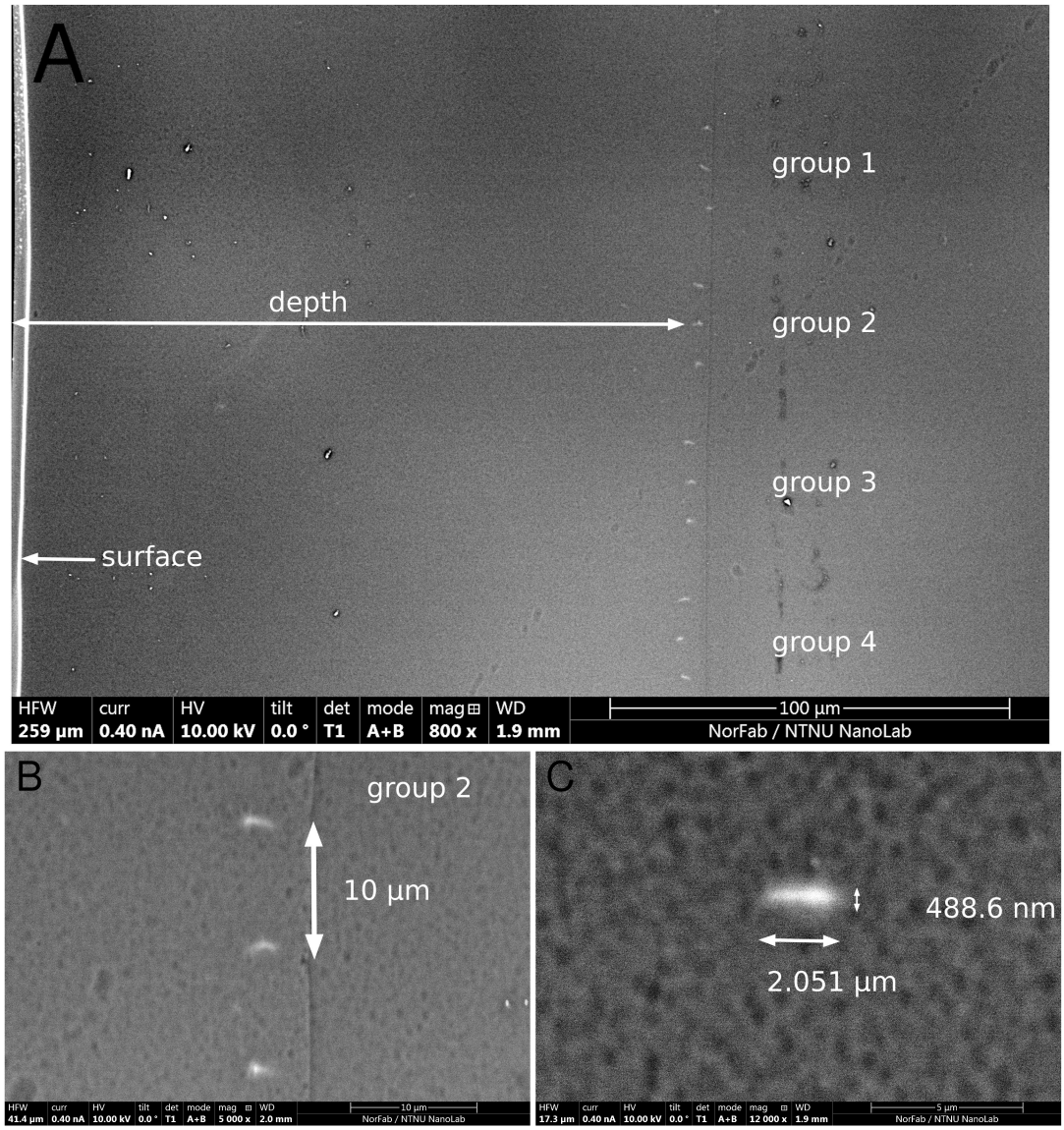

Figure 3.2: BSE signal of buried modifications taken with FEI Apreo SEM: **(a)** overview of four groups of defects, the depth was calculated from the surface to the right end of the modification; **(b)** three defects composing a group with a distance of ≈ 10 μm from each other (scale-bar of 10 μm); **(c)** morphology of a single defect, where the dimension along the laser beam is 2.051 μm and the other dimension is 488.6 nm (scale-bar of 5 μm).

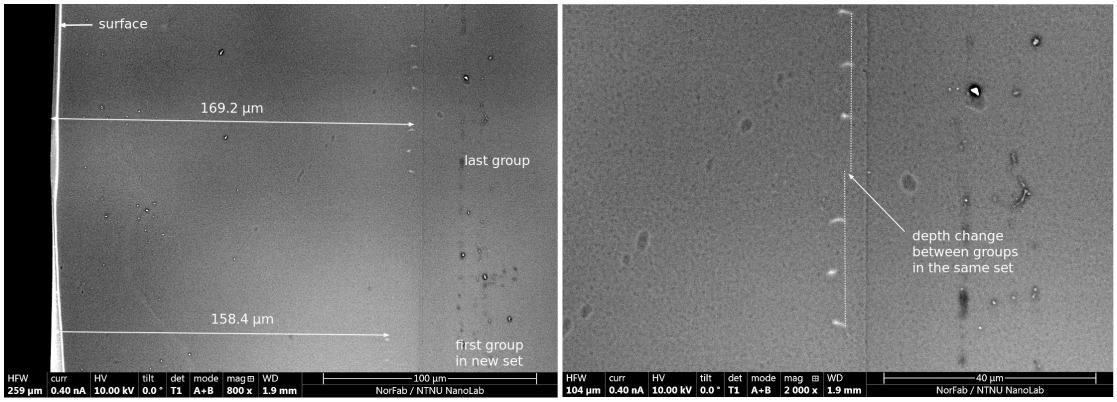

Figure 3.3: BSE signal of buried modifications in a different sample region, taken with FEI Apreo SEM. The first visible group has a depth of 170.6 μm, the second one is at 169.2 μm and the third one is at 158.4 μm (left image). The depth change between the two upper groups belonging to the same set is 1.429 μm (right image). After the second group of defects, a gap appears: considering the depth difference of ≈ 11 μm between the second and third group, the two groups belong to different sets. The scale-bars are 100 μm and 40 μm, respectively.

Another aim of the SEM analysis was to determine the depth of the inscribed lines. The interesting result is that the depth changes as a function of the pulse energy. Indeed, recalling the laser-writing procedure for this sample, the only parameter that was changed between groups was the pulse energy, while the focusing depth was kept fixed (see Figure 2.2). This effective depth difference is visible in Figure 3.2a, where the first group is clearly at the deepest position, while the fourth is the shallowest. Figures 3.3 and 3.1 present the same but for more groups in other sample regions.
The average depth change was calculated considering four sets of four or five groups each. For instance, Figure 3.2a shows only one set. If the depth change between the two groups was more than 9 μm, which is approximately how much the focusing depth was deliberately changed between the sets, the two groups were considered as belonging to different sets. This constraint was taken into account to make sure that the set was only composed of groups with the same focusing depth and only variable pulse energy. Nevertheless, some gaps between groups are detected which may represent either the desired gap between two sets or a gap created by the unsuccessful induction of any modification. For instance, the gap in Figure 3.3 should be the gap between two different sets because the depth change between the two groups is ≈ 11 μm.
The average depth change between the central defects of two adjacent groups in one set results (-1.71 ± 0.14) μm, which is related to an increase in energy of 33%. Therefore, the depth of the modifications decreases with increasing energy. Within

the same group, the three defects induced with the same pulse energy have the same depth. Not all groups of defects were inscribed because they clearly miss in the sequence of defects, which suggests that the laser parameters were not optimal to induce any modification at that specific depth. Unfortunately in some cases it is difficult to determine if one group is missing. Figure 3.1 is an example because after the last visible group no other defects are detected.

3.1.2 Micro-Raman spectroscopy

To determine the nature of the laser-induced modifications, the Raman spectroscopy technique was employed. Figure 3.4 shows the results of the analysis in a sample region (see Figures 3.4a,b). The acquired Raman spectra clearly show that there is not any difference between the reference spectrum and the spectrum of the modification. In both cases, the typical crystalline silicon peak is detected at (520.700 ± 0.014) cm^{-1} for the reference and at (520.708 ± 0.014) cm^{-1} for the modification. Thus, the two peaks are not shifted relative to the expected position of the monocrystalline silicon TO-peak [25, 68, 84]. The TO-peak arises from the first-order Raman scattering of the longitudinal optical (LO) and the transverse optical (TO) phonon modes which are degenerated at the Γ-point [47], but for backscattering from the (111) silicon surface and in the present instrumental configuration, the contribution of the TO-phonon mode is expected to be dominant [78].
The FWHM of these peaks is also comparable because it results in (4.70 ± 0.03) cm^{-1} for both. Therefore it seems that there is no broadening of the TO-peak of the modified material relative to an unmodified region.
Moreover, both spectra display the typical c-Si broad region between 930 and 1040 cm^{-1} [84]. The second-order optical-phonon peaks (2TO) correspond to this region [47].
However, with the employed instrument the beam size at the focal plane (≈ 4 μm) is bigger than the dimension of the defects. Therefore the contribution of the modified material to the overall signal is not enough to clearly identify the nature of the induced modification.

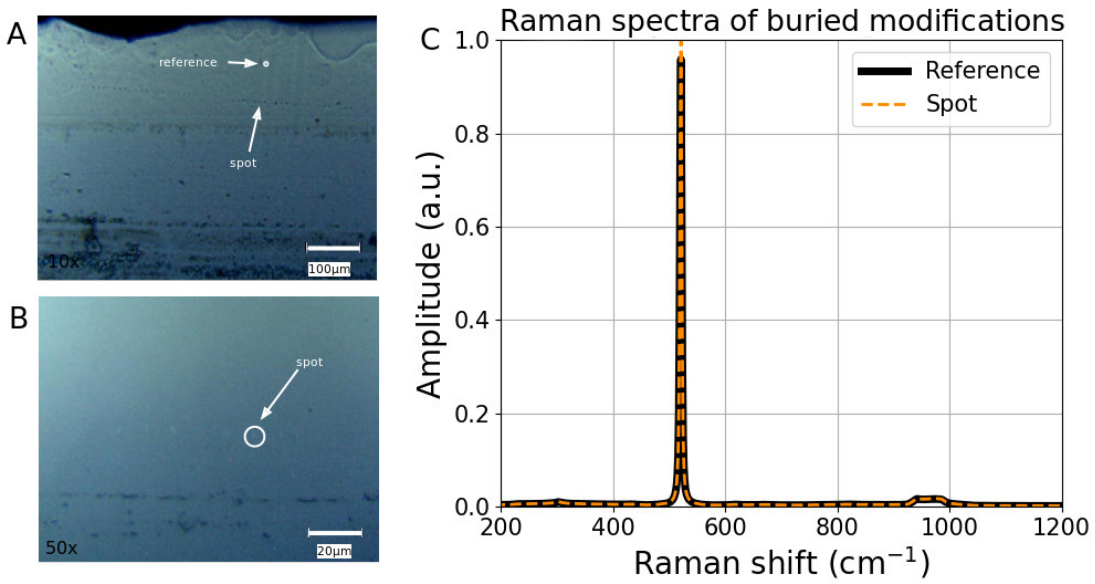

Figure 3.4: Raman spectroscopy of the laser-induced buried modifications. **(a-b)** OM images of one sample region at 10x and 50x magnification, respectively; the reference and the modification spots for the Raman analysis are indicated. **(c)** Raman spectra of the reference and defect spots acquired with the 532 nm laser with 50x magnification, 2s exposure and laser power of 5 mW.

Aiming to check the previous results, another sample was analyzed by Raman spectroscopy. Refer to "polished wafer with laser-written lines" in Figure 2.1. In this case, the laser writing process was done on the surface of a polished silicon wafer, being sure that the defect density was high enough to overcome the beam size problem. Figure 3.5a shows two black lines, where the Raman spectra were acquired. What appears as a line in the OM images is composed of several lines of defects at a distance of $\approx$ 700 nm, as shown in Figures 3.5e-g. The difference between the two wider lines only relies on their width.
Considering this analysis, the laser-writing process effectively changes the silicon properties. Indeed, the results in Figure 3.5b qualitatively show that the characteristic TO-peak at 520 cm^{-1} belongs to all three spectra, but a tail towards lower wavenumbers appears for the modified material. The behaviour is also highlighted by the inset in Figure 3.5c. Here a strong feature is detected around $\approx$ 496 cm^{-1}.

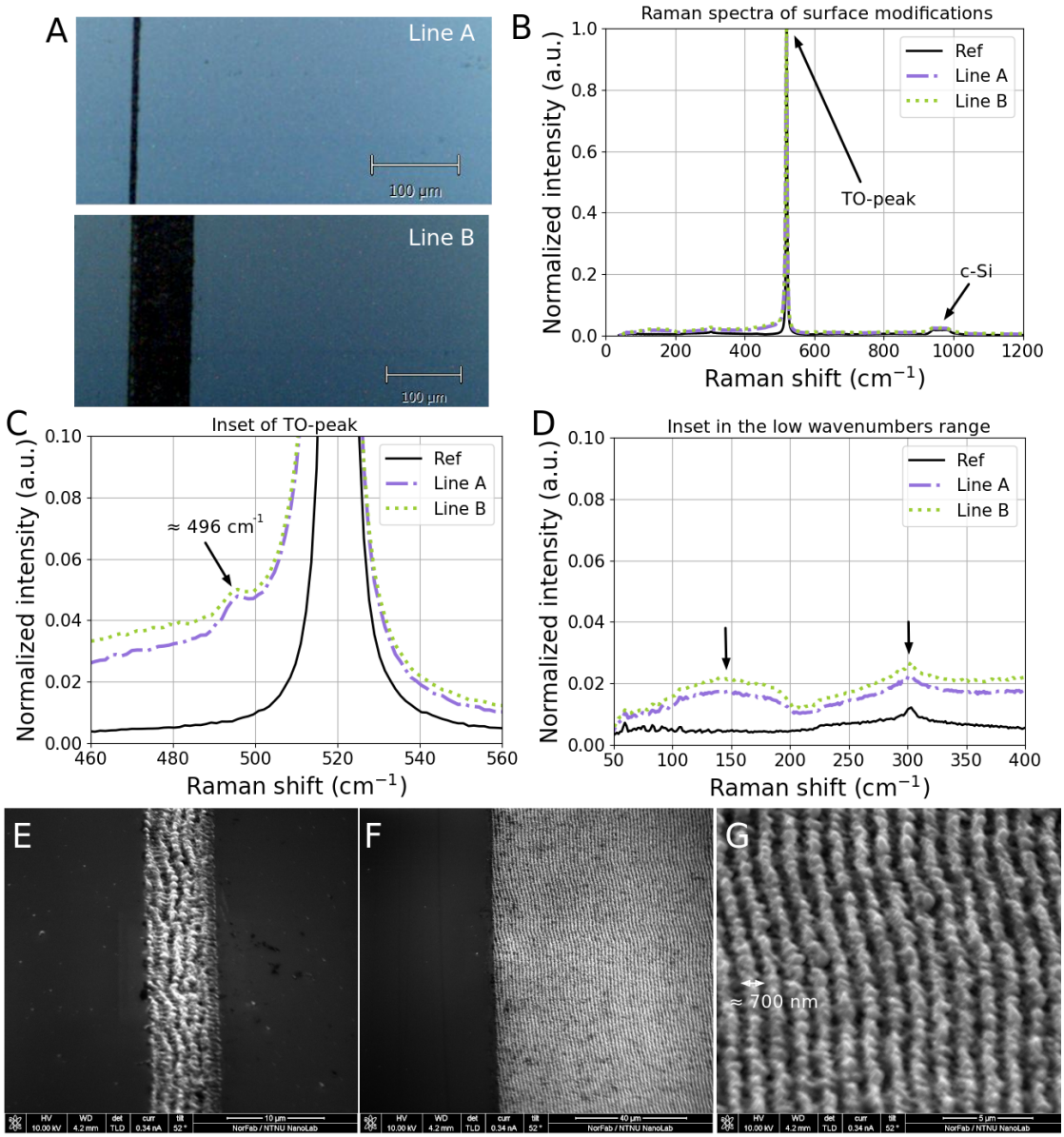

Figure 3.5: Study of the laser-induced surface modifications written on a polished silicon wafer ("polished wafer with laser-written lines" in Figure 2.1): **(a)** OM images at 10x magnification of the two surface lines; the scale-bar is 100 μm. **(b)** Raman spectra of two spots taken inside the two lines and of a reference point taken on the unmodified silicon surface; the spectra were acquired with the 532 nm laser, 100x magnification, 2s exposure and 5 mW power. **(c)** Inset of the spectra centred on the crystalline silicon peak at 520 cm^{-1}. **(d)** Inset of the low wavenumbers range from 50 cm^{-1} to 400 cm^{-1}. Secondary electrons images of Line A **(e)** and Line B **(f,g)** were acquired with FEI Helios NanoLab DualBeam FIB; the scale-bars are 10 μm (e), 40 μm (f), 5 μm (g).

Regarding the modified material, the position of the TO-peak is shifted towards lower wavenumbers (see Tab.3.1) and the peak is $\approx 25\%$ broader. Indeed, the FWHM increases by $\approx +1$ cm^{-1}. The spectra of the modified silicon in lines A and B show a shift of the TO-peak of 0.7 and 0.9 cm^{-1}, respectively. For uniaxial or biaxial stress, a linear relationship between stress and Raman shift is established with the following formula [85]:

$$\Delta\omega(\text{cm}^{-1}) = -2\sigma(\text{GPa}). \tag{3.1}$$

From Equation 3.1, the reported values of the TO-peak shifts should correspond to $\sigma \approx -350$ MPa and $\sigma \approx -450$ MPa for Line A and B, respectively.
In conclusion, different features arise in the low range of the wavenumbers, as Figure 3.5d displays. A broad region around ≈ 150 cm^{-1} appears only for the modified material.

Table 3.1: Peak position ω_0 and FWHM of the characteristic TO-peak acquired by Raman spectroscopy from points within the surface laser-written lines. The parameters were obtained from a Gaussian fit of the spectra reported in Figure 3.5b-d.

Data	ω_0 (cm^{-1})	FWHM (cm^{-1})
Reference	520.304 ± 0.010	4.072 ± 0.017
Line A	519.63 ± 0.03	5.013 ± 0.077
Line B	519.45 ± 0.03	5.13 ± 0.09

3.2 Characterization of the separated wafers

The separated wafers are characterized by measuring the lifetime, performing Raman spectroscopy on a few selected spots on the wafer surface, acquiring SEM surface images and AFM topographies, and electrically probing the surface properties with conductive AFM. The aim is to determine the effect of the SLIM-cutting process.

3.2.1 Effective lifetime measurements

Figure 3.6 reports the μ-PCD analysis of the separated wafers (top row) and the remaining silicon thin foil (bottom row), which is attached to the substrate. Figures 3.6a and 3.6e correspond to the wafer detached rapidly cooling in liquid nitrogen (see Figure 2.1-081). Figures 3.6b-d and 3.6f-h correspond to the wafers detached cooling at room temperature, after being heated up (see Figures 2.1-062,072,073). The resulting average minority carrier lifetime (MCLT) values and the sample thicknesses are reported in Table 3.2.

Table 3.2: Average effective minority carriers' lifetime τ_{eff}, which is calculated over the whole area of the μ-PCD MCLT map. Final thickness W: for the Si/substrate both the epoxy and the Si foil attached to it contribute to the final thickness. Only for sample 081, it was possible to calculate the thickness of the Si foil only. For each sample, the correspondent MCLT map is indicated.

Sample id.	τ_{eff} (μs)	W (mm)	MCLT map
081 wafer	20 ± 4	0.550 ± 0.010	Fig.3.6a
062 wafer	71 ± 4	2.000 ± 0.014	Fig.3.6b
072 wafer	30 ± 4	1.86 ± 0.03	Fig.3.6c
073 wafer	26 ± 5	1.88 ± 0.03	Fig.3.6d
081 Si foil	1.3 ± 0.8	0.433 ± 0.010	Fig.3.6e
062 Si/sub	2.0 ± 0.9	1.87 ± 0.04	Fig.3.6f
072 Si/sub	1.2 ± 0.6	1.61 ± 0.02	Fig.3.6g
073 Si/sub	1.2 ± 0.6	1.63 ± 0.04	Fig.3.6h

Sample 081, cooled in liquid nitrogen, has an average MCLT of (20±4) μs, but the distribution is not uniform (Figure 3.6a). Indeed, the central part has $\tau_{eff} = (23 \pm 2)$ μs, which is higher than the average MCLT of the top and bottom edges, which is equal to $\tau_{eff} = (17 \pm 4)$ μs. The strong reduction at the edges is attributed to the separation process and not to the laser-writing one. The Si/substrate (Figure 3.6e) has an extremely low lifetime, with an average of (1.3 ± 0.8) μs. Interestingly, although this MCLT map does not show all the edges, the

bottom one shows a slightly higher lifetime of (1.9 ± 0.9) μs, while the central part has a lower MCLT of (0.8 ± 0.2) μs.

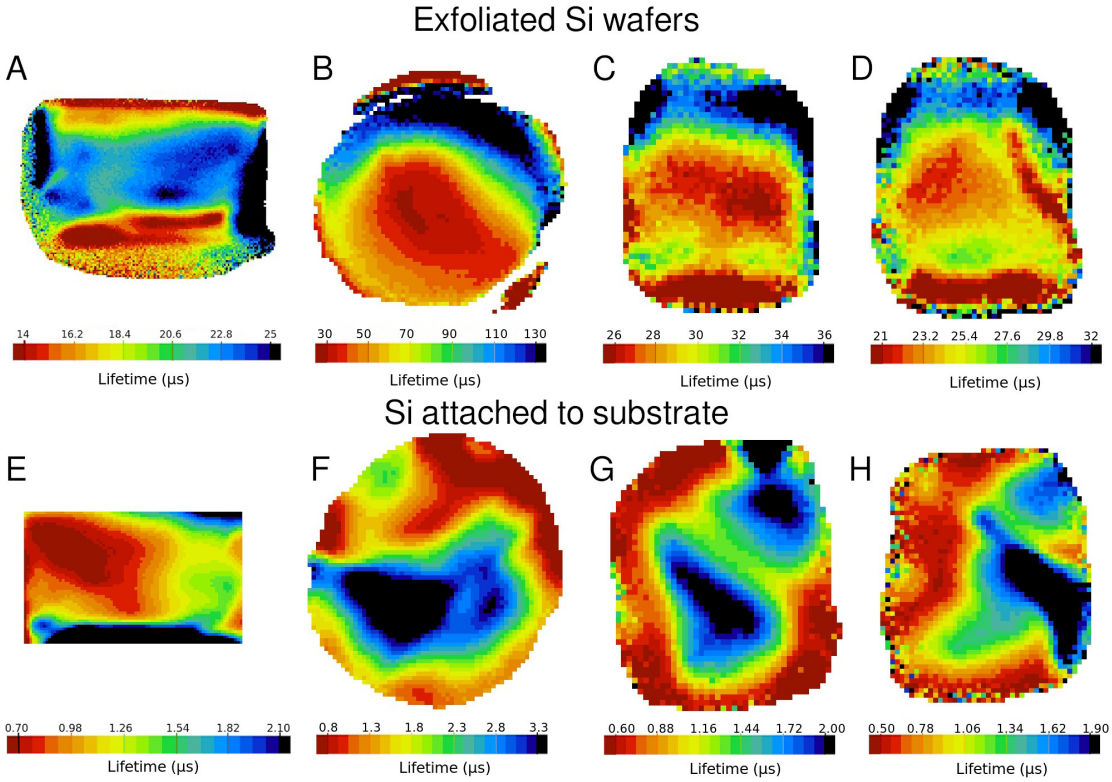

Figure 3.6: μ-PCD lifetime maps of the separated wafer (top) and of the Si/substrate (bottom). Note the different colour bar scales for all the maps. The analyzed samples are 081 **(a,e)**, 062 **(b,f)**, 072 **(c,g)** and 073 **(d,h)**, with the identification label that refers to Figure 2.1.

To verify the validity of these results, an unmodified silicon wafer was used as a reference. The specifications of this wafer are the same as the wafer which was laser-processed. The reference average MCLT is $\tau_{eff} = (36.7 \pm 0.6)$ μs and the distribution is uniform across the sample surface. Therefore, the sample presents an MCLT reduction of 46% relative to an untouched wafer.

The wafers separated cooling at room temperature (Figures 3.6b-d) have the opposite behaviour. Indeed, the sample centre has a lower lifetime than the upper edge. All the Si/substrate samples (Figures 3.6f-h) show regions of a higher lifetime located in the centre, but the distribution is more uniform. Indeed, one could calculate the average MCLT from specific regions of the Si/substrate, only finding out that these values are all within the error associated with the average. As a

consequence, none of the regions is significantly different from the others in terms of MCLT, even if the colour map shows different colors.
Sample 062, with an average value of (71±4) μs, has the highest MCLT among all the measured samples, as deduced from the values in Table 3.2). On the contrary, samples 072 and 073 have an MCLT slightly higher than sample 081, with (30±4) μs and (26±5) μs, respectively. The Si/substrates all have comparable lifetimes, which are extremely low relative to their complementary detached side. In this case, it is not possible to calculate how much the lifetime decreased due to the lack of a reference sample.

3.2.2 Raman spectroscopy of selected spots on the surface

A low MCLT is often associated with the presence of defects, such as dislocations [30, 86] or micro-cracks [31], but the present SLIM-cut technique could have another major drawback related to the possible modifications of the silicon properties due to the laser-writing process. Indeed, the results presented in Section 3.1 showed the presence of tensile stress, polycrystallization and amorphization of the modified material. Aiming to assess the possible difference between a SLIM-cut wafer and an unmodified wafer, Raman spectroscopy was employed also in this case, selecting specific spots on the wafer surface. The spots were chosen to take into account the different regions resulting from the MCLT maps.

The results for the 081 wafer and the Si/substrate sample are reported in the bottom row of Figure 3.7. Three spectra were acquired in three spots of the separated wafer and two on the Si/substrate surface. The typical features of c-Si are present in all the spectra and the spectra do not show any difference between each other. Moreover, an accurate analysis of the TO-peak position and FWHM (see Figure 3.9a) confirms that the five Raman acquisitions have the TO-peak centred around 520 cm^{-1} without any significant shift or broadening.

The Raman spectroscopy analysis of the other samples is displayed in Figure 3.8. The spectra all resemble the Raman spectrum of the previous sample (Figure 3.7). The TO-peak is present, alongside the broad region between 930 and 1040 cm^{-1}.

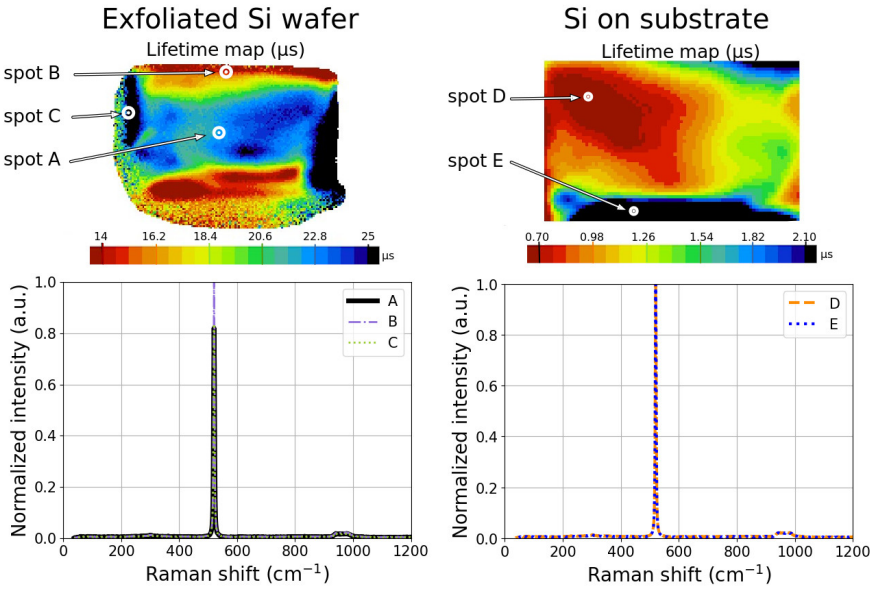

Figure 3.7: μ-PCD measurements of the effective MCLT (top) and Raman spectroscopy of selected spots on the sample surface (bottom) for the separated wafer (left) and Si/-substrate samples (right). The MCLT map of the Si wafer was acquired with a sensitivity of 200 mV and a spatial resolution of 250 μm; while the map of the Si/substrate sample with 500 mV sensitivity and spatial resolution of 250 μm. Note the different colour bar scales for the two maps. The Raman spectra were acquired with the 532 nm laser, 50x magnification, 2s exposure and 5 mW power. The labels of the different spectra correspond to the spots indicated with an arrow on the maps.

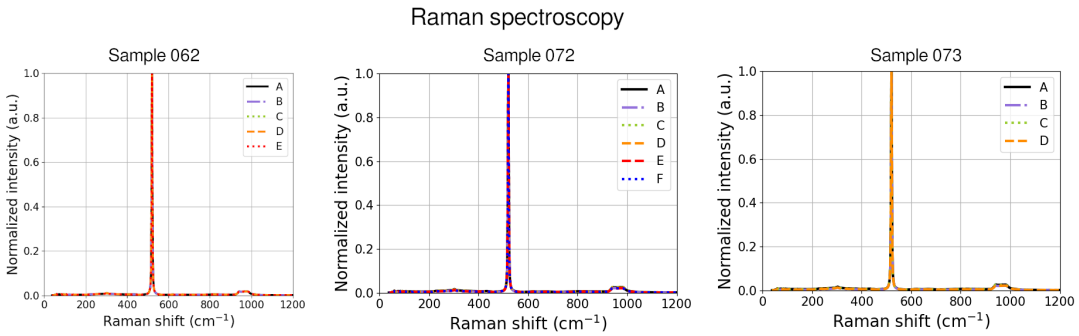

Figure 3.8: Raman spectroscopy of selected spots (see corresponding MCLT maps in Figure 3.9) on the sample surface for the separated wafer and Si/substrates. The Raman spectra were acquired with the 532 nm laser 50x magnification, 2s exposure and 5 mW power.

However, differences are found considering the position and broadening of these TO-peaks. The upper edge of sample 062 (see Figure 3.9b) has a slightly shifted TO-peak relative to the peak from the centre of the wafer. As before, the TO-peak position is still centred around 520 cm^{-1} and any broadening is absent.
The Si/substrate sample has a shifted peak in the central region (point C in Figure 3.9b). The amount of this shift relative to the closer data point (D in Figure 3.9b) is $\Delta\omega = 0.217$ cm^{-1} towards lower wavenumbers, which corresponds to a tensile stress of $\sigma \approx -109$ MPa, using Equation 3.1. Note that this tensile stress is calculated considering another modified region. The peak is not broadened. Moreover, even if the MCLT map shows different colors, the central region does not have an average MCLT significantly higher than the upper edge. Thus, the TO-peak shift does not correspond to a different MCLT.
Sample 072 in Figure 3.9c has a similar behaviour: the TO-peak acquired from the centre of the Si/substrate shows a shift of $\Delta\omega = 0.166$ cm^{-1} towards lower wavenumbers relative to the spectrum of a spot in the upper edge. The shift corresponds to $\sigma \approx -83$ MPa. The spectra acquired from the separated wafer of this sample do not have anomalous features.
The TO-peaks of the spots from the 073 Si/substrate do not show any difference from the typical c-Si TO-peak, as displayed in Figure 3.9d. On the contrary, the TO-peak acquired in the upper edge of the separated wafer is $\Delta\omega = 0.393$ cm^{-1} shifted towards lower wavenumbers relative to the spectrum acquired from the centre. Thus, the tensile stress is $\sigma \approx -197$ MPa. In this case, the average MCLT of the upper region is significantly higher than the MCLT of the central region. Indeed, the upper edge has an average MCLT of (31 ± 5) μs, while the centre of (23 ± 2) μs.

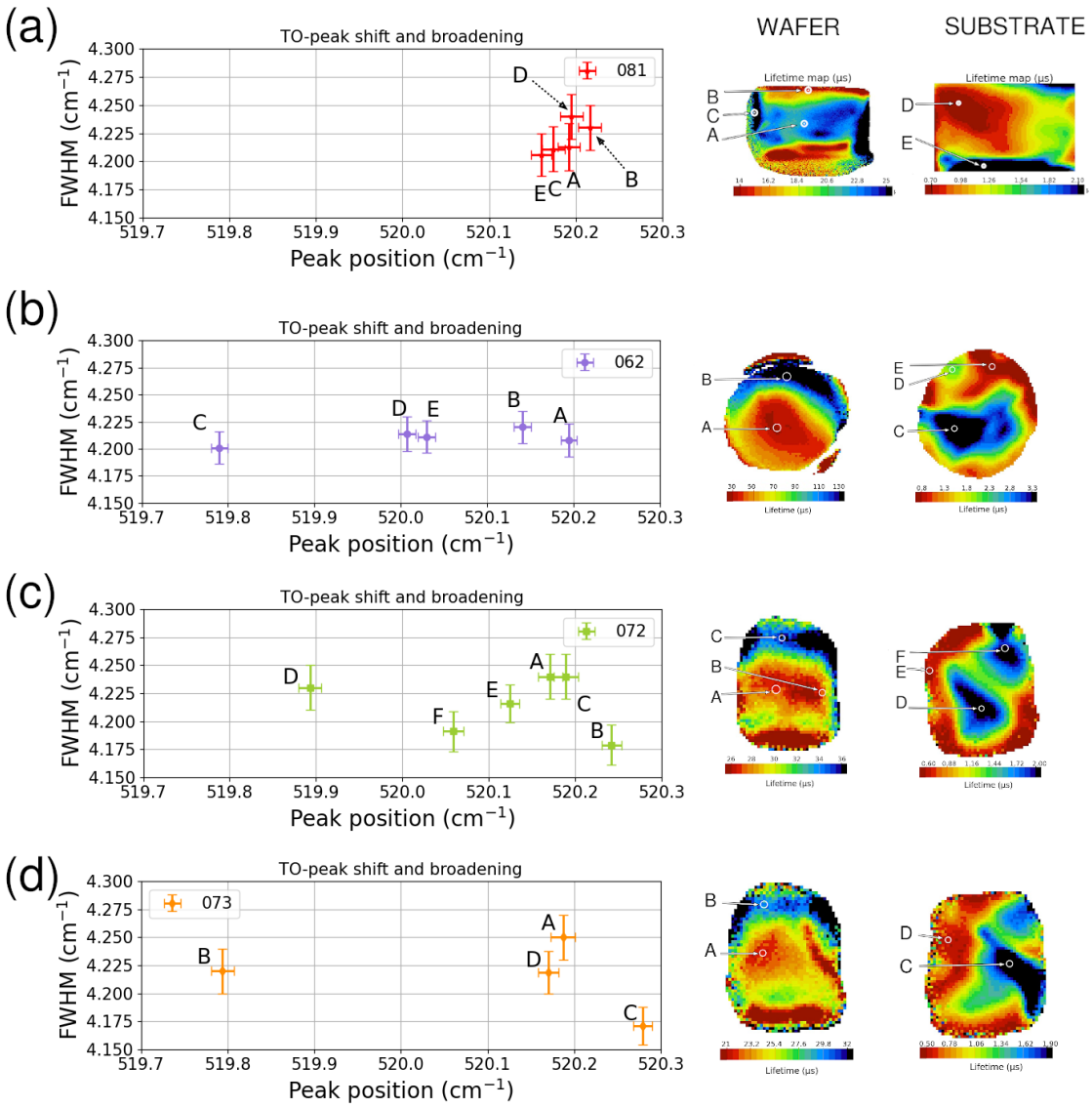

Figure 3.9: Results of the Gaussian fit providing the TO-peak position and FWHM of the Raman spectra acquired from selected spots on the wafer surface of the separated Si wafers and the Si/substrates: **(a)** 081, **(b)** 062, **(c)** 072, **(d)** 073. The MCLT maps, on the right-hand side, show the position of the analyzed spots (indicated by arrows). The label of these spots is also reported on the scatter plot for each sample. The Raman spectra were acquired with the 532 nm laser, 50x magnification, 2s exposure and 5 mW power.

Comparison of the Raman spectra with a reference Silicon wafer

The previous analysis is useful to find a correlation between the Raman results and the different regions of the same sample surface. However, the shifts and the broadening of the TO-peaks were calculated considering other spectra belonging to the same sample. Therefore, an interesting comparison is with the silicon reference Raman spectrum, which was considered in Section 3.1.2. Indeed, the Raman spectrum was acquired from the polished surface of the silicon wafer, where the influence of the laser-writing process is excluded. The TO-peak position and FWHM of this spectrum are reported as "Reference" in Table 3.1. The data presented in Figure 3.9 are gathered in Figure 3.10 to make a comparison with the reference TO-peak.

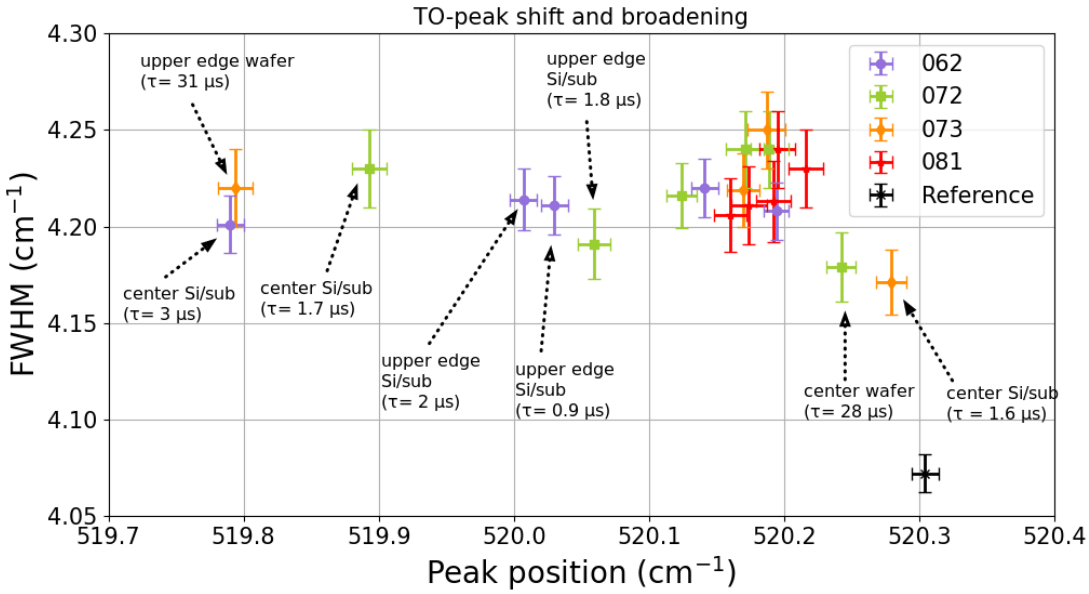

Figure 3.10: Results of the Gaussian fit providing TO-peak position and FWHM of the Raman spectra acquired from selected spots on the sample surface. The data set for each sample is labelled with the sample name, different colour and marker. For sake of simplicity, the labels of the different spots where the Raman spectra were acquired are not indicated here, but some comments are reported to link the spot to the location in the MCLT maps in Figure 3.9. The calculated lifetime of the region surrounding the spot is also reported. The reference data come from the unmodified region of the polished silicon wafer.

From Figure 3.10 it is easier to recognize a common trend of the TO-peak shift and broadening with the spot location on the sample surface and lifetime.
The regions showing the lowest shift and broadening are the central parts of the 072 separated wafer (see spot B in Figure 3.9c) and the central part of the 073 Si/substrate (see spot C in Figure 3.9d). The MCLTs of these regions are extremely different from each other, i.e. (28 ± 2) μs and (1.6 ± 0.5) μs, respectively.
The regions presenting the highest shift are the centre of 062 Si/substrate (see spot C in Figure 3.9b) and the upper edge of the 073 separated wafer (see spot B in Figure 3.9d). The former has a shift of $\Delta\omega = (0.514 \pm 0.020)$ cm^{-1} and it is (0.13 ± 0.02) cm^{-1} broader than the reference TO-peak. The latter has a shift of $\Delta\omega = (0.510 \pm 0.023)$ cm^{-1} and it is (0.15 ± 0.03) cm^{-1} broader than the reference TO-peak. The shifts are associated by Equation 3.1 with a tensile stress of $\sigma = (-257 \pm 10)$ MPa and $\sigma = (-255 \pm 12)$ MPa, respectively. Similarly to the previous case, the MCLT values of the two regions are extremely different from each other: (3.0 ± 0.6) μs for spot C in Figure 3.9b and (31 ± 5) μs for spot B in Figure 3.9d.
Other significant shifts are found for the upper edges of 062 and 072 Si/substrate (see spots D and E in Figure 3.9b and F in Figure 3.9d). These regions have a comparable average MCLT.
The TO-peak position is close to the reference one for all the other spots, but the peaks seem the broadest. For instance, considering only the data from the largest sample, i.e. 081 in Figure 3.9a, the average shift, calculated from the five acquired spots, is $\Delta\omega = (0.117 \pm 0.010)$ cm^{-1}, which corresponds to average tensile stress of $\sigma = (-58 \pm 5)$ MPa. The TO-peak is (0.148 ± 0.006) cm^{-1} broader than the TO-peak of the reference spectrum.

3.2.3 Morphological study with AFM and SEM

To characterize the morphology of the wafer surface AFM was employed to obtain the topography with TM-AFM and contact AFM or current maps in C-AFM. Figure 3.11 shows the surface topographies of samples 081 and 062. The surfaces present some stair-like features on a ≈ 10 nm scale (Figures 3.11a,d). The height of these features is ≈ 60 nm in sample 081 and $\approx$ 100-400 nm in sample 062 (Figures 3.11c,f). Considering also Figure 3.12, the surface of 062 appears less uniform than that of 081. Moreover, the root-mean-square roughness (rms) is one order of magnitude higher in 062. On a smaller scale (Figures 3.11b,e), the surface presents a "streaked" texture with oblique "stripes". The rms roughness of two almost flat regions is (0.92 ± 0.10) nm and (1.2 ± 0.3) nm for 081 and 062, respectively. The height between the valleys and the peaks of the "stripes" ranges from 1.7 nm to 4.9 nm. Nevertheless, it seems that the laser-induced modifications are not visible from these measurements.

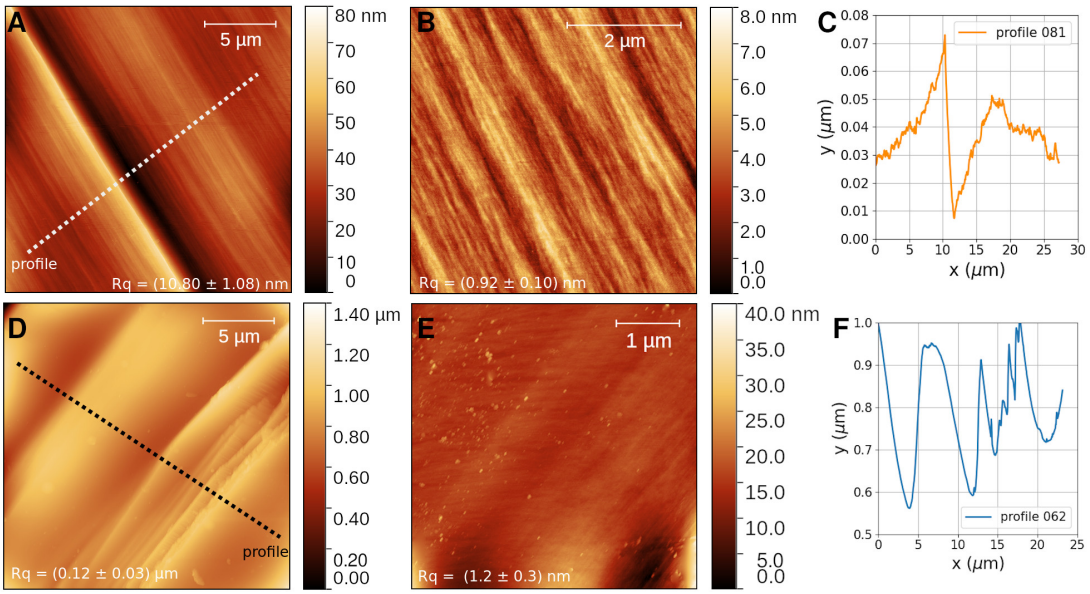

Figure 3.11: Topographies of 081 (top) and 062 (bottom) acquired with TM-AFM with tip I. The images are 20×20 μm^2 **(a,d)** and 5×5 μm^2 **(b,e)**. Two profiles are reported in **(c,f)**, extracted from **(a,d)**, respectively. The tip used in (a,b) has resonant frequency f=291 kHz, quality factor Q=387 and phase difference $\phi = 240°$. The tip used in (d,e) has resonant frequency f=214 kHz, quality factor Q=381 and phase difference $\phi = 182°$. The value of the rms roughness (Rq) is reported.

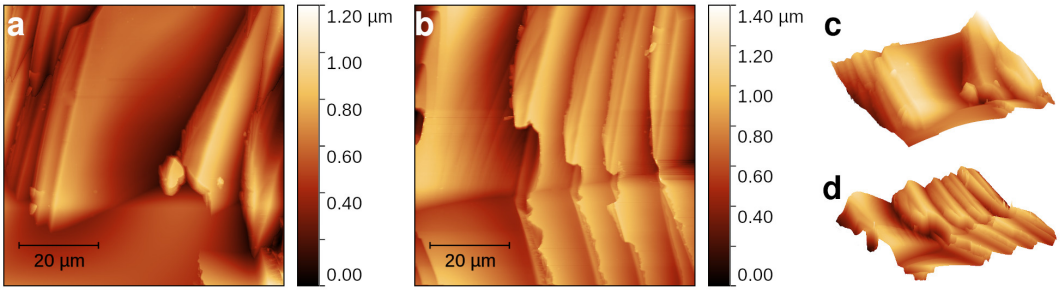

Figure 3.12: Topographies of 062 (70×70 μm^2) acquired with contact AFM. Tip III and IV were employed for (a,c) and (b,d), respectively.

The samples were analyzed in the SEM to verify the absence of laser-induced modifications on the surface. At the beginning of the measurements ($\leq$ 5 min),

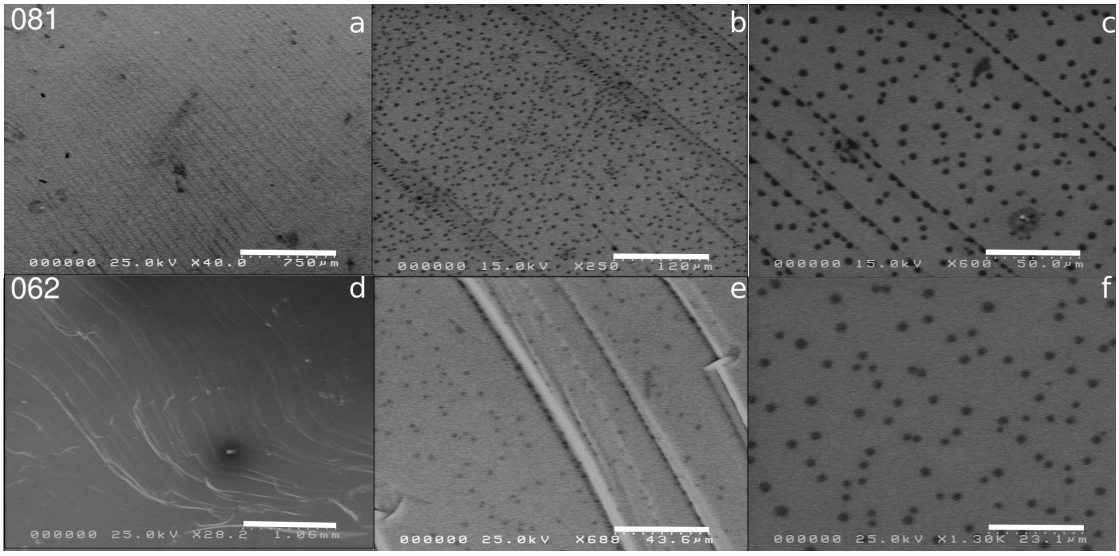

Figure 3.13: SEM images of 081 (top row) and 062 (bottom row) at different magnification with Hitachi S4000 SEM. The images were acquired with an acceleration voltage of 25 kV in air. The scale-bars are: **(a)** 750 μm, **(b)** 120 μm, **(c)** 50 μm, **(d)** 1060 μm, **(e)** 43.6 μm, **(f)** 23.1 μm.

the surface did not show any feature linked to the modification process (Figures 3.13a,d). A pattern of lines emerges, and it is attributed to the exfoliation step. In particular, sample 081 has a pattern of dense, straight and regularly-spaced lines. On the other hand, sample 062 shows an irregular pattern: the lines are often neither continuous nor straight, but they suddenly break off. This result is in agreement with 062 topographies (Figures 3.11d,e and 3.12), where the distance between the stair-like features decreases, and the reciprocal distance is not constant.

After some time, the defects became visible (Figures 3.13b-c,e-f). The distribution seems random in the flat areas, but the defects become closer and accumulate along the topographic lines. The shape and size of these dark spots are consistent with what is expected for laser-induced modifications. Qualitatively, the shape is regular and circular.

The size distribution of the dark spots (see Figure 3.14) shows that the spots on sample 081 have a mean area of $(7.8 \pm 0.4)\mu m^2$, while those on sample 062 of $(3.18 \pm 0.08)\mu m^2$. Thus, the mean diameter values are $(3.15 \pm 0.08)\mu m$ and $(2.01 \pm 0.03)\mu m$, respectively.

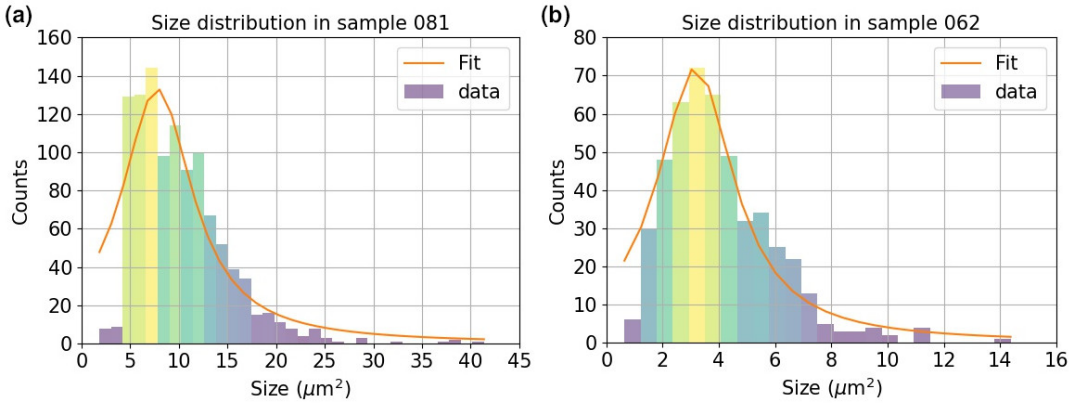

Figure 3.14: Size distribution obtained from the analysis of the black dots in the SEM images: **(a)** sample 081 and **(b)** 062. The software ImageJ was employed to perform a particle analysis routine. The obtained distribution is fitted with a Lorentzian curve. For sample 081 the data were collected from 700x, 800x, 250x images and the fit parameters are $\mu_0 = (7.8 \pm 0.4)\mu\text{m}^2$ and $\sigma = (4.4 \pm 0.6)\mu\text{m}^2$. For sample 062 the data were collected from 703x, 800x, 1300x images and the fit parameters are $\mu_0 = (3.18 \pm 0.08)\mu\text{m}^2$ and $\sigma = (1.65 \pm 0.13)\mu\text{m}^2$.

The fact that these dark spots "emerged" from the surface during the SEM imaging process had to be investigated. For this reason, new topographies were acquired employing a conductive tip in TM-AFM, a conductive tip in contact mode and an insulating tip in contact mode. Figures 3.15a and 3.15b, acquired in contact mode, do not show any feature on the surface. The random distribution of the black spots, their regular shape and their topographic absence lead to conclude that the black spots were not created by the deposition of particles during the SEM imaging. However, strongly visible features were detected with TM-AFM, as shown in Figure 3.15c,d. Their height saturates the scale and the rest of the surface appears flat.

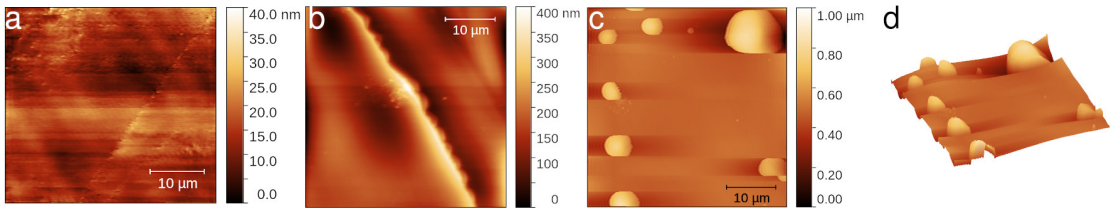

Figure 3.15: Topographies of 081 (40×40 μm^2) after the SEM measurement : **(a)** contact AFM with tip V; **(b)** contact AFM with tip II; **(c,d)** TM-AFM with tip I: resonant frequency f=214 kHz, quality factor Q=395 and phase difference $\phi = 275°$.

3.2.4 Electrical analysis with C-AFM

In addition to the morphological analysis, the electrical characterization was performed using C-AFM. The idea was to scan the surface to see if the laser-induced modifications were electrically active or if they contribute to the conductivity differently than the unmodified parts. The presence of defects on the surface was assured by the SEM results reported above. Two current maps are reported in Figure 3.16, alongside the topography. Neither spots nor significant changes in the current are detected. The maps contain only noise.

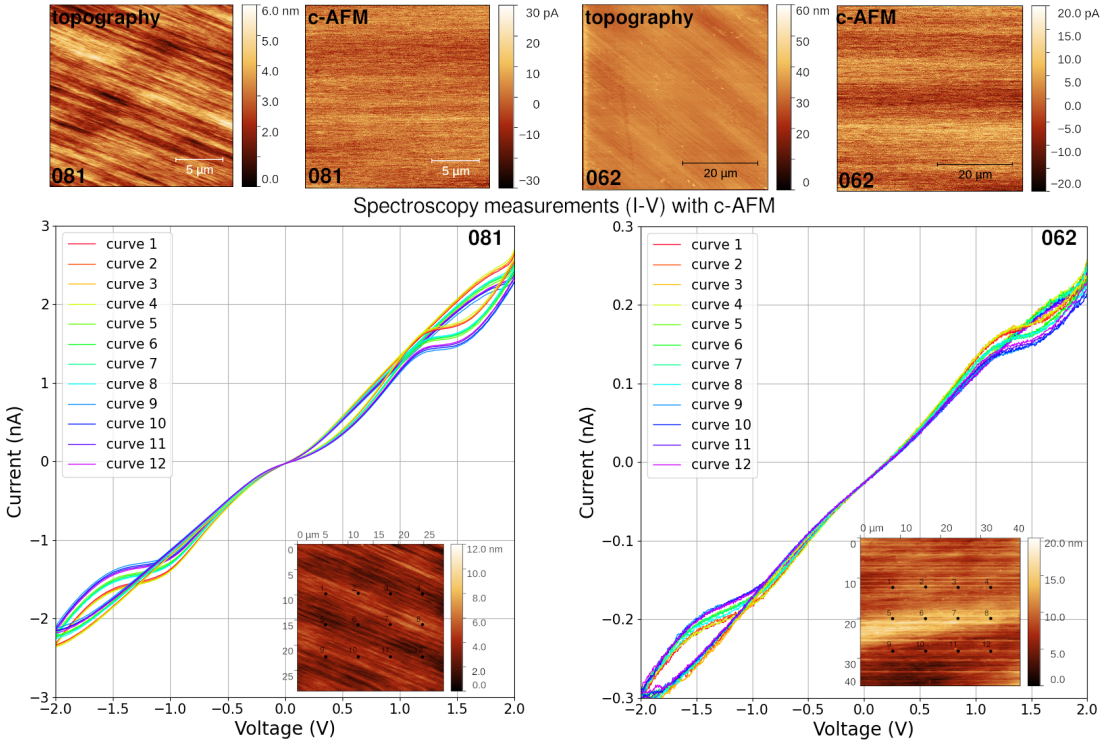

Figure 3.16: Topographies, current maps (above) and I-V curves (below) of 081 and 062 acquired with C-AFM with tip II. The applied voltage is $V_0 = -1$V and $V_0 = -1.8$V for the current map of 081 (30×30 μm^2) and 062 (40×40 μm^2), respectively. For the I-V curves the applied voltage sweeps from -2V to +2V and each curve is acquired in 10s. Only 12 out of 100 I-V curves are reported and the correspondent spots are indicated in the inset (30×30 μm^2 topography).

Indeed, the maximum values of the current are very low for doped silicon. Figure 3.17 also reports three topographies and the correspondent current maps acquired with higher input voltage. As before, the maps show only noise.

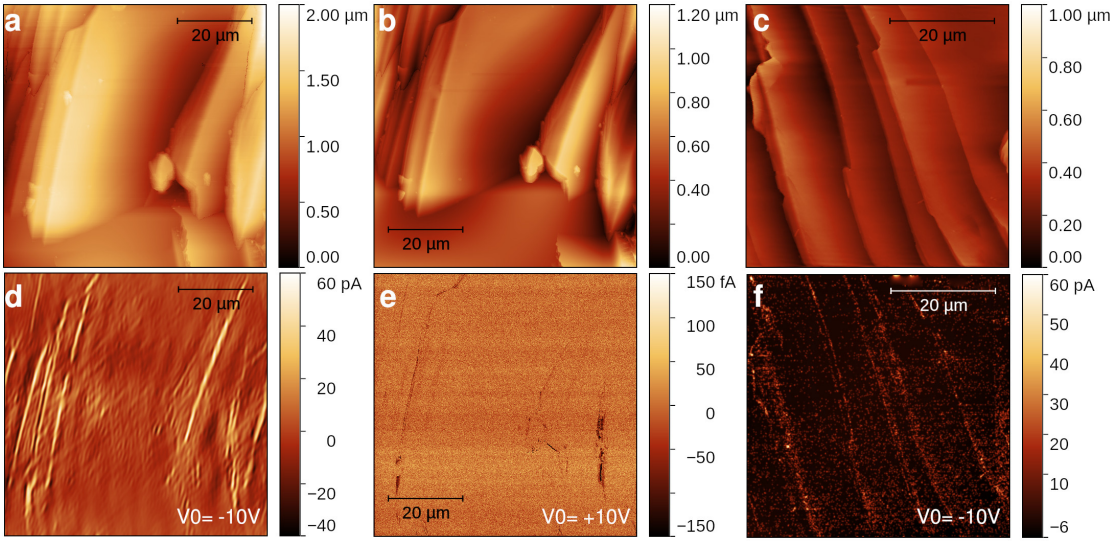

Figure 3.17: Topographies and current maps of 062 acquired with C-AFM with different applied voltages (reported in figure). Tip III were employed for **(a,d)** and **(b,e)**, while tip IV for **(c,f)**. The images are 70×70 μm^2 for (a,b,d,e) and 50×50 μm^2 for (c,f).

Also in Figure 3.16, the I-V curves acquired with spectroscopy from -2V to + 2V are shown. The selected spots are indicated in a reference topography. For clarity's sake, only twelve curves are reported, because all the 100 curves present the same behaviour without significant differences.
In the case of sample 062, the trend is almost linear for low input voltages, which agrees with the ohmic behaviour of the metal/semiconductor (tip/sample) junction. For higher voltages, the curves strongly deviate from the linearity. The latter trend dominate the entire spectrum of the curves in sample 081. In both cases, the hysteresis for a positive bias is smaller than for a negative bias.
It is important to note that the grid of measured spots during the spectroscopy was made dense enough to be sure of probing at least one modified spot. The step size is 4 μm for acquisitions on sample 062 and 3 μm for sample 081. Therefore, the dimension of the black spots in SEM images is bigger than the step size. As a consequence, the absence of diversity between the 100 I-V curves means that the defects do not show any difference in conductivity relative to the defect-free regions.

Chapter 4

Discussion

4.1 Characterization of bulk modifications

Morphology

The characterization of the laser-induced modifications confirmed the expected morphology for the buried defects. They are not point-like structures localized at the focus spot but rather elongated in the direction parallel to the laser beam [6, 38, 44]. The shape of these defects is not regular. Sometimes they are arched or more circular. There is no connection between this irregularity with the energy of the laser pulse. On the contrary, the modification depth decreased with increasing energy. Moreover, it appeared clear that not all the defects were successfully inscribed into the silicon bulk. Therefore, not only an energy threshold must be overcome to induce the modifications, but the energy must also be optimized for the desired depth [46, 61, 62, 66].
Previous studies showed the presence of cracks and voids on the exposed surface near the modifications [38, 46, 49]. Nevertheless, the SEM analysis did not report any of these damage signs. This result is in agreement with *Wang et al.* [48] and *Yu et al.* [53], who concluded that the pulse energy of a few μJ might merely induce a local change of density. Indeed, the estimated delivered energy density in the modified volume is orders of magnitude below the damage threshold for cracks and voids.
Note that the acquired signal of the SEM images in Figure 3.1-3.2-3.3 is not secondary electrons (SE), but it is backscattered electrons (BSE). Indeed, the SE signal did not show the defects as clearly as BSE. This may have an interesting interpretation: a higher contrast in the BSE signal may mean that there is no topographic difference between the modified surface area and the unmodified silicon. Collecting the BSE signal from a deeper interaction volume allows us to identify the modifications. The signal coming from the modified material is brighter, which

can be associated with the different phases, maybe amorphous or polycrystalline, of this region [46, 47].

Raman spectra

The Raman analysis did not detect any significant presence of stress, amorphization or polycrystallization in a region where both unmodified and modified silicon is present. Indeed, the spectrum from this region is comparable to the reference spectrum acquired from an unmodified silicon region. Therefore, the hypothesized amorphization or presence of stress is probably reduced to the defect area and not the surrounding one. Nevertheless, the Raman spectrum from a region with a high density of modified material confirms that the laser forms the polycrystalline and amorphous phases, as confirmed by several recent studies [9, 37, 43, 48–51].
The resulting shift of the TO-peak may be caused by the presence of tensile stress or polycrystallization. Indeed, the presence of tensile stress for shifts towards lower wavenumbers has been previously reported for laser-induced defects in silicon [25, 49]. The shifts of the TO-peak in the spectra of the modified material and the stress values are comparable to the results of *Kammer et al.*, who found a TO-peak shift of 1 cm^{-1}, corresponding to uniaxial stress of 500 MPa or in-plane biaxial stress of 250 MPa [84]. The stress is tensile and not compressive, being negative [87].
The presence of crystal disorder causes the broadening of the TO-peak and its asymmetry [47, 49, 68]. The FWHM increase of $\sim +2$ cm^{-1} was previously associated with pc-Si having crystallite sizes between 5 and 10 nm [47]. However, the presence of pc-Si is also associated with a feature at 510 cm^{-1} [68], which is absent in the acquired spectra.
The features at 496 cm^{-1} and around 150 cm^{-1} may correspond to amorphous silicon (a-Si). Indeed, a-Si shows two maxima in the Raman spectrum: one around 500 cm^{-1}, arising from the optic phonon branch, and one around 150 cm^{-1}, arising from the acoustic branch [75]. In addition, a-Si was previously associated with additional features between 430 and 500 cm^{-1} [25, 68, 84], but also with a broad band around 473 cm^{-1} [47].

4.2 Characterization of the separated wafers

Minority carriers' lifetime, thickness and carrier diffusion length

The wafer that was separated rapidly cooling in liquid nitrogen showed a 46% drop of the MCLT relative to an unmodified silicon wafer with the same characteristics. On the other hand, for the foils separated at room temperature, the

absence of another reference wafer does not allow us to calculate the lifetime reduction caused by the SLIM-cutting process.
A comparison may be established with the work of *Serra et al.* [31], who reported that the wafer effective MCLT was in the range of 8-25 μs and improved up to 20-45 μs after etching the surface. The MCLT drop was around 60%. *Bellanger et al.* [30] obtained effective lifetime values of 28 μs after passivating the surface, with a 53% drop. The reduction of the MCLT is typically associated with the increase of the dislocation density, and the presence of micro cracks or recombination centres close to the surface [31]. For instance, a value of 2×10^5 cm^{-2} causes a decrease in the lifetime of three to five times smaller than the value of a reference Cz-Si wafer, which typically shows a dislocation density of 1×10^4 cm^{-2} [30].

In general, the values of the MCLT measured with the present μ-PCD technique after SLIM-cutting are lower than the desired lifetime for PV applications. Indeed, commercial-grade silicon wafers typically have MCLT values of a few milliseconds [86, 88]. However, the measurements were performed without passivating the silicon surface.
According to Section 1.1.2, the contribution of surface recombination without any passivation is high and can be approximated with $2S/W$, where $S \approx 5 \times 10^4$ cms^{-1} is the surface recombination velocity [13] and W is the wafer thickness (see Eq. 1.5). Considering n-type wafers with thicknesses reported Table 3.2, τ_{surf} is in the range of 0.5-2 μs. Then, assuming a hole diffusivity of $D_h \approx 12$ cm^{2}s^{-1} [89], τ_{diff} is in the range of 25-340 μs. Thus, the approximate theoretical bulk lifetime is $\tau_{bulk} \approx 30 - 90$ μs.
For instance, the theoretical underestimation of the MCLT for sample 081 would be 77% considering that $\tau_{eff} = 20$ μs and $\tau_{bulk} \approx 86$ μs. The value is in agreement with some previous experiments stating that the effective MCLT measured without passivation could be 70-90% underestimated [14].
Regarding the application to the PV field, good performances of an operating solar cell were obtained by *Bellanger et al.* [30]. They reported a conversion efficiency of 12.6% under 1-sun AM1.5 G spectrum, for a simple device fabricated with 135-μm-thick SLIM-cut Si foil. The value is only 1.4% lower than the efficiency of the same device fabricated with a reference silicon wafer. The separated wafer had an MCLT of 28 μs after passivation and the low MCLT was considered the main cause of the lower efficiency.

The sample that was cooled in liquid nitrogen has the thinnest thickness (see Table 3.2) and it is one order of magnitude lower than the others. Therefore, this sample is more than three times thicker than the n-type wafers required for PV applications, which have a thickness of 0.16 mm. The other samples, cooled at room temperature, are twelve times thicker than 0.16 mm. These results are unexpected considering that previous results reported the achievement of 40-μm-

thick up to 140-μm-thick SLIM-cut wafers [7, 30–34].
Moreover, commercial n-type wafers with an MCLT of 1 ms have a carrier diffusion length much longer than their thickness [21]. A 160-μm-thick wafer with $\tau = 1$ ms would have $L \approx 10^4$ μm, which is six times greater than the thickness. If the carrier diffusion length is higher than the material thickness, good efficiencies for the solar energy conversion are expected [7].
However, the range of the diffusion lengths is ~ 35 μm for the Si/substrates and 150-290 μm for the separated wafers. These values were extracted from Equation 1.4, assuming a hole diffusivity of $D_h \approx 12$ cm^{2}s^{-1} [89]. Therefore, the diffusion lengths are four or six times shorter than the thickness (see Tab.3.2).
The 20-40 μs MCLT values of wafers with thickness in the range of 110-135 μm, obtained by [30, 31], would be more compatible with the PV market requirements. The MCLTs correspond to L=155-220 μm, which are slightly higher than the foil thickness.

Raman spectra

Raman spectroscopy did not highlight any significant shift or broadening of the TO-peak in the spectra acquired from the surface of the wafer separated with cooling in liquid nitrogen. Thus, the SLIM cutting did not induce any phase change in these samples, and the presence of strain is not significant. The other three wafers showed small changes in the Raman spectra for some surface regions. The stress calculated from the largest TO-peak shift is lower than the stress obtained for regions with high defect density [84]. In conclusion, considering Figure 3.10, the presence or absence of tensile stress is not correlated with the position of the spot on the sample surface and the measured MCLT.

Morphology and roughness

In the literature, it is difficult to find references about the roughness of native silicon wafers because most of the results refer to polished or treated wafers. The common cutting techniques produce wafers with a macroscopic average surface roughness in the range of 0.2-0.5 μm [29, 90]. Employing the AFM, rms roughness values of $\approx$ 0.1-0.2 nm or average roughness of 0.03-0.04 nm are measured for polished wafers (AFM 1×1 μm^2 images) [90, 91]. The morphology is typically uniform with a grain-like aspect (Figure 4.1a-b) [92].
On the contrary, the analyzed wafers have an rms roughness of 0.92 nm and 1.2 nm (AFM 5×5 μm^2 images). The morphology presents a streaked-like microscopic structure, which does not resemble any other silicon AFM topography image in the literature.
There is a resemblance with SiC microscopic structure (see Figures 4.1c-f). *Vecchio*

et al. determined an rms surface roughness of 0.2 nm and features of 15 nm height [93]. Similarly, *Oliveros et al.* determined an rms surface roughness of 0.3 nm (TM-AFM 5×5 μm^2 images) [94]. *Canino et al.* found that the height of the features is 0.3-0.6 nm and the rms roughness is around 0.4 nm in 4H-SiC (TM-AFM 7×7 μm^2 images) [95]. Therefore, it seems that the surface roughness is smaller for SiC than for the analyzed samples. The height of the features in the analyzed samples is within the range of 0.3 nm to 15 nm, which is reported in the literature. Despite the topographic resemblance, the Raman spectra acquired from the samples do not coincide with a typical SiC spectrum (Figure 4.1g). Therefore, these results require further investigation.

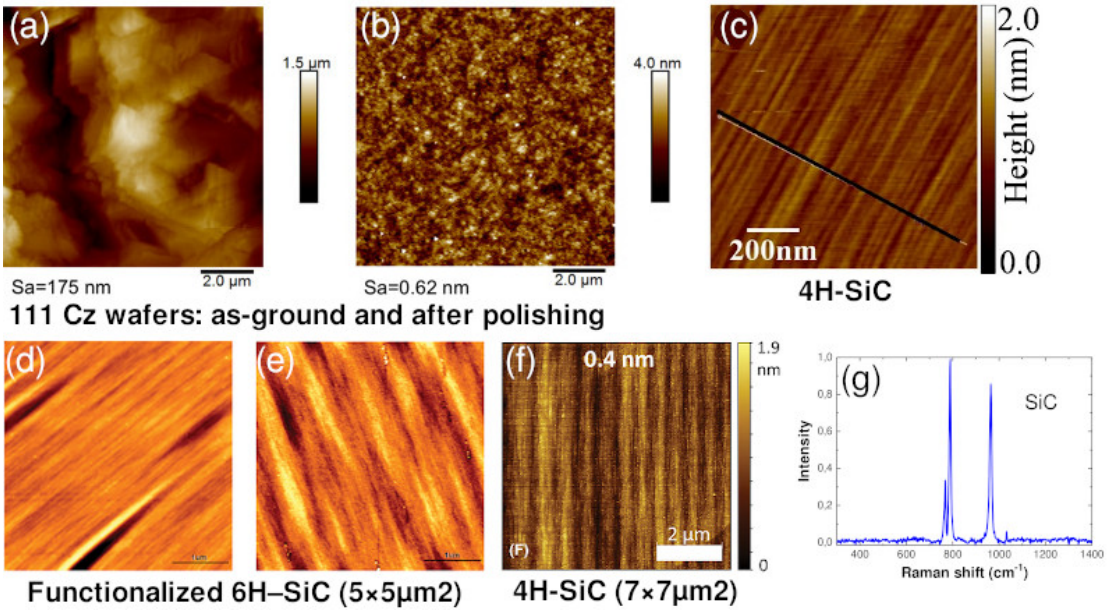

Figure 4.1: **(a-b)** AFM topographies of as-ground and polished 111-oriented c-Si wafers, respectively [92]. **(c)** Morphology of the virgin 4H-SiC (0001) [93]. **(d-e)** TM-AFM topographies of 6H–SiC- and 1-octadecene-functionalized 6H–SiC after alkylation, respectively [94]. **(f)** non-contact AFM topography of 4H-SiC [95]. **(g)** Raman spectrum of SiC [96].

The surface images acquired with the SEM showed that the detachment process creates an inhomogeneous surface with regular straight lines or bent irregular ones, depending on the separation procedure. A rougher surface results from separating with cooling at room temperature. Either the different silicon material, the stress-inducing layers, or the cooling temperature may cause these differences. It is difficult to establish a unique correspondence due to the lack of a systematic study of the separation process.
Interestingly, black spots appeared on the surface while performing the SEM mea-

surements. These spots were not detected with contact AFM. On the contrary, extremely evident round features appeared in TM-AFM topographies, acquired after the SEM measurement. A possible explanation for all these results is the following. The laser modified the monocrystalline silicon bulk properties without causing a strong amorphization. Therefore, Raman spectra acquired from surface spots do not show changes from a typical c-Si spectrum. At the same time, these modified regions were charged by the electron bombardment in the SEM. The charges appear as an increase in the apparent height (artefacts) in the topographic images because they produce an additional electrostatic contribution to the tip-surface interaction while performing TM-AFM. The same issue does not occur in contact mode because the tip/surface junction acts as a conductive path to the ground. Thus, the tip "touches" the surface and only topographic features are detected. The possibility that an involuntary deposition of material created these black spots is discarded because nothing is found in contact mode, although the measurements were made in the air. Similarly, the removal of material by electron bombardment is discarded. The size of the black spots is larger than the size calculated for buried modifications. Indeed, based on the calculations of the mean area, the diameter of the black spots is ≈1-4 μm. These values are more than two times the dimension perpendicular to the laser beam (486 nm), which was found for buried modifications. Nevertheless, the laser beam diameter at the focus was ≈ 2-3 μm, which is comparable with the dimensions of the black spots. Therefore, the presence of these modified regions in the SEM images can be safely associated with the laser-writing process.

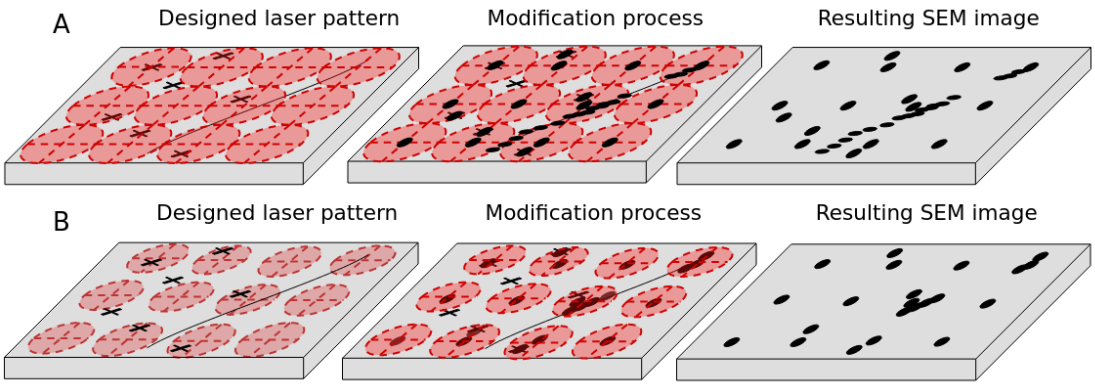

Figure 4.2: Scheme of the possible pattern designs for laser-processing the silicon bulk: **(a)** beam diameter at the focusing depth equal to the step size of the scanning pattern and **(b)** beam diameter smaller than the step size. The silicon material with its intrinsic defects (left) is modified by the laser beam (centre) and may appear in SEM images as a specific pattern of black spots (right).

The distribution of the black spots in the SEM images should be discussed in terms of the beam diameter at the focus and also the step size (5 μm) of the scanning pattern. The reason is that the SEM images show a random pattern of black spots, rather than a regular one. The laser beam may have induced a change in the silicon properties where other defects were already present, considering that the beam diameter is almost equal to the step size. Therefore, the black spots appear randomly distributed in the flat regions, while they appear closer along line defects. This mechanism is schematized in Figure 4.2a. On the contrary, a regular pattern of modified spots (black spots) would appear if the laser diameter was much smaller than the step size, as shown in Figure 4.2b.

Electrical characterization

Lastly, the electrical analysis performed with C-AFM highlighted the lack of a change in the conductive behaviour of the material where the laser-modified areas should be located. Indeed, the I-V curves are all the same and no particular features appear in the current maps.
Moreover, high noise levels characterize the conductive maps. On the other hand, the I-V curves obtained by applying a bias for 10 s are not noisy. This difference could suggest that the surface layers of the material do not conduct well and that a longer time is needed to achieve a significant conductive response. It is known that the silicon surface incorporates a native oxide (which is usually insulating) [82, 97]. This layer avoids lateral propagation and confines the current to the area strictly below the tip. Thus, many papers study local inhomogeneities with I-V curves and not collecting current maps [82].

4.3 Limitations and accuracy of the measurements

The limited accuracy of SEM measurements of the dimensions of the defects is due to their irregular shape. Thus, only three defects with the same shape were considered to calculate the average size. The change of depth of the defects and the distance between each other are accurate because they are quantities relative to the reciprocal position of the defects. On the contrary, the total depth is more difficult to determine because the surface was often chipped and not regular. Moreover, the lack of knowledge of the energy and focusing depth exact values does not allow us to determine the correlation between the focusing depth and the effective depth of the defects. In addition, it is difficult to establish an exact correspondence of the pulse energy with depth.

Microwave-PCD was employed to measure the effective minority carriers' lifetime of the wafers. As was mentioned in Chapter 2, the effective lifetime may be

underestimated due to surface recombination. The surface passivation would lead to better results. The spatial resolution of the measurements was 250 μm. The MCLT average values provided by the software are calculated on 7200 data for the largest sample and 1600 data for the smallest ones.

The Raman spectroscopy analysis of silicon samples is accurate because the monocrystalline and amorphous silicon spectra are well known. Moreover, the high spectral resolution of the instrument assures that the detected peaks are well resolved. However, the beam size of the 532 nm laser on the focal plane is 2 μm and 4 μm, respectively employing the 100x and 50x lenses. Thus, the spatial resolution of the measurements is limited by the effective beam diameter. The peak positions and FWHM were determined by fitting the Raman spectra with the Lmfit Python library, evaluating the quality of the fit through the reduced χ^2 value. The other limitation is the shallow penetration of the 532 nm laser, which should be around ~ 2 μm. This aspect limits the characterization of the material properties to surface analysis.

In addition, the nature of the induced stress is not clear, and it is not possible to determine if it is caused by the presence of the laser-induced modification or by the detachment process. Moreover, it seems difficult to determine if the different separation methods have precise consequences on the wafer properties. Not only considering the MCLTs, but also the wafer thickness. The detachment caused by cooling the wafer in liquid nitrogen produced a much thinner wafer than the detachment at room temperature. However, the latter technique leads to significantly thinner wafers, as reported in the literature.

Chapter 5

Conclusions

The need to find new materials for solar cells is accompanied by that of making the production process of monocrystalline silicon more efficient and sustainable. Indeed, silicon solar cells dominate the market, but the manufacturing process still presents some problems, such as the consistent loss of material occurring during cutting. Therefore, it is of great interest to find new separation methods that are more sustainable than the established ones, such as diamond wire sawing. In this direction, the Stress-Induced Lift-Off (SLIM)-cutting seems to present a good alternative. It mainly reduces the waste of silicon and it may help in producing thinner wafers. However, like any new technique, it is necessary to verify that the final product meets the demands of the PV market in terms of material quality and its optoelectronic properties.

In the present work, the study of the modification produced by laser pulses in the infrared range was combined with the study of some wafers obtained by SLIM-cutting. The results obtained on the buried modifications showed that the use of a 2.08 μm laser with picosecond pulses and with μJ energy creates elongated defects with a maximum size of 2 μm. The precision with which these defects are located at a specific depth depends on the pulse energy. In general, the effective depth is shorter than the laser focus depth when the pulse energy increases. Moreover, the laser processing caused the localized formation of crystal disorder or amorphous silicon, but their contribution is not significant in the area surrounding the defects. Precisely, the Raman spectra of areas in which the size of the defect was about half of the total area contributing to the spectrum did not show changes from reference silicon spectra. On the other hand, when spectra were acquired from regions where the modified material was predominant, strong features of these different phases appeared. Moreover, a shift of $0.7 - 0.9$ cm^{-1} and a broadening of ≈ 1 cm^{-1} of the characteristic c-Si TO-peak were detected. A value of ≈ 400 MPa of tensile stress was associated with the shifts.

The transition from monocrystalline silicon to polycrystalline or amorphous

silicon in correspondence to laser-induced defects could be a problem for PV applications. However, the detachment of the two parts could also contribute to inducing stress. The Raman characterization of the wafer surface detected a small TO-peak shift for some spots on the wafer surface. The shift was associated with a tensile stress of $59 - 257$ MPa. The minority carriers' lifetime was in the range of 20-71 μs. No correlation was established between the Raman results showing the centroid shift of the TO-peak, the lifetime values and the position on the wafer surface.

The SLIM cutting successfully leads to separating the thick silicon wafer into two thinner foils. The surface appears irregular, with a "stair-like" or "streaked-like" microscopic texture, and it is significantly rougher than typical silicon wafers. Nevertheless, it must be considered that these analyzed wafers were not treated after the separation process. Small circular regions with modified properties cover the entire wafer surface with a pattern that does not seem orderly and regular. The dimensions of these regions confirm that they were probably created due to laser exposure. Interestingly, the electrical behaviour of these regions is the same as the unmodified monocrystalline silicon surface, as results from the microscopic analysis performed with AFM.

All of these results are promising because they show that the laser process and separation modify the properties of silicon, but not in an incisive way. In particular, it can be thought that a subsequent treatment step, e.g. polishing or annealing, is sufficient to remove the most damaged first surface layer. In conclusion, the studied SLIM cutting is certainly promising in the light of an initial study such as the one reported in this thesis. However, there are still many aspects to be analyzed and systematic studies to be conducted on the technique, which are not yet present in the literature.

Chapter 6

Future work

The present work has several possible developments. On one hand, the experimental results could be enriched by employing more characterization techniques. For instance, the micro-Raman analysis could be broadened by employing a different laser. In particular, the 1064 nm laser allows us to penetrate the surface and measure the Raman shift of buried modifications. Indeed, the penetration depth of the 532 nm laser in silicon is ~ 2 μm, while the penetration of the 1064 nm laser would be ~ 1 mm [11]. Within this project, only the 532 nm laser was available to carry out the measurements and therefore only surface laser-written lines were analyzed. However, the analysis of the buried defects could show the changed properties within the silicon bulk and the dependence of the induced stress, amorphization or crystal disorder on the bulk laser-writing process may be established. In addition, X-Ray Diffraction studies could deepen our knowledge regarding the presence of surface residual stress, amorphization and polycrystallization. The refractive index change of the buried defects could be determined with IR microscopy, while scanning transmission electron microscopy could help to determine their nature. In conclusion, the thickness total variation of the wafers could be calculated to compare them with established technologies, such as fixed-abrasive and slurry-based cutting techniques.

On the other hand, it may be interesting to carry out a systematic study of the separation procedure, focusing attention on both the material choice for the stress-inducing layer and the process of rapid cooling to induce the lift-off of the thin wafer. Indeed the thin thickness and standard dimension of silicon wafers required by the PV market must be achievable without a high probability of breakage and edge damage. In addition, the whole SLIM process should be repeated with commercial-grade silicon wafers that have an initial lifetime of the order of 1 ms, aiming to verify that even a 50% drop still makes the wafer suitable for PV applications.

Bibliography

1. L. Oberbeck, K. Alvino, B. Goraya, M. Jubault, *Progress in Photovoltaics: Research and Applications* **28**, 1207–1214 (2020).
2. National Renewable Energy Laboratory, *NREL Best Research-Cell Efficiency Chart*, Accessed May 31, 2022. `https://www.nrel.gov/pv/cell-efficiency.html`.
3. C. Ballif, F.-J. Haug, M. Boccard, P. J. Verlinden, G. Hahn, *Nature Reviews Materials* **7**, 597–616 (2022).
4. V. Fthenakis, E. Leccisi, *Progress in Photovoltaics: Research and Applications* **29**, 1068–1077 (2021).
5. Nakamura Choukou Co., *Silicon solar cells manufacturing process*, Accessed October 1, 2022. `http://www.nakamura-gp.co.jp/en/product01_01.html`.
6. R. A. Richter *et al.*, *J. Opt. Soc. Am. B* **37**, 2543–2556 (2020).
7. J. Serra, J. M. Alves, A. Vallera, *Journal of Crystal Growth* **468**, The 18th International Conference on Crystal Growth and Epitaxy (ICCGE-18), 590–594 (2017).
8. O. Tokel *et al.*, *Nature Photonics* **11**, 639–645 (2017).
9. M. Chambonneau *et al.*, *Laser & Photonics Reviews* **15**, 2100140 (2021).
10. I. Yonenaga, in *Handbook of Photovoltaic Silicon*, ed. by D. Yang (Springer Berlin Heidelberg, Berlin, Heidelberg, 2019), pp. 1–48.
11. W. M. Bullis, in *Handbook of Semiconductor Silicon Technology* (Elsevier Science, 1990), pp. 347–450.
12. H. M. Liaw, in *Handbook of Semiconductor Silicon Technology* (Elsevier Science, 1990), pp. 94–181.
13. Semilab, *WT-2000PV User Manual Volume 1*, Semiconductor Physics Laboratory, Inc.

14. A. Cuevas, D. Macdonald, *Solar Energy* **76**, Solar World Congress 2001, 255–262 (2004).

15. A. Richter, S. W. Glunz, F. Werner, J. Schmidt, A. Cuevas, *Phys. Rev. B* **86**, 165202 (16 2012).

16. M. J. Kerr, A. Cuevas, *Journal of Applied Physics* **91**, 2473–2480 (2002).

17. B. A. Veith-Wolf, S. Schäfer, R. Brendel, J. Schmidt, *Solar Energy Materials and Solar Cells* **186**, 194–199 (2018).

18. W. Shockley, H. J. Queisser, *Journal of Applied Physics* **32**, 510–519 (1961).

19. H. M. van Driel, *Phys. Rev. B* **35**, 8166–8176 (15 1987).

20. J. Veirman *et al.*, *Solar Energy Materials and Solar Cells* **228**, 111128 (2021).

21. VDMA, *International Technology Roadmap for Photovoltaic (ITRPV)- 2021 Results - Thirteenth Edition, March 2022*, Accessed October 1, 2022. `https://www.vdma.org/international-technology-roadmap-photovoltaic`.

22. X. Yu, D. Yang, in *Handbook of Photovoltaic Silicon*, ed. by D. Yang (Springer Berlin Heidelberg, Berlin, Heidelberg, 2017), pp. 1–45.

23. L. Arnberg, M. Di Sabatino, E. J. Øvrelid, *Journal of Crystal Growth* **360**, 56–60 (2012).

24. VDMA, *International Technology Roadmap for Photovoltaic (ITRPV)- 2020 Results - Twelfth Edition, March 2021*, Accessed October 1, 2022. `https://www.vdma.org/international-technology-roadmap-photovoltaic`.

25. H. J. Möller, in *Handbook of Photovoltaic Silicon*, ed. by D. Yang (Springer Berlin Heidelberg, Berlin, Heidelberg, 2019), pp. 359–395.

26. H. J. Möller, in *Handbook of Photovoltaic Silicon*, ed. by D. Yang (Springer Berlin Heidelberg, Berlin, Heidelberg, 2019), pp. 269–309.

27. E. Ohmura, Y. Kawahito, K. Fukumitsu, J. Okuma, H. Morita, presented at the Fundamentals of Laser-Assisted Micro- and Nanotechnologies 2010, ed. by V. P. Veiko, T. A. Vartanyan, vol. 7996, pp. 12–19.

28. C. Chen *et al.*, *Metallurgical Research & Technology* **118**, 616 (2021).

29. O. Anspach, B. Hurka, K. Sunder, *Solar Energy Materials and Solar Cells* **131**, 58–63 (2014).

30. P. Bellanger *et al.*, *IEEE Journal of Photovoltaics* **6**, 1115–1122 (2016).

31. J. Serra, P. Bellanger, P. O. Bouchard, M. Bernacki, *physica status solidi c* **11**, 1644–1647 (2014).

32. P. Bellanger *et al.*, *Journal of Renewable and Sustainable Energy* **10**, 023502 (2018).
33. J. M. Serra *et al.*, presented at the 2013 IEEE 39th Photovoltaic Specialists Conference (PVSC), pp. 0177–0180.
34. H.-S. Yang *et al.*, *Frontiers in Chemistry* **6** (2019).
35. V. V. P. Sreenivas, M. Bülters, R. B. Bergmann, *Journal of the European Optical Society: Rapid Publications* **7**, 12035 (2012).
36. E. V. Zavedeev, V. V. Kononenko, V. I. Konov, *Laser Physics* **26**, 016101 (Dec. 2015).
37. X. Zhang *et al.*, *Applied Physics A* **127**, 1–9 (2021).
38. H. Kiyota, K. Hara, M. Jankowski, M. M. Fejer, *Journal of Applied Physics* **127**, 085106 (2020).
39. A. D. Bristow, N. Rotenberg, H. M. van Driel, *Applied Physics Letters* **90**, 191104 (2007).
40. S. Pearl, N. Rotenberg, H. M. van Driel, *Applied Physics Letters* **93**, 131102 (2008).
41. H. Kämmer *et al.*, *Applied Physics A* **124**, 1–6 (2018).
42. R. Soref, B. Bennett, *IEEE Journal of Quantum Electronics* **23**, 123–129 (1987).
43. P. Venkat, T. Otobe, *Applied Physics Express* **15**, 041008 (Apr. 2022).
44. E. Ohmura *et al.*, *International Congress on Applications of Lasers & Electro-Optics* **2006**, M105 (2006).
45. P. C. Verburg, G. R. B. E. Römer, A. J. H. in 't Veld, *Optics express* **22 18**, 21958–71 (2014).
46. P. Verburg *et al.*, *Applied Physics A* **120**, 683–691 (2015).
47. J. Bonse, K.-W. Brzezinka, A. Meixner, *Applied Surface Science* **221**, 215–230 (2004).
48. X. Wang *et al.*, *Journal of Laser Applications* **31**, 022601 (2019).
49. K. Sugimoto, S. Matsuo, Y. Naoi, *Scientific Reports* **10**, 1–7 (2020).
50. C. Florian *et al.*, *Materials* **14** (2021).
51. A. Pushkin, E. Migal, D. Suleimanova, E. Mareev, F. Potemkin, *Photonics* **9** (2022).
52. M. Chambonneau, D. Richter, S. Nolte, D. Grojo, *Opt. Lett.* **43**, 6069–6072 (Dec. 2018).

53. X. Yu *et al.*, *Applied Physics A* **122**, 1–7 (2016).
54. M. Chanal *et al.*, *Nature communications* **8**, 1–6 (2017).
55. A. Mouskeftaras *et al.*, *Applied Physics Letters* **105**, 191103 (2014).
56. A. H. Nejadmalayeri *et al.*, *Opt. Lett.* **30**, 964–966 (May 2005).
57. D. Grojo *et al.*, *Phys. Rev. B* **88**, 195135 (19 Nov. 2013).
58. S. Leyder *et al.*, *Applied Surface Science* **278**, Laser materials processing for micro and nano applications, E-MRS 2012 Symposium V, 13–18 (2013).
59. D. Grojo, A. Mouskeftaras, P. Delaporte, S. Lei, *Journal of Applied Physics* **117**, 153105 (2015).
60. M. Mori *et al.*, *physica status solidi (a)* **212**, 715–721 (2015).
61. A. Das, A. Wang, O. Uteza, D. Grojo, *Opt. Express* **28**, 26623–26635 (Aug. 2020).
62. A. Wang, A. Das, D. Grojo, *Phys. Rev. Research* **2**, 033023 (3 2020).
63. E. I. Mareev *et al.*, *Laser Physics Letters* **17**, 015402 (Dec. 2019).
64. V. V. Kononenko, V. V. Konov, E. M. Dianov, *Opt. Lett.* **37**, 3369–3371 (Aug. 2012).
65. I. Pavlov *et al.*, *Opt. Lett.* **42**, 3028–3031 (Aug. 2017).
66. G. Matthäus *et al.*, *Opt. Express* **26**, 24089–24097 (Sept. 2018).
67. M. Chambonneau *et al.*, *Phys. Rev. Applied* **12**, 024009 (2 Aug. 2019).
68. X. Wang *et al.*, *Opt. Express* **29**, 14201–14207 (May 2021).
69. N. Tolstik, E. Sorokin, R. A. Richter, V. Kalashnikov, I. T. Sorokina, *in preparation for submission to Optica* (2022).
70. Y. Zhu, Z. Hameiri, *Progress in Energy* **3**, 012001 (2021).
71. S. Rein, *Lifetime Spectroscopy: A Method of Defect Characterization in Silicon for Photovoltaic Applications* (Springer Berlin Heidelberg, 2006).
72. M. Wilson, P. Edelman, J. Lagowski, S. Olibet, V. Mihailetchi, *Solar Energy Materials and Solar Cells* **106**, SiliconPV, 66–70 (2012).
73. C. Claeys, E. Simoen, J. Vanhellemont, *Nuclear Instruments and Methods in Physics Research Section A: Accelerators, Spectrometers, Detectors and Associated Equipment* **377**, Proceedings of the Seventh European Symposium on Semiconductor, 244–257 (1996).
74. M. Schöfthaler, R. Brendel, *Journal of Applied Physics* **77**, 3162–3173 (1995).

75. R. Merlin, A. Pinczuk, W. H. Weber, in *Raman Scattering in Materials Science*, ed. by W. H. Weber, R. Merlin (Springer Berlin Heidelberg, Berlin, Heidelberg, 2000), pp. 1–29.

76. N. John, S. George, in *Spectroscopic Methods for Nanomaterials Characterization*, ed. by S. Thomas, R. Thomas, A. K. Zachariah, R. K. Mishra (Elsevier, 2017), pp. 95–127.

77. P. Goh, A. Ismail, B. Ng, in *Membrane Characterization*, ed. by N. Hilal, A. F. Ismail, T. Matsuura, D. Oatley-Radcliffe (Elsevier, 2017), pp. 31–46.

78. J. Menéndez, in *Raman Scattering in Materials Science*, ed. by W. H. Weber, R. Merlin (Springer Berlin Heidelberg, Berlin, Heidelberg, 2000), pp. 55–103.

79. C. Pan, Y. Shi, F. Hui, E. Grustan-Gutierrez, M. Lanza, in *Conductive Atomic Force Microscopy* (John Wiley & Sons, Ltd, 2017), chap. 1, pp. 1–28.

80. R. D. Oliveira, D. Albuquerque, T. Cruz, F. Yamaji, F. Leite, in *Atomic Force Microscopy*, ed. by V. Bellitto (IntechOpen, Rijeka, 2012), chap. 7.

81. K. Bian *et al.*, *Nature Reviews Methods Primers* **1**, 1–29 (2021).

82. G. Benstetter, A. Hofer, D. Liu, W. Frammelsberger, M. Lanza, in *Conductive Atomic Force Microscopy* (John Wiley & Sons, Ltd, 2017), chap. 3, pp. 45–77.

83. Reinishaw, *InVia Reflex Raman microscope specifications*, Accessed October 1, 2022. `https://www.renishaw.com/en/invia-confocal-raman-microscope--6260`.

84. H. Kämmer *et al.*, *Laser & Photonics Reviews* **13**, 1800268 (2019).

85. I. D. Wolf, *Semiconductor Science and Technology* **11**, 139–154 (Feb. 1996).

86. F. Zhang *et al.*, *Solar Energy Materials and Solar Cells* **193**, 214–218 (2019).

87. X. Wu, J. Yu, T. Ren, L. Liu, *Microelectronics Journal* **38**, 87–90 (2007).

88. N. E. Grant *et al.*, *Solar RRL* **5**, 2000754 (2021).

89. PV Education, *General Properties of Silicon*, Accessed October 1, 2022. `https://www.pveducation.org/pvcdrom/materials/general-properties-of-silicon`.

90. M. Tilli, in *Handbook of Silicon Based MEMS Materials and Technologies (Second Edition)*, ed. by M. Tilli *et al.* (William Andrew Publishing, Boston, Second Edition, 2015), pp. 86–103.

91. MikroMasch, *Roughness of Si Wafer*, Accessed October 1, 2022. `https://www.spmtips.com/how-to-choose-afm-probes-by-applications-metrology-roughness-of-Si-wafer.html`.

92. Z. Fang, Y. Zhang, R. Li, Y. Liang, H. Deng, *International Journal of Machine Tools and Manufacture* **159**, 103649 (2020).

93. C. Vecchio *et al.*, *Nanoscale Research Letters* **6**, 1–7 (2011).

94. A. Oliveros *et al.*, *Journal of Materials Research* **28**, 78–86 (2013).

95. M. Canino, P. Fedeli, C. Albonetti, R. Nipoti, *Journal of Microscopy* **280**, 229–240 (2020).

96. RamanLife, *SiC Raman spectrum*, Accessed October 1, 2022. `https://ramanlife.com/library/silicon-carbide/`.

97. D. Cavalcoli, M. Rossi, A. Tomasi, A. Cavallini, *Nanotechnology* **20**, 045702 (2008).

98. S. Rubanov, P. R. Munroe, *Journal of Microscopy* **214**, 213–221 (2004).

99. P. Li *et al.*, *Nanoscale* **13**, 1529–1565 (3 2021).

100. S. Rigaud, MA thesis, Norwegian University of Science and Technology NTNU, 2019.

Appendix A: FIB for cross-section preparation

Focused Ion Beam (FIB) is one of the possible techniques to expose the buried modification in the monocrystalline silicon bulk. FIB advantages are that the electron-transparent area can be located with high precision, the milling times are shorter than with conventional argon ion milling, and flat, parallel-sided specimens can be readily prepared [98]. Therefore, FIB is already an established method to create clean cross-sections with high resolution [99]. Despite its advantages, the main drawback of this technique is the damage induced by the use of a highly energetic gallium ion beam. The damage is caused by the redeposition of the sputtered atoms, ion implantation and amorphization, as depicted in Figure 1. The following section presents the characterization of the FIB-induced damage in a Cz-Si wafer. The objective is to determine the applicability of this technique for SEM sample preparation.

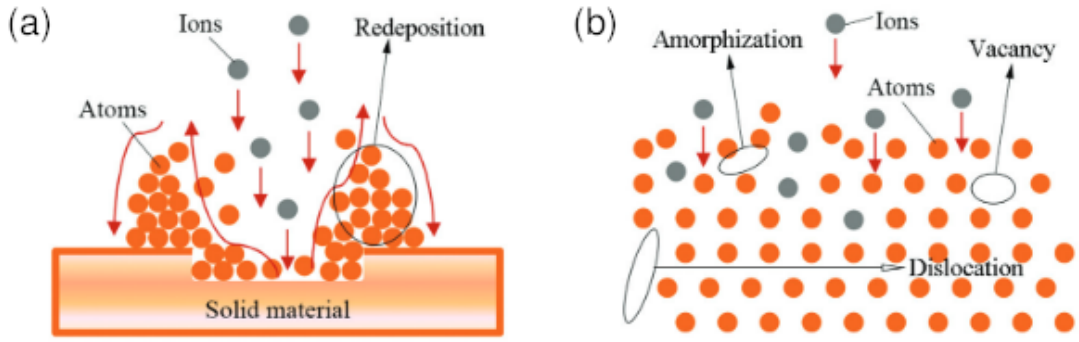

Figure 1: Schematic diagram of **(a)** the redeposition effect and **(b)** of ion implantation damage. Adapted from [99].

Experimental procedure

In light of the work carried out by Rigaud [100] in 2019 at NTNU, a two-step process was employed to create the cross-section. Indeed, the deep depth of the defects, which ranges from 200 μm to 300 μm, requires an extremely long milling time. Employing a two-step process, a preliminary rough milled region is created with maximum beam current and then, a cleaner cross-section is obtained only in the region of interest with a smaller current. The smaller current is less destructive and avoids damaging the entire region, but takes a significantly longer time.
FEI Helios NanoLab DualBeam FIB was employed. It has an attainable resolution of 1.2 nm for SEM imaging. The SEM images were taken at a working distance of 4.1 mm, a tilt of 52°, a beam current of 0.17 nA and an acceleration voltage of 10 kV.
The samples are polished silicon wafers. They were firstly cleaned with acetone and rinsed with 70% ethanol. Then, they were put in the Diener Electronics' Femto Plasma Cleaner for two minutes at the maximum generator frequency of 40kHz and with oxygen at a 180 sscm flow rate.
Three different tests were carried out with the parameters in Table 1. The milled depths are extremely small compared to the depth at which the modifications are expected but this allows us to perform several tests in a reasonable time. The (x, y) dimensions are chosen considering that the electron beam in SEM requires a sufficiently long pit to be focused on the cross-section. The two other parameters are the acceleration voltage (kV) and the beam current (A). The time required to mill the specified region with the set parameters is also reported. This information tells how long the sample was exposed to the high-current beam, which is a crucial aspect of damage assessment. Note that the third test was performed with the first high current step only. In order to assess the damage level on the sample, a simple silicon wafer was processed with the FIB and analyzed with Micro-Raman spectroscopy (refer to Section 2.2.2 for details).

Characterization results

Figure 2 reports the performed tests. The images were taken after processing the silicon wafer with the two-step technique with the SEM inside FEI Helios NanoLab DualBeam FIB.
The SEM images show the top view of the pits that were milled (Figures 2a-c) and the region close to the cross-section wall (Figures 2d-f). As expected, a first rough cut is distinguished on the opposite side of the cross-section where the milling starts. As the milling continues, the material is removed with subsequent steps. Some uncommon features are visible on the bottom of the milled area of the tests in Figure 2d and Figure 2e, which could be due to the redeposition of the material

Table 1: Milling parameters of the three tests carried out with FIB: milled area S, depth z, acceleration voltage V, beam current I and processing time t.

	S (μm^2)	z (μm)	V (kV)	I (nA)	t (min)
Test 1					
First step	3.83×10^4	1	30	21	20
Second step	0.31×10^4	1	30	2.8	20
Test 2					
First step	3.83×10^4	1	30	21	20
Second step	0.13×10^4	1	30	2.8	15
Test 3					
First step	1.75×10^4	3	30	21	20

after the removal. However, for the third test the milled area appears smooth (Figure 2f).

The damage caused by FIB was assessed with Micro-Raman spectroscopy with the same method explained in Section 2.2.2 employing the 532 nm laser. Figures 3a-b and 3e show the regions where the Raman spectra were acquired, while Figures 3c-d and 3f show the results of the Raman analysis.

Three main regions can be distinguished after the Raman analysis: the cross-section region, the bottom and the walls of the milled area and the outer region. The spectrum taken from a point close to the cross-section (Spot B in Figure 3a and spectrum in Figure 3c) shows the presence of the characteristic TO-peak at 520 cm^{-1} [68] and the rest of the spectrum is almost the same as a typical c-Si sample. This result is promising considering the importance of having unaltered properties in the cross-section. Moving further away from the cross-section (Spot C in Figure 3a and spectrum in Figure 3c), the Raman spectra show strong features between 100 and 200 cm^{-1} and between 430 and 500 cm^{-1} corresponding to amorphous silicon (a-Si) [68]. Here, the TO-peak almost disappears. On the walls of the milled area the TO-peak completely disappears (Spot D in Figure 3a and spectrum in Figure 3c). Therefore, the uncommon features visible in the SEM images (Figures 2d-e) could be due to the redeposition of the removed material as amorphous silicon. The spectrum from the outer region (Spot A in Figure 3a and spectrum in Figure 3c) shows both the c-Si and the a-Si characteristic features. Thus, the employed high current may also have amorphized the area outside the region where the material was removed.

The previous results are confirmed by the Raman analysis reported in Figure 3d: the TO-peak disappears for the spots inside the milled area (A-B) and the outer region shows both the 520 cm^{-1} c-Si peak and the amorphous features between

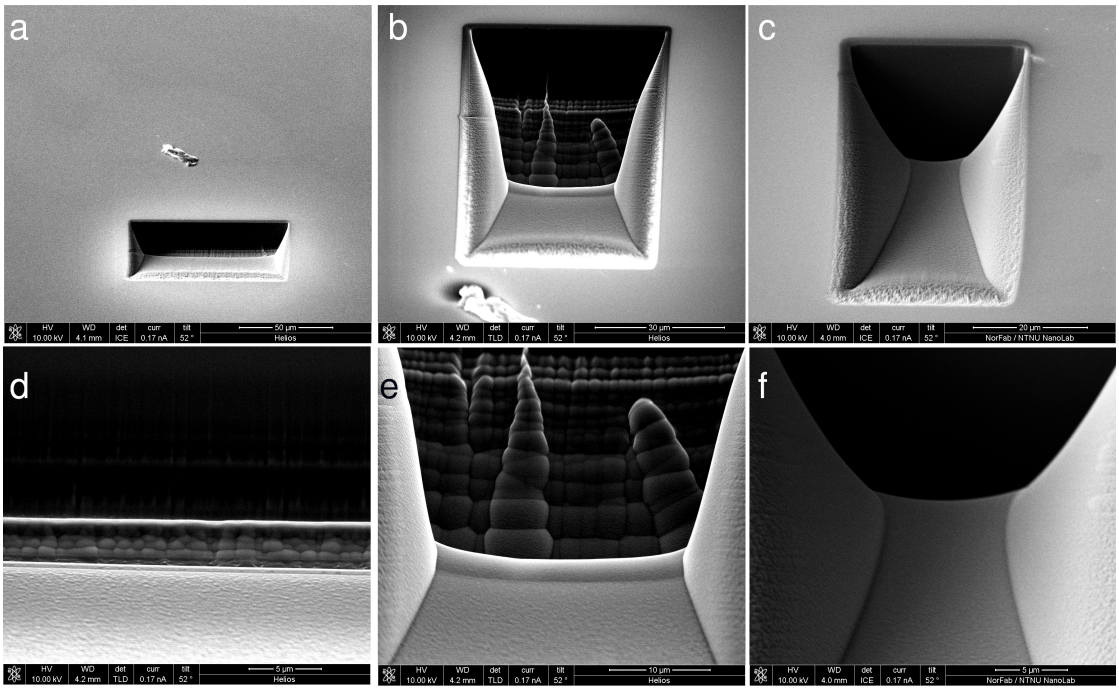

Figure 2: SEM images of the cross-sections milled with FIB: **(a,d)** Test 1; **(b,e)** Test 2; **(c,f)** Test 3. The test number refers to Table 1.

430 and 500 cm^{-1}.
The Raman measurements highlighted the need for two reference spots: one in the area close to the milled area and one further away. This is also supported by the visible presence of a square with a different reflectivity, which can be seen with the OM (see Figure 3e). Indeed, the region close to the modified material may have different properties from those of the unmodified silicon wafer.
This hypothesis is confirmed by the Micro-Raman results. Considering Figure 3f, the two Raman spectra show significant differences: the outer spot (A in Figure 3e), which belongs to the unmodified material, has the typical c-Si spectrum with only the characteristic peak at 520 cm^{-1}. On the other hand, the spectrum acquired from the inner spot (B in Figure 3e), which is close to the milled area, shows the characteristic features of a-Si between 430 and 500 cm^{-1} alongside the c-Si peak.

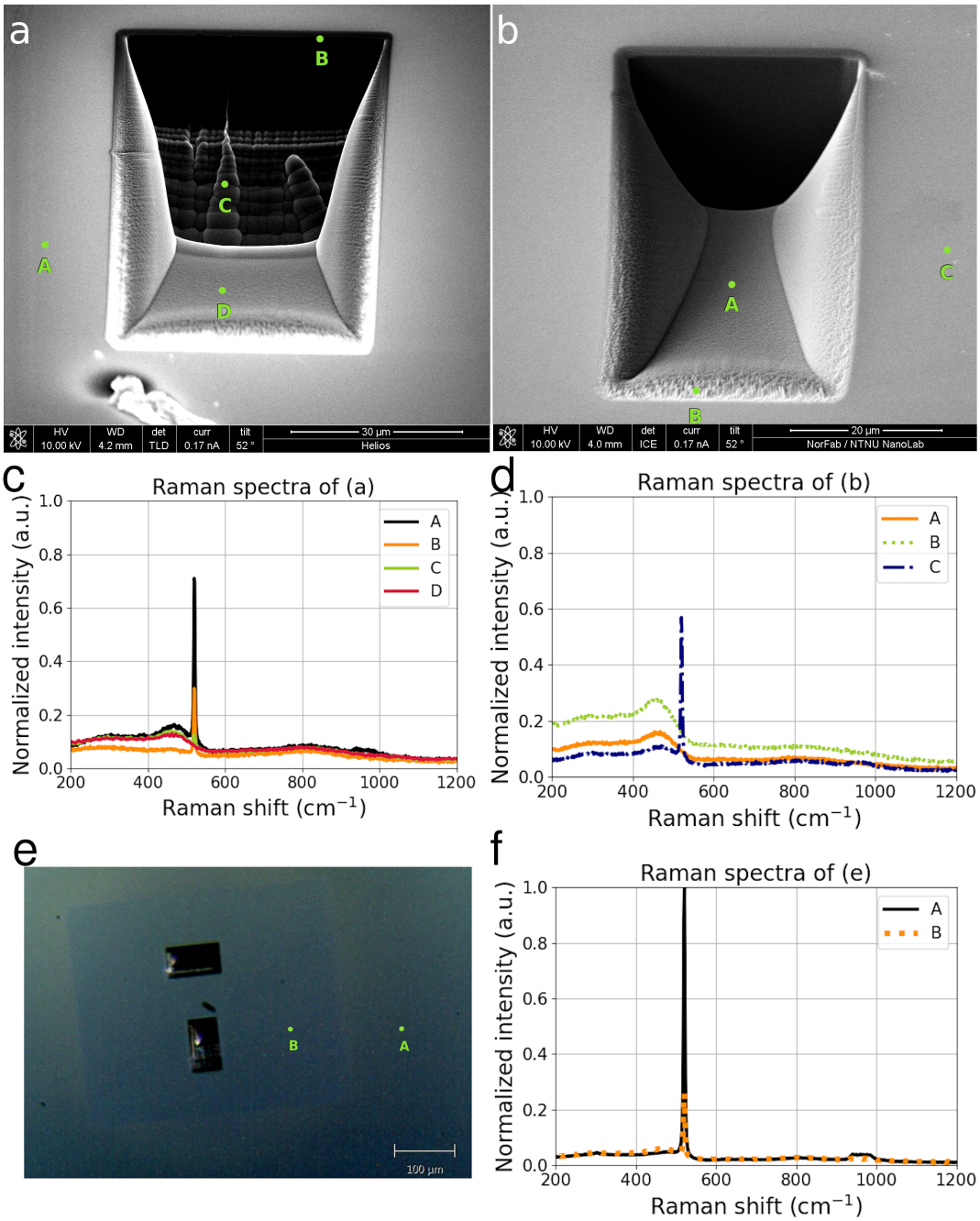

Figure 3: **(a)** SEM image of Test 2 and spots were Raman spectra in **(c)** were acquired; **(b)** SEM image of Test 3 and spots were Raman spectra in **(d)** were acquired; **(e)** Visible microscope image of the region exposed to high current during the milling process on Test 1 and 2 and spots were Raman spectra in **(f)** were acquired. The test number refers to Table 1.

The FIB preparation is damaging for the whole sample area that is under focus during the processing. The cause is probably the high current. Amorphization produced by FIB is a known problem [99]. Redeposition of the sputtered material is also known to take place when another pit is milled over the first one, principally on the side walls of the first pit [98]. The measurement of gallium concentration with energy dispersion spectroscopy (EDS) in the milled area could help to distinguish the amorphous silicon from the redeposited layer. Indeed, the gallium concentration in the layer formed by direct amorphization should be very low, while the redeposited layer should be rich in gallium [98]. Previous studies [98] have reported that FIB produces damage both on the bottom wall and on the side walls. The thickness of the induced damage layer in silicon was calculated to be 36 nm in the bottom wall and 13 nm in the side walls employing gallium ions with 30 kV acceleration voltage, which is the same parameter employed in this work.

Furthermore, to see the buried defects, which are found at a depth of around 200 μm, the sample should be subjected to a high current for a very long time (estimated at more than 10 hours). As a consequence, the sample amorphization during the FIB milling process would be extreme and would compromise subsequent SEM and Micro-Raman analyses.

In light of these considerations, the FIB technique was not considered a good method to prepare the samples in this research project. Indeed, the laser-induced modifications are well below the surface and there are no visible marks that could help to locate them, which means that the FIB milling procedure would require several attempts to identify the defects. Cleaving and etching remain the best methods to expose the laser-induced modification quickly and efficiently, as supported by the widespread use of these techniques reported in the literature [46, 48].